



HAL
open science

Atom chips for metrology

Ramon Szmuk

► **To cite this version:**

Ramon Szmuk. Atom chips for metrology. Quantum Physics [quant-ph]. Université Pierre et Marie Curie - Paris VI, 2015. English. NNT : 2015PA066089 . tel-01260339

HAL Id: tel-01260339

<https://theses.hal.science/tel-01260339>

Submitted on 22 Jan 2016

HAL is a multi-disciplinary open access archive for the deposit and dissemination of scientific research documents, whether they are published or not. The documents may come from teaching and research institutions in France or abroad, or from public or private research centers.

L'archive ouverte pluridisciplinaire **HAL**, est destinée au dépôt et à la diffusion de documents scientifiques de niveau recherche, publiés ou non, émanant des établissements d'enseignement et de recherche français ou étrangers, des laboratoires publics ou privés.



LABORATOIRE DES SYSTÈMES DE RÉFÉRENCE TEMPS-ESPACE

**THÈSE DE DOCTORAT DE
L'UNIVERSITÉ PIERRE ET MARIE CURIE**

**Spécialité : Physique Quantique
ÉCOLE DOCTORALE : Physique en Île de France (ED 564)**

Présentée par

Ramon Szmuk

**Pour obtenir le titre de
DOCTEUR de l'UNIVERSITÉ PIERRE ET MARIE CURIE**

Sujet de Thèse :

Atom chips for metrology

Jury :

Philipp TREUTLEIN	Rapporteur
Edward HINDS	Rapporteur
Agnès MAÎTRE	Présidente du jury
Hélène PERRIN	Examinatrice
Peter WOLF	Directeur de thèse
Peter ROSENBUSCH	Encadrant

Acknowledgments

I would first like to thank my thesis advisors, Peter Rosenbusch , Jakob Reichel and Peter Wolf. Peter Rosenbusch, with his calm and open character, was always available for discussions throughout my thesis and was an invaluable source of knowledge on both technical details and more fundamental questions. I enjoyed enormously his input on aesthetics when preparing documents and presentations and learned a lot about the importance of telling a compelling story when presenting results. Jakob Reichel, besides giving me valuable guidance throughout the thesis, was always available for fascinating discussions about every kind of physics (from quantum mechanics to wind turbines to violin making). His contagious passion for science was a true source of inspiration. Peter Wolf helped me a lot in keeping my schedule tight, he went over my results and pushed me to publish. His great character made for great interactions and I thank him for his patience and guidance.

I would also like to extend my gratitude to the members of the jury which found the time to evaluate my thesis and provided me with valuable corrections and illuminations: Philipp Treutlein, Edward Hinds, Agnès Maître and H el ene Perrin.

The members of TACC deserve a particular mention. Wilfried Mainault, the post-doc in the first two years of my thesis is a great scientist with a deep understanding of quantum mechanics which made him the to go man for fundamental questions. Vincent Dugrain, the senior PhD student when I just arrived guided me through the experiment and took the time to show me around the lab and explain the delicacies of noise budget analysis. Vincent and Wilfried (the artists) where a fun bunch to work with, always up for a laugh, creating an excellent atmosphere in the lab. Christian Deutsch left a few weeks after I arrived but was nevertheless available for fruitful discussions about the setup and the ISRE effect as he was packing. The new generation of TACC is equally composed of amazing people. Konstantin Ott, a very funny German, was a lot of fun working with. Our walks around the observatory discussing whatever where always a good break from work and I thank him for allowing me to be seen with him in public. Vera Guarrera, the post-doc I worked with for nearly 2 years

and enjoyed practicing my Italian with (until she would politely ask me to stop) was a lot of fun in the lab and was an indispensable guide to the world of academia. Ralf Kohlhaas, the post-doc working on TACC 2 was always available (he seats next to me) to discuss ideas and a great partner for beer and German poetry. Theo Laudat, the new PhD student, is a fast learner and a great guy, I'm sure TACC is safe in his hands and I wish him all the luck. I would also like to thank the forefathers of TACC which built this wonderful experiment I had the pleasure of working on: Friedmann Reinhard, Clement Lacroute and Fernando Ramirez. I would like to thank the Atom Chip team at LKB for discussions and friendships: Jerome Esteve, Alice Sinatra, Romain Long, Claire Lebouteiller, Sébastien Garcia, Hadrien Kurkjian, Florian Haas and Leander Hohmann. I would like to thank all the great scientists at SYRTE. Sebastien Bize, which was always available for long discussions about fundamental questions of quantum mechanics and the more detailed aspects of atomic clock making. Frank Pereira Dos Santos, with his amazing straightforward style, was always there to discuss both technical and fundamental issues. Michel Abgral was a great source of knowledge on the precise architecture of the Maser chains at SYRTE and was always an email away with any question I had. Other scientists helped me throughout: Rodolphe Letargat, Giorgio Santarelli, Pierre Ulrich, Carlos Garrido Alzar, Luigi De Sarlo, Pacôme Delva, Gilles Sakoun, Jocelyne Guena, Remi Geiger, Stéphane Guérandel, Bess Fang, Paul-Eric Pottie, Giovanni-daniele Rovera, Ouali Acef, Christine Guerlin, Sébastien Merlet and Philip Tuckey. I would like to thank also the great guys from the electronics workshop which were always there to explain, help design, fix and loan me some hardware. The energetic José Pinto-Fernandes, the venerable and funny Michel Lours and the formidable Laurent Volodimer. The directors of the lab deserve a special mention, Noël Dimarcq and now Arnaud Landragin are incredible scientists. Noël with his calm spirit and Arnaud (quite the opposite) both make for great directors and conversation partners. Being the son of architects I value scenery a lot. The historic site of the Paris Observatory was always a source of inspiration during my many strolls in the large garden and historic building. I must thus also thank Jean-Baptiste Colbert for the conception and Louis XIV for the funding of

this amazing place. During my stay at the observatory I had the good fortune of making many friends, partners with which I could share a beer and discuss science and other forms of living, they are: Sinda Mejri, Adele Hilico, Jean-Marie Danet, Indranil Dutta, Tristan Farah, Jean Lautier, Bruno Pelle, Rinat Tyumenev, Wenhua yan, Satyanarayana Bade, Pierre Gillot, Matthias Lopez, Katharina Predehl, Cyrille Solaro, Adèle Hilico, Marc Antoine-Buchet, Olivier Gaubron, Eric Chea, Baptiste Chupin and Edouard Richard. I would also like to thank my family for supporting me throughout my thesis and for coming to my defense in Paris all the way from Israel. My parents Nitza and Peter Szmuk, my sister Lital and my wife's parents Yuri and Liodmila Katsman.

Lastly I would like to thank the number one encouraging and stabilising force in my life, my amazing wife and best friend Ira who joined me in this Parisian adventure and showed me nothing but unconditional love throughout. I am incredibly lucky to have such a partner in my life and I hope the rest of our journey will be as awesome as it has been up to now. I dedicate this thesis to you and I promise to do the dishes more often.

Abstract

This thesis covers two main subjects: the evaluation of the stability of a Trapped Atom Clock on a Chip (TACC) and the expansion of this technology towards creating an atom interferometer on the same chip. The combination of a clock and an interferometer on the same chip constitutes the basis for the realization of atom-based integrated inertial navigation units. TACC has been built with the aim of realizing a compact high stability clock. Previous work installed the clock operation and discovered, among others, very long coherence times, which allow Ramsey interrogation up to 5 s – a prerequisite for high stability operation. I present the first thorough evaluation of the clock stability. Together with my predecessor we have demonstrated relative frequency fluctuations of $5.8 \cdot 10^{-13}$ at 1 s integrating down to $6 \cdot 10^{-15}$ at 30 000 s. This performance outruns the best commercial clocks by almost one order of magnitude and is competitive with the best compact atomic clocks under development. In particular, this long-term stability is reached by two other compact clocks only. Jointly we have investigated 7 contributions to the clock frequency noise, which I analyze in detail. The sum of all contributions explains the measured frequency fluctuations and confirms that all major noise sources have been identified. The frequency (in)stability is dominated by atom temperature fluctuations and magnetic field fluctuations followed by the local oscillator noise via the Dick effect. The analysis allows me to propose improvements of a future 2nd generation set-up, which has the potential to reach a stability of 10^{-13} at 1s equivalent to the well-known hydrogen maser, but in a much smaller set-up.

The second part of this thesis aims to expand the versatility of our atom chip to create an atom interferometer. I have studied various interferometer schemes using microwave dressed potentials and implemented these to the set-up. The first scheme, following work by P. Treutlein et al., involves displacing one of the clock states vertically during a Ramsey clock sequence thereby allowing the measurement of potential gradients by exploiting the differential frequency shift accumulated between the two states. Ramsey fringes were recorded for different durations of the splitting,

resulting in a clear signal of the wavepacket separation. The relative velocity of the combining wavepackets is observed as optical fringes. A new method for estimating the wavepacket separation is developed.

The second scheme uses microwave dressing to generate a double well potential in one of the clock states and a single well in the other - a configuration suggested in the thesis of P. Treutlein. Starting in the single well, a π -pulse on the clock transition constitutes the beam splitter and leads to a spatial separation for the same internal state. Such a scheme has the advantage over the first that it is insensitive from clock shifts. Furthermore it has the advantage over other existing schemes because it does not require dynamical variation of the populated potential which induces cloud excitations as the potential goes through the quartic point. Implementation of this scheme has to respect the particularities of our chip, notably the vertical gradient of the evanescent microwave field. This is overcome by the use of two frequency dressing. I demonstrate that the potentials of both clock states can be modified independently. Varying the differential detuning, I optimized the transfer between the single and double well potential. The splitting distance is characterized as a function of dressing power and detuning as well as the dynamics of the split atom clouds.

Résumé

Cette thèse porte sur deux sujets principaux: l'évaluation de la stabilité d'une horloge sur microcircuit utilisant des atomes piégés (Trapped Atom Clock on a Chip - TACC) et l'extension de cette technologie vers la réalisation d'un interféromètre atomique sur la même puce. La combinaison d'une horloge et un interféromètre sur la même puce constitue la base pour la réalisation de capteurs inertiels intégrés pour la navigation. TACC a été construit dans le but de réaliser une horloge compacte de grande stabilité. Des travaux antérieurs ont installé le fonctionnement de l'horloge et ont découvert, entre autres, des temps de cohérence très longues, qui permettent une interrogation Ramsey jusqu'à 5 s, une condition préalable pour le fonctionnement à grande stabilité. Je présente ici la première évaluation approfondie de la stabilité de l'horloge. Avec mon prédécesseur, nous avons démontré les fluctuations de fréquences relatives de $5.8 \cdot 10^{-13}$ à 1 s intégrant jusqu'à $6 \cdot 10^{-15}$ à 30000 s. Cette performance dépasse les meilleures horloges commerciales de près d'un ordre de magnitude et est en concurrence avec les meilleures horloges atomiques compactes en cours de développement. En particulier, cette stabilité à long terme est atteinte par seulement deux autres horloges compactes. Nous avons étudié sept contributions au bruit de fréquence de l'horloge, qui je analyse en détail. La somme de toutes les contributions explique les fluctuations de fréquence mesurées et confirme que toutes les sources majeures de bruit ont été identifiées. La stabilité de fréquence est dominée par les fluctuations de la température des atomes et du champs magnétique suivis par le bruit de l'oscillateur local via l'effet Dick. L'analyse me permet de proposer des améliorations d'une futur génération du set-up, qui pourra atteindre une stabilité de $1 \cdot 10^{-13}$ à 1s, équivalente à celle d'un maser à hydrogène, mais dans un dispositif plus compact. La deuxième partie de cette thèse vise à étendre la polyvalence de notre puce atomique pour créer un interféromètre atomique. J'ai étudié divers régimes d'interféromètres en utilisant des potentiels habillés par microondes et je les ai mis en place. Le premier régime, suite des travaux de P. Treutlein et al., consiste à déplacer l'un des états d'horloge verticalement pendant une séquence d'horloge Ramsey. Ceci

permet la mesure de gradients de potentiel en exploitant la fréquence différentielle entre les deux états. Des franges de Ramsey étaient enregistrées pour différentes durées de la scission résultant en un signal clair de la séparation des paquets d'onde. En recombinaison, la vitesse relative des paquets d'ondes est observée via des franges optiques. Une nouvelle méthode d'estimation de la séparation de paquet d'ondes est développée. Le second régime utilise des champs microondes pour générer un potentiel de double puits dans l'un des états d'horloge et un seul puits dans l'autre - une configuration suggérée dans la thèse de P. Treutlein. À partir du seul puits, un pulse π sur la transition d'horloge constitue la séparatrice de l'interféromètre et conduit une séparation spatiale tout en préservant le même état interne pour les deux bras de l'interféromètre. Un tel système a l'avantage sur le premier qu'il est insensible aux déplacements de la fréquence d'horloge. De plus, il porte des avantages sur les autres systèmes existants car il ne nécessite pas de variation dynamique du potentiel peuplé qui induit des excitations du nuage d'atomes quand le potentiel passe par le point quartique. Notre mise en œuvre expérimentale a dû respecter les particularités de notre puce, notamment le gradient vertical du champ de microondes. Il est surmonté par l'utilisation de deux fréquences. Je montre que les potentiels des deux états d'horloge peuvent être modifiés indépendamment. La variation du désaccord différentiel a été utilisée pour optimiser le transfert entre le simple puits et le double puits. La distance de séparation est caractérisée en fonction de la puissance d'habillage et du désaccord ainsi que la dynamique des nuages atomiques séparés.

Contents

1	Introduction	11
2	Clock frequency stability	17
2.1	Atomic System	18
2.2	Experimental Apparatus	19
2.3	Stability Measurement	22
2.4	Noise Analysis	26
2.4.1	Detection and Quantum Projection Noise	27
2.4.2	Local oscillator noise	29
2.4.3	Fluctuations of the atomic frequency	34
2.5	Conclusion	43
3	Towards an atom chip atom interferometer	45
3.1	Review of atom interferometers	45
3.1.1	A basic framework for comparing the sensitivity of atom interferometers	46
3.1.2	Free fall atom interferometers	48
3.1.3	Confined atom interferometers	51
3.1.4	Microwave dressed potentials and our proposed interferometer scheme	56
3.2	Theory	61
3.2.1	General considerations	61
3.2.2	Transfer between a single and a double well	62

3.2.3	The dressed state picture in the microwave regime	64
3.3	Measurement of the microwave dressed potential	85
3.3.1	Measurement of the microwave mode shape with cold atoms	85
3.3.2	Extracting the dressing parameters	86
3.3.3	Experimental results confirming our characterization	87
3.4	Results: state selective single well potentials	89
3.4.1	Internal and external coherence	92
3.4.2	Wavepacket separation from phase gradients	95
3.5	Results: state selective double well potentials	97
3.5.1	Characterization of the double well potential	98
3.5.2	High Rabi frequency transfer	99
3.5.3	Dynamics in the double well potential	101
3.5.4	Low Rabi frequency transfer	104
3.6	Conclusion	110
4	Conclusion	113
A	The spectral analysis of fluctuations	117
A.1	Unit conversion of the Power Spectral density	122

Chapter 1

Introduction

The purpose of this work is to demonstrate the feasibility of using magnetically trapped atoms on atom chips [53, 99] for the realisation of a compact atomic sensor.

During the first part of my thesis I have finalized the characterization of the stability of our trapped atomic clock on a chip (TACC). I have performed measurements on the local oscillator noise and have estimated its contribution to the instability via the Dick effect. I have also analyzed the noise contributions of temperature and magnetic field fluctuations and have incorporated this analysis, together with that of my predecessors, into a complete noise budget that accounts for all the observed noise.

The second part of the thesis involved the development of a new interferometer scheme using state selective MW dressed potentials. Here I have performed a theoretical and experimental study of this new scheme and have participated in the analysis of the results. In particular, I have implemented two frequency dressing of the clock states in order to cancel their relative vertical displacement (originating from the vertical gradient of the MW field), increasing their overlap and allowing the transfer of atoms between the two states.

I will start by putting my work into context with two short introductory sections discussing compact clocks and interferometers and continue with the respective chapters detailing my work.

Trapped atom clock on a chip (TACC)

Atomic clocks form the backbone of technologies requiring precise frequency references. The most known example is that of the Global Navigation Satellite System (GNSS), where a network of satellites, with on board atomic clocks, distributes a reference clock signal that allows for sub-meter positioning of receivers on the ground [42]. Applications such as Very Long Baseline Interferometry (VLBI) [32,87], Geodesy [118], pulsar astronomy [123], space gravity and climate surveys [113] and the test of fundamental physics [44,103] also require very stable frequency references. To date, atomic clocks give by far the best performance and have long surpassed classical devices [13].

The workhorse of modern atomic clocks is the atomic fountain, operating today at the mid 10^{-16} level [91] but with a large footprint, usually occupying a whole room and requiring skilled personnel to operate. They are thus unsuitable for embedding in a satellite or for standard commercial use. Commercial atomic clocks available today, such as the industry standard Symmetricom 5071A [3] offer modest performances on the order of $5 \cdot 10^{-12}1/\sqrt{\tau}$, but with a much reduced package size of about 30 l. Smaller integrated Rubidium oscillators with package sizes on the order of 100-500 ml exist, but with a further reduction in performance reaching the low 10^{-11} level [1,2,5].

The present state of the art thus offer two alternatives, either large and cumbersome devices which perform on the 10^{-16} level or below, or sub-liter scale devices that perform at four or five orders of magnitude below these levels and which no longer outperform state of the art commercial quartz oscillators at short and medium range integration times [108]. The current technological situation then demands a compact frequency references that does not perform substantially worse than their large laboratory counterparts.

Figure 1-1 shows the short and long term stability of several selected oscillators, it focuses on compact clocks and shows a few commercial compact solutions and a typical fountain clock for reference. There is an evident gap in this list of frequency standards, clocks which perform on the 10^{-13} level with a package size of a few liters

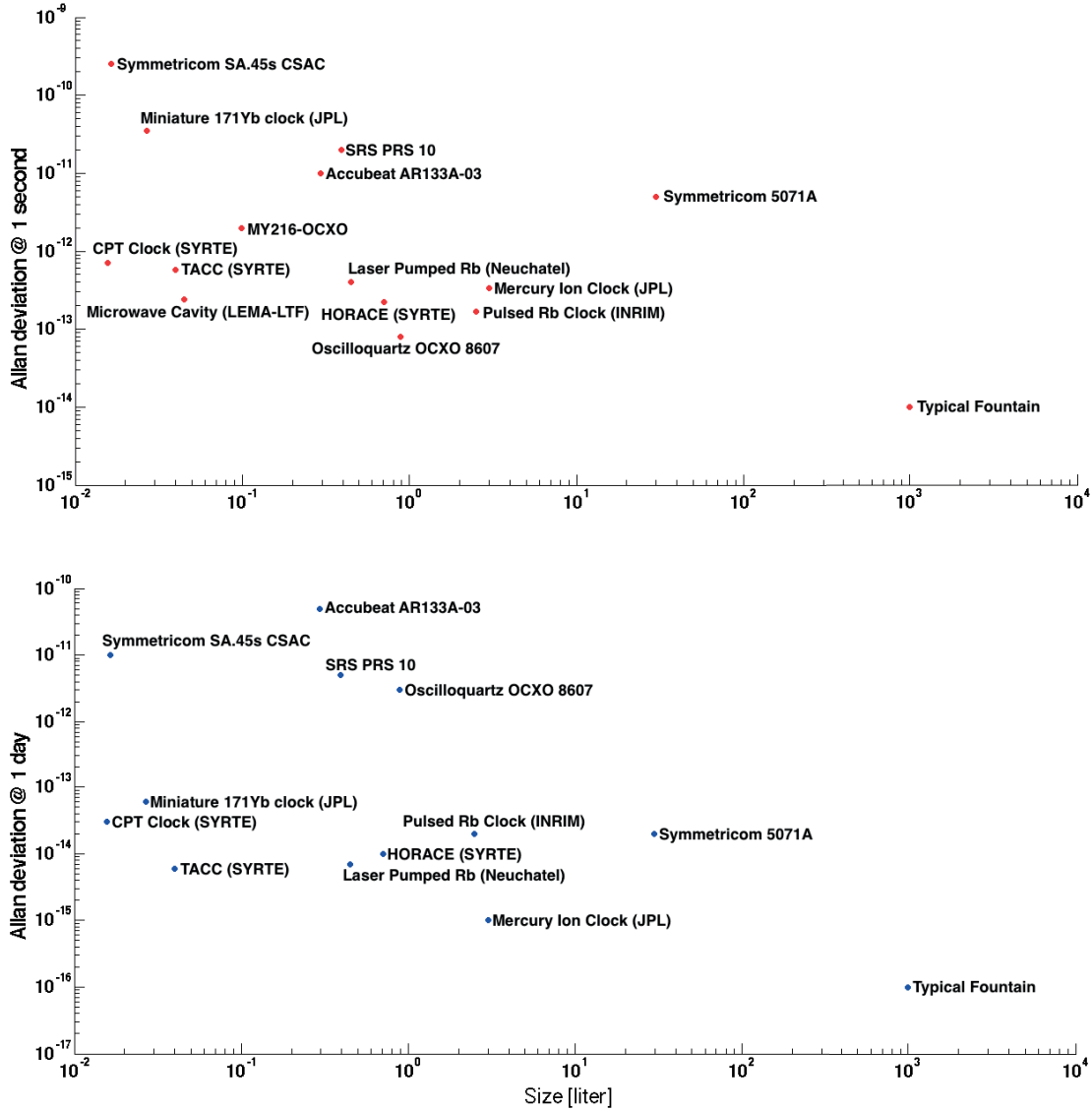


Figure 1-1: A comparison of various clocks at short (1s) and long (1day) integration times. The list is comprised of: 171Yb clock (JPL) [67], Symmetricom SA.45s [4], laser pumped Rb clock (Neuchatel) [10], pulsed optically pumped rubidium clock (INRIM) [84], CPT clock at SYRTE [35], mercury ion clock at JPL [95], HORACE clock at SYRTE [46], microwave cavity rubidium clock at LTF and LEMA [120], and our clock TACC (SYRTE).

are few, the mercury ion clock at JPL and the laser pumped rubidium clock from Neuchatel are the only compact clocks known to the author that exhibit both short and long term stabilities comparable to the ones available from modern hydrogen masers. A word must be said about the reported system sizes in figure 1-1. In the figure we have equated the clock size with that of the physics package disregarding

the contributions from the electronics, laser, vacuum and other subsystems. This was done in order not to get into speculations about the possible miniaturization of the various subsystems. In addition, when one discusses miniature clock devices the contribution of these subsystems to the overall volume of the system becomes much more important and in fact eventually dominates the total size. Laser systems for atom cooling and trapping have been successfully miniaturized to occupy a single 19 inch rack (such as in systems constructed by muQuans, Sodern or AOSense to name a just a few companies). Current supplies used in atom chip devices currently occupy a single 19 inch rack for each current source but we envisage that further miniaturization is possible or alternatively the use of permanent magnet atom chips [116] can be used to provide magnetic fields used for the trapping of atoms. Microwave sources have also been successfully miniaturized [77] and currently occupy a volume of a few liters without affecting their performance. We thus feel confident that eventually an atom chip experiment such as ours could eventually be fitted inside a setup with a total size of a few tens of liters.

The atomic clock implementation described in this manuscript, termed the Trapped Atomic Clock on a Chip (TACC) [75] exhibits a short term stability of $5.8 \cdot 10^{-13}$ at one second and integrates to the 10^{-15} level in $3 \cdot 10^4$ seconds and shows great promise for compact atomic clocks. The long interrogation times as well as the high number of atoms, provide narrow linewidths and a high signal-to-noise ratio.

Constructing a performing compact atomic clock is an important achievement with immediate applications. In the context of navigation, a precise on board atomic clocks will allow a faster acquisition of a GNSS signal and will require only 3 satellites (instead of a minimum of 4) to operate, rendering the navigation system more robust [69]. On board the satellites, more precise clocks will improve on the positioning precision [42]. Also, precise and compact atomic clocks which integrate to the 10^{-15} level promise a revolution in deep space navigation. Today, radiometric tracking of spacecrafts rely on two-way radiometry, simply because the on board clocks of current vehicles are not sufficiently precise to resolve the Doppler frequency shift used for Doppler tracking. By incorporating clocks which integrate to 10^{-15} in one day or

less, a large reduction of dead time can be achieved by using one-way radiometry. One way Doppler tracking with such clocks will improve the knowledge of the trajectory to a point that will allow for autonomous navigation of spacecrafts in deep space [45].

Trapped atom interferometer on a chip (TAIC)

Besides atomic clocks, other types of atomic sensors have been investigated. Atomic gyroscopes and accelerometers were first demonstrated more than twenty years ago [70, 102] and since then many groups have been working on improving their performance. They now equal or surpass their best classical counterparts in the field of rotation [43] and acceleration sensing [39].

Current atomic inertial sensors use freely evolving atoms during the measurement period which is at present the best known technique for high performance measurements but requires large devices, unfavorable in terms of size and integration, restricting their application to very specialized scientific experiments.

Several groups have demonstrated interferometers [15, 112], magnetic field sensors [131, 133] and plans for a gyroscope [55] on an atom chip. Being able to integrate high precision accelerometers, gyroscopes and magnetometers together with an atomic clock on one chip will open the way for cold atom based position navigation and timing (PNT) devices [50] capable of autonomous navigation independent of GNSS satellites which have inherent vulnerabilities such as Electro-Magnetic Interference (EMI) and satellite signal blockage.

We propose in this manuscript a new interferometer scheme which is in principle sensitive to acceleration using state selective MW dressed potentials which offers several advantages over previous proposals. We will show the basic building blocks of the scheme and demonstrate that coherence is maintained during operation. We will discuss the future improvements required to render the scheme fully operational and will give some estimates for its projected capabilities.

Chapter 2

Clock frequency stability

Atomic clocks are behind many everyday tasks such as synchronisation of telecommunication networks and satellite-aided navigation. Fundamental science, too, benefits from the performance of atomic clocks. Finest tests of founding theories become possible through referencing to "perfect" frequency standards [17,92] and primary clocks themselves test general relativity and the standard model [59,76,134].

The performance of atomic clocks has made a big leap by the use of laser cooling [26,29,94]. It has led to the development of atomic fountain clocks [28,72] which have overcome all major technical noise sources and have reached a stability limited by fundamental physics properties only [110], i.e. a quantum projection noise limited detection and a Fourier limited linewidth. In fact, the fountain geometry, where the atoms are launched upwards, is chosen to gain a factor 2 on the interrogation time and thus linewidth without increasing the apparatus size. Atomic fountain clocks are today's primary standards [135].

Current research on atomic clocks aims at numerous purposes and applications. The development of clocks interrogating an optical transition [37] is at one extremity and will probably lead to a new definition of the SI second. Actually, the most stable optical clock reaches $3.4 \times 10^{-16} \tau^{-1/2}$ [13]. On the other extreme is the invention of miniaturised atomic clocks such as the 16 mm³ "chip scale atomic clock" (CSAC) using thermal vapor and showing a stability of 4×10^{-11} at 1 s [73]. It has now become a commercial product. Between these two extremes lies the need for litre-

sized atomic clocks with a stability similar to the traditional hydrogen maser ($\sim 10^{-13}$ at 1 s) to serve in embarked ground and space missions [42, 45, 113]. Among the candidates [10, 35, 46, 84, 95, 120], trapped ion clocks have shown the best stability so far combined with an impressively compact physics package [96].

Here, we present a similar but complementary approach based on *neutral* atoms trapped on an atom chip. Our "Trapped Atom Clock on a Chip" (TACC) employs laser cooling and evaporative cooling to reach ultra-cold temperatures where neutral atoms can be held in a magnetic trap. Having demonstrated several tens of seconds coherence time sustained by spin self-rephasing [19, 38] we here present 100 mHz linewidth on the hyperfine transition in ^{87}Rb with 85% contrast and investigate the clock stability. The fractional frequency (in)stability reaches $5.8 \times 10^{-13} \tau^{-1/2}$ integrating down to 6×10^{-15} at 30 000 s. We identify and analyse all mayor contributions to the frequency (in)stability. The compact set-up is realised through the atom chip technology [99, 104, 127], which is now widely used for the study of ultra-cold gases and Bose-Einstein condensates [61]. Interesting regimes such as low dimensional quantum gases are reached [48, 63]. Other experiments strive for the realisation of quantum information processors [111, 126]. The realisation of atom interferometers on an atom chip [15, 55, 112, 129] is strongly appealing for surface probing [88] or inertial navigation purposes [55]. Thus, an on-chip high stability atomic clock not only provides an excellent candidate for demanding timing applications, it also takes a pioneering role among the broad range of atom chip experiments, demonstrating that experimental parameters can be mastered to the fundamental physics limit.

2.1 Atomic System

Our TACC, interrogates the hyperfine transition of ^{87}Rb . A two photon drive couples the magnetically trappable states $|1\rangle \equiv |F = 1, m_F = -1\rangle$ and $|2\rangle \equiv |F = 2, m_F = 1\rangle$, whose transition frequency exhibits a minimum in magnetic field near $B_m = 3.23$ G [62, 82]. This 2nd order dependence strongly reduces the clock frequency sensitivity on magnetic field fluctuations and atoms with different trajectories within the trap

still experience similar Zeeman shifts. Furthermore, by tuning the magnetic field at the trap bottom, the inhomogeneity from the negative collisional shift can be compensated to give a quasi position-invariant overall shift [104]. Under these ideal conditions we have observed coherence times of 58 ± 12 s [38] confirming the possibility to create a high stability clock.

2.2 Experimental Apparatus

All experimental steps, atom cooling, interrogation and detection, take place in a $4 \times 4 \times 5$ cm³ glass cell where one cell wall is replaced by the atom chip (see figure 2-2). A 25 l/s ion pump connected via standard vacuum components evacuates the cell to a pressure of $1 - 2 \times 10^{-9}$ torr. The cell is surrounded by a $10 \times 10 \times 15$ cm³ cage of Helmholtz coils. A 30 cm diameter optical table holds the coil cage as well as all beam expanders necessary for cooling and detection and is surrounded by two layers of magnetic shielding.

The timing sequence starts with a mirror MOT [98] loading $\sim 3 \times 10^6$ atoms in 4 s from the background vapor. The MOT magnetic field is generated by one of the coils and a U-shaped copper structure placed behind the atom chip [132]. Compressing the MOT followed by a 3 ms optical molasses cool the atoms to $\sim 20 \mu\text{K}$. The cloud is then optically pumped to the $|1\rangle$ state and transferred to the magnetic trap. It is gradually compressed to perform RF evaporation, which takes ~ 3 s. A 1 s decompression ramp transfers the atoms to the final interrogation trap with trap frequencies $(\omega_x, \omega_y, \omega_z) = 2\pi \times (2.7, 92, 74)$ Hz located $350 \mu\text{m}$ above the surface. It is formed by two currents on the chip and two currents in two pairs of Helmholtz coils, which are supplied by homebuilt highly stable current supplies with relative (in)stability $< 10^{-5}$ at 3 A [101]. The final atom number is $2 - 4 \times 10^4$ and their temperature ~ 80 nK. The density is thus with $\bar{n} \approx 1.5 \times 10^{11}$ atoms/cm³ so low that the onset of Bose-Einstein condensation would occur at 5 nK. The trap lifetime $\gamma^{-1} = 6.9$ s is limited by background gas collisions.

The clock transition is interrogated via two-photon (microwave + radiofrequency)

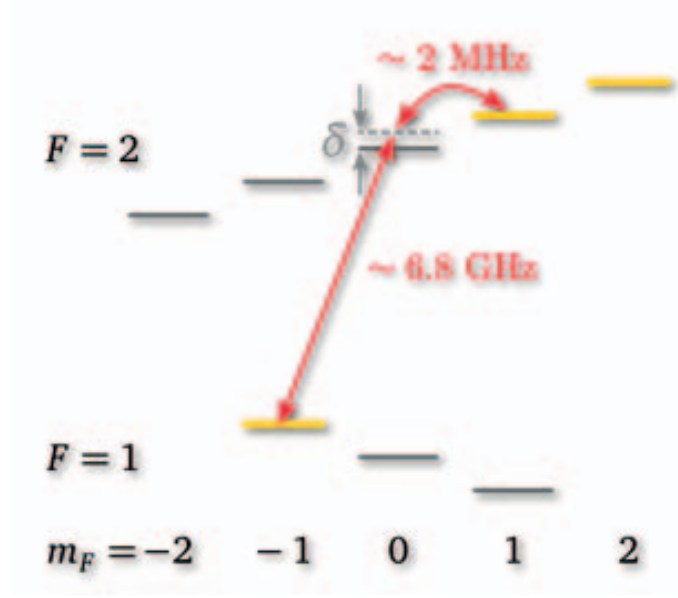


Figure 2-1: The two clock states $|1, -1\rangle$ and $|2, 1\rangle$ are coupled via a 2-photon transition, MW+RF, where the microwave is tuned ≈ 500 kHz above the $|1, -1\rangle \rightarrow |2, 0\rangle$ transition.

coupling (see fig 2-1), where the microwave is detuned 500 kHz above the $|1\rangle$ to $|F = 2, m_F = 0\rangle$ transition. The microwave originates from the evanescent field of a three-wire coplanar waveguide on the atom chip [75]. The close proximity of the atoms allows to reach single photon Rabi frequencies of a few kHz with only moderate power (~ 0 dBm). The waveguide furthermore avoids the use of a bulky microwave cavity. The microwave signal is generated by a homebuilt synthesiser which multiplies a 100 MHz reference signal derived from a commercial hydrogen maser to the microwave frequency without degradation of the maser phase noise [97]. The actual phase noise is detailed in section 2.4.2. The RF signal of ~ 2 MHz comes from a commercial DDS which supplies a "standard" wire parallel to the waveguide. The two-photon Rabi frequency is 3.2 Hz so that a $\pi/2$ pulse takes 77.65 ms.

Detection is performed via absorption imaging. A strongly saturating beam [100] is imaged onto a back illuminated, high quantum efficiency CCD camera with frame transfer. 20 μ s illumination without and with repumper 5.5 ms and 8.5 ms after trap release probes the F=2 and F=1 atoms independently. Numerical frame recomposition [89] generates the respective reference images and largely reduces optical fringes.

The number of atoms in each state $N_{1,2}$ is extracted by summing the pixel counts from a state selective detection image. The transition probability is calculated as $P = N_1/(N_1 + N_2)$ accounting for total atom number fluctuations. The actual detection noise is discussed in section 2.4.1. The total time of one experimental cycle is 16 s including the $T_R = 5$ s Ramsey time.

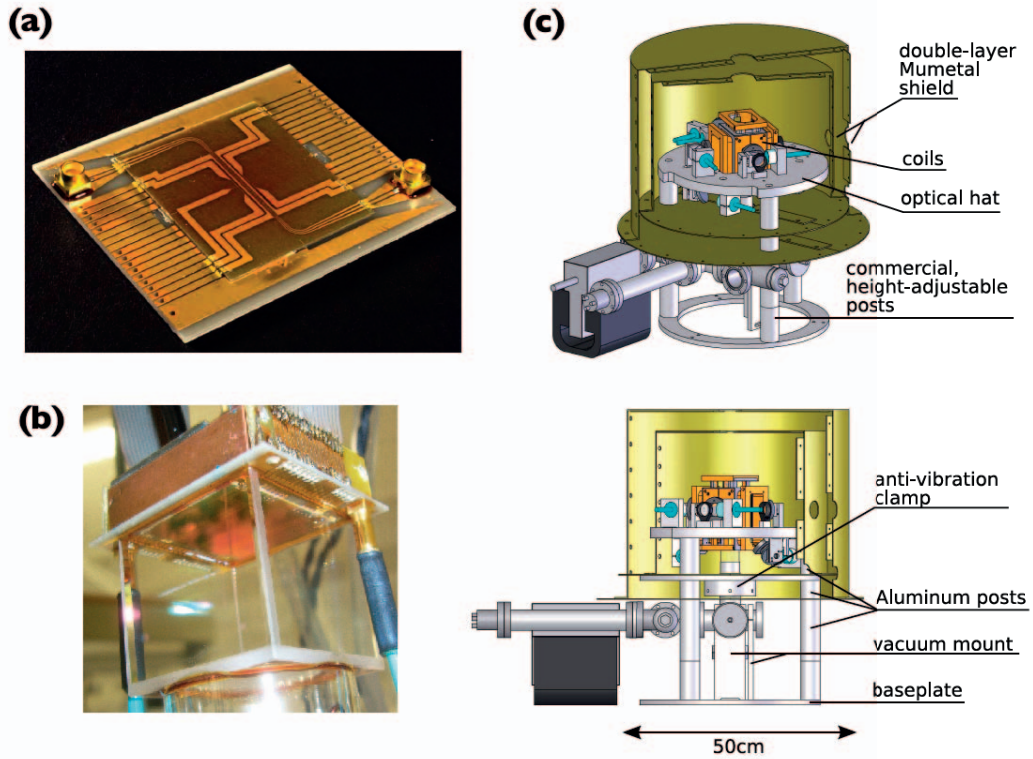


Figure 2-2: Our experimental setup. a. The atom chip has two layers, the science chip ($24 \times 28 \times 0.25 \text{ mm}^3$) is glued on top of a base chip ($38 \times 45.5 \times 0.8 \text{ mm}^3$) and coated with a dielectric layer which is reflective for 780 nm radiation. The double layer chip constitutes one of the facets of the vacuum cell (b) which is a commercial Pyrex spectroscopy cell ($35 \times 35 \times 32.5 \text{ mm}^3$) [8] treated with anti reflection coating on the outside facets. The cell is embedded in a $10 \times 10 \times 15 \text{ cm}^3$ cage of Helmholtz coils (c) and a 30 cm diameter optical table holds the coil cage as well as all beam expanders necessary for cooling and detection and is surrounded by two layers of magnetic shielding. We reach vacuum levels in the low 10^{-9} mbar. The core physics package is around 50 ml in volume and is thus a promising technology for the creation of compact atomic sensors.

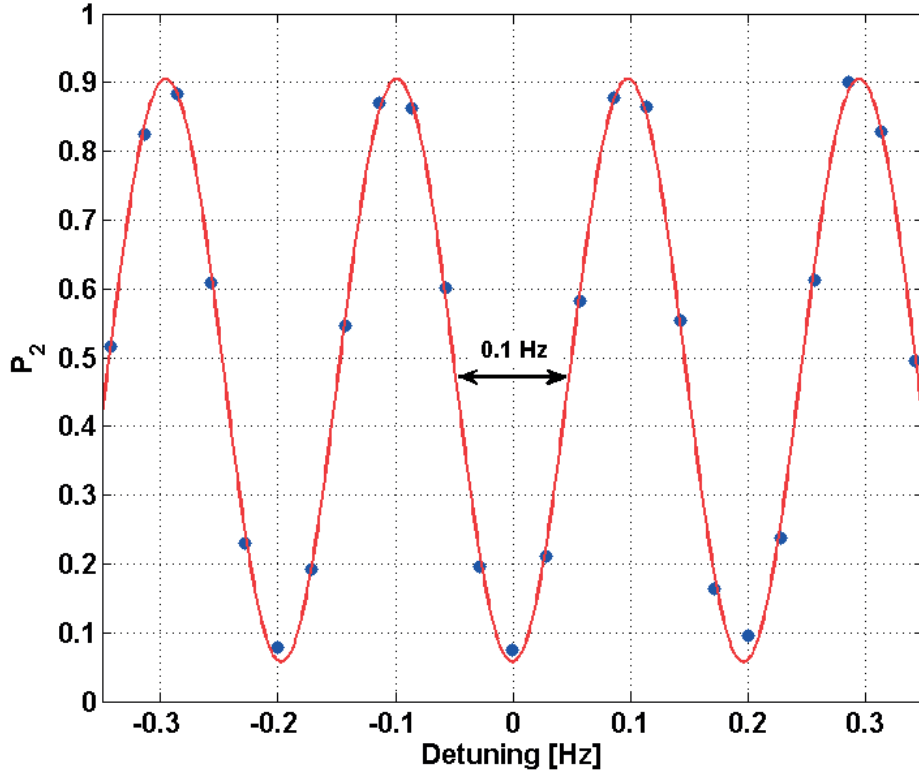


Figure 2-3: Typical Ramsey fringes recorded at $T_R = 5$ s scanning the local oscillator detuning. Each point corresponds to a single experimental realisation. One identifies the Fourier limited linewidth of 100 mHz and the very good contrast of 85%.

2.3 Stability Measurement

Prior to any stability measurement we record the typical Ramsey fringes. We repeat the experimental cycle while scanning $\nu_{LO} = \nu_{MW} + \nu_{RF}$ over ~ 3 fringes. Doing so for various Ramsey times T_R allows to identify the central fringe corresponding to the atomic frequency. Figure 2-3 shows typical fringes for $T_R = 5$ s, where each point corresponds to a single shot. One recognises the Fourier limited linewidth of 100 mHz corresponding to a $\sim 10^{11}$ quality factor. The contrast is remarkably 85% even after a 5 seconds integration. A sinusoidal fit gives the slope at the fringe half height $dP/d\nu = 13.4/\text{Hz}$, which is used in the following stability evaluation to convert the detected transition probability into frequency.

Evaluation of the clock stability implies repeating the experimental cycle several

thousand times. The clock is free-running, i.e. we measure the transition probability at each cycle, but we do not feedback to the interrogation frequency ν_{LO} . Only, an alternation in successive shots from a small fixed negative to positive detuning (± 50 mHz) probes the left and right half-height of the central fringe. The difference in P between two shots gives the variation of the central frequency independent from detection or microwave power drifts. In the longest run, we have repeated the frequency measurement over 18 hours.

The measured frequency data is traced in figure 2-4 versus time. Besides shot-to-shot fluctuations one identifies important long-term variations. Correction of the data with the atom number (by a procedure we will detail in the next chapter) results in substantial improvement (figure 2-4(b)). Figure 2-5 shows the Allan standard deviation [7] of the uncorrected and corrected data. The first data point occurs at $\tau = 16$ s corresponding to the cycle time. Up to 100 s the frequency fluctuations follow a white noise behaviour characterised by the typical $\tau^{-1/2}$ scaling. The uncorrected data follows $7.9 \times 10^{-13} \tau^{-1/2}$, the corrected data $5.8 \times 10^{-13} \tau^{-1/2}$. At $\tau \approx 1000$ s, the fluctuations are above the white noise behaviour but decrease again at $\tau > 10^4$ s to almost join the initial white noise extrapolation. This behaviour of the Allan standard deviation is characteristic for an oscillation at a few 10^3 s half-period. Indeed, this oscillation is visible in the raw data in figure 2-4. Table 2.1 gives a list of identified contributions to the clock frequency noise. Treating them as statistically independent and summing their squares gives a shot-to-shot frequency fluctuation of 5.9×10^{-13} at 1 s identical to the measured stability. We have thus identified all dominant noise sources giving a solid basis for future improvements. In the following we will discuss each noise contribution in detail.

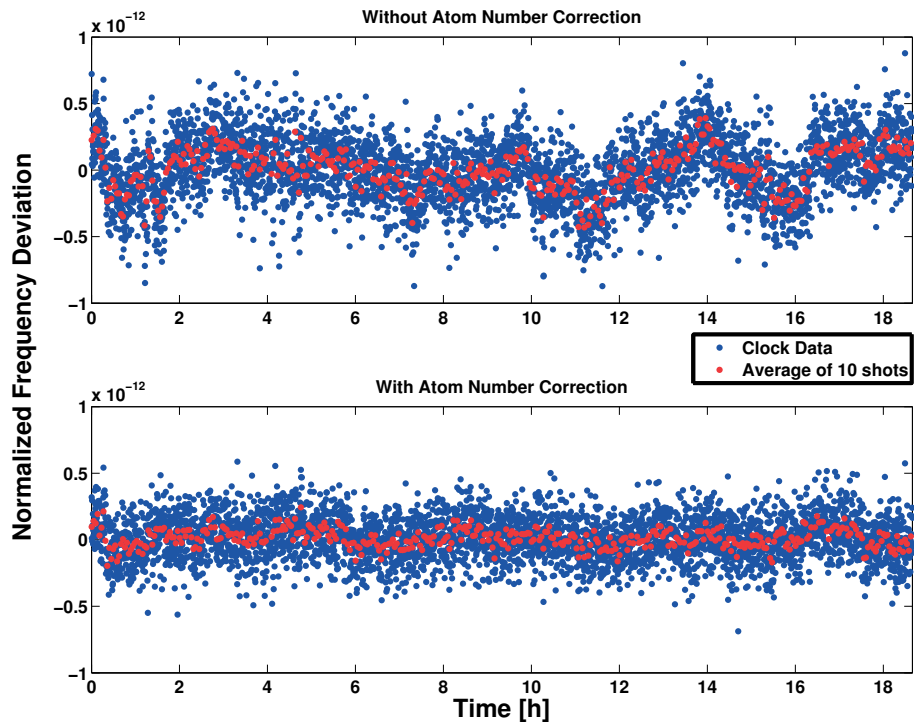


Figure 2-4: Normalized frequency deviation when repeating the clock measurement over 18 h. Before the correction with the atom number (above) and after the correction (below). Blue dots are single shots, red dots represent an average of 10 shots.

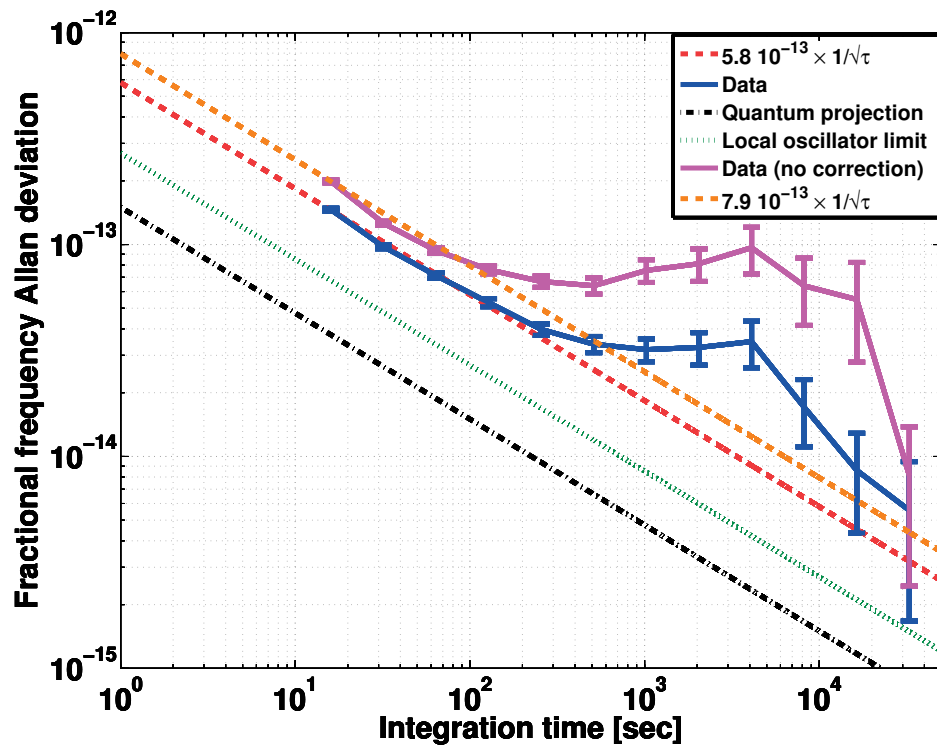


Figure 2-5: Allan deviation of the clock stability with (blue line) and without (pink line) atom number correction. The quantum projection noise and the local oscillator noise contributions are given as a reference.

Contribution	Amplitude $\sigma_y@1s$
Measured, without correction	7.9×10^{-13}
Measured, after correction	5.8×10^{-13}
Temperature fluctuations	3.8×10^{-13}
Magnetic field fluctuations	2.6×10^{-13}
Local oscillator	2.7×10^{-13}
Quantum projection	1.5×10^{-13}
Correction	1.3×10^{-13}
Symmetric losses	1.1×10^{-13}
Detection	0.9×10^{-13}
Total Estimate	5.9×10^{-13}

Table 2.1: TACC Noise Budget. Temperature fluctuations comprise the largest noise contribution followed by magnetic field fluctuations and local oscillator noise. Increasing tof we could improve our estimation of the temperature and use it to correct for its fluctuations. Sacrificing the detection noise might be a good tradeoff as it is the lowest contribution to the noise budget.

2.4 Noise Analysis

In a passive atomic clock, electromagnetic radiation generated from an external local oscillator (LO) interacts with an atomic transition (fig. 2-6) . The atomic transition frequency is probed by means of spectroscopy. The detected transition probability is used to correct ν_{LO} such that it represents the atomic frequency. The so steered LO signal is the useful clock output ready for cycle counting and synchronisation of secondary devices. When concerned with the stability of the output frequency, we have to analyse the noise of each element within this feed-back loop, i.e.

1. fluctuations of the atomic transition frequency induced by interactions between the atoms themselves or with the environment,
2. noise from imperfect detection,

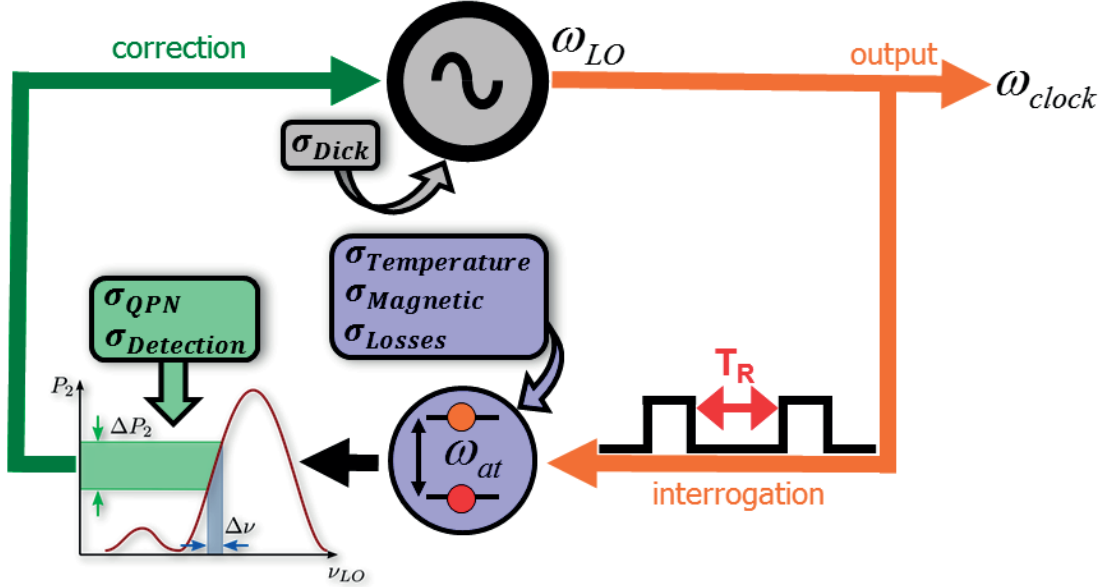


Figure 2-6: Schematics of the clock operation loop. A local oscillator (LO) interrogates the atomic transition via Ramsey spectroscopy. The detuning of the LO from the atomic transition is obtained from detecting the relative occupation of the two states. The result is fed back to the LO to lock the output signal to the atomic transition. In the scheme we show the various noise sources as they appear in the sequence. Temperature, magnetic and atom losses fluctuations affect the atomic transition directly whereas the quantum projection and detection noises affect the detection of the relative population. The LO noise degrades the stability due to an aliasing process known as the Dick effect.

3. uncorrected fluctuations of the LO frequency known as Dick effect.

We now analyse these three noise types for our clock. We begin by describing the most intuitive contribution (2. detection noise) and finish by the most subtle (1. fluctuations of the atomic frequency).

2.4.1 Detection and Quantum Projection Noise

The clock frequency is deduced from absorption imaging of the atom cloud in each clock state. N_1 and N_2 are obtained by summing the camera pixels over a square region corresponding to 3 times the cloud width. Photon shot noise and optical fringes lead to ghost atoms σ_{det} that add to the true atom number. Analysing blank

images, we confirm that σ_{det}^2 increases as the number of integrated pixels and that optical fringes have efficiently been suppressed [89]. However, the scaling has led to the choice of short times-of-flight where the atoms occupy fewer pixels ¹. Supposing the same remaining σ_{det} for both states we get for the transition probability noise $\sigma_{P,det} = 2^{-1/2}\sigma_{det}N^{-1}$ with $N = N_1 + N_2$.

Another degradation $\sigma_{P,lf}$ may occur if the efficiency varies between the $|1\rangle$ and $|2\rangle$ detection. As the two are separated by a 3 ms delay, this may arise from laser frequency fluctuations. It induces a direct error on P and is independent from the atom number.

Quantum projection noise is a third cause for fluctuations in P . This fundamental noise arises from the fact that the detection projects the atomic superposition state onto the pure clock states. Before detection, the atom is in a near-to-equal superposition of $|1\rangle$ and $|2\rangle$. The projection then can result in either pure state with equal probability giving $\sigma_{QPN} = 1/2$ for one atom. Running the clock with N (non-entangled) atoms is equivalent to N successive measurement resulting in $\sigma_{P,QPN} = 1/(2\sqrt{N})$ at 1 shot.

We quantify the three noise types from an independent measurement: Only the first $\pi/2$ pulse is applied and P is immediately detected. The measurement is repeated for various atom numbers and $\sigma_P(N)$ is extracted. In addition to the above three noise sources, this procedure is sensitive to fluctuations of the Rabi frequency $\sigma_{P,Rf}$ which also give N -independent P fluctuations. They can not be distinguished from $\sigma_{P,lf}$, however, as we will show below, this noise is negligible. Figure 2-7 shows the measured σ_P at one shot versus N . Considering the noise sources statistically independent, we fit the data by $\sigma_P^2 = \sigma_{det}^2/N^2 + 1/4N + \sigma_{P,lf+Rf}^2$ and find $\sigma_{det} = 59$ atoms and $\sigma_{P,lf+Rf} < 10^{-4}$. σ_{det} is equivalent to an average of ≈ 0.06 atoms/pixel reaching almost single atom detectivity for our very typical absorption imaging system. The low σ_{lf+Rf} proves an excellent microwave power stability which may be of use in other experiments, in particular quantum information processing.

During the stability measurement of figure 2-4 we detect about 20 000 atoms which

¹The minimum time-of-flight is given by the onset of optical diffraction at high optical density.

is equivalent to $\sigma_{y,QPN} = 1.5 \times 10^{-13} \tau^{-1/2}$. Here we have used the spectroscopic response based on the true contrast C as measured in figure 2-3.

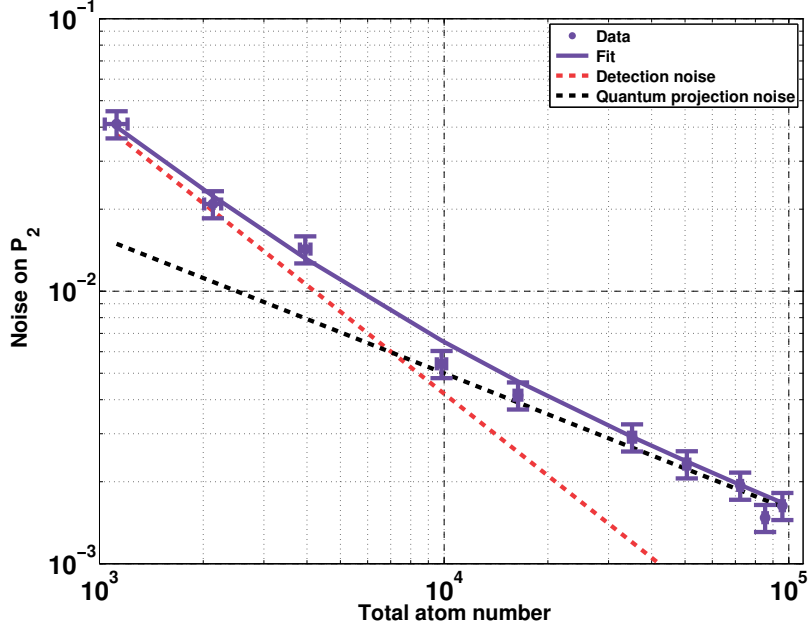


Figure 2-7: Characterization of the detection noise. The Allan deviation at one shot is plotted as a function of the total atom number. We fit the data with the quadratic sum of the detection noise σ_{N_i} , the quantum projection noise $\frac{1}{2\sqrt{N}}$ and the Rabi frequency noise $\sigma_{P_2,Rabi}$. The fit gives $\sigma_{N_i} = 59$ atoms and a negligible value for $\sigma_{P_2,Rabi}$ smaller than 10^{-4} .

2.4.2 Local oscillator noise

The stability evaluation gives the LO frequency compared to the atomic frequency with one point per cycle. The cyclic operation constitutes periodic sampling of the LO frequency fluctuations and it is well-known from numerical data acquisition, that periodic sampling leads to aliasing. It folds high Fourier frequency LO noise close to multiples of the sampling frequency T_C^{-1} back to low frequency variations, which degrade the clock stability. Thus even high Fourier frequency noise can degrade the clock signal. The degradation is all the more important as the dead time is long and the duty cycle $d = T_R/T_C$ is low.

This stability degradation $\sigma_{y,Dick}$ is known as the Dick effect. It is best calculated

using the sensitivity function $g(t)$ [109]. During dead-time $g = 0$ whereas during T_R , when the atomic coherence $|\psi\rangle = 2^{-1/2}(|1\rangle + e^{i\phi}|2\rangle)$ is fully established $g = 1$. During the first Ramsey pulse, when the coherence builds up, g increases for a square pulse as $\sin \Omega t$ and decreases symmetrically for the second pulse (see Fig. 2-8). Then the

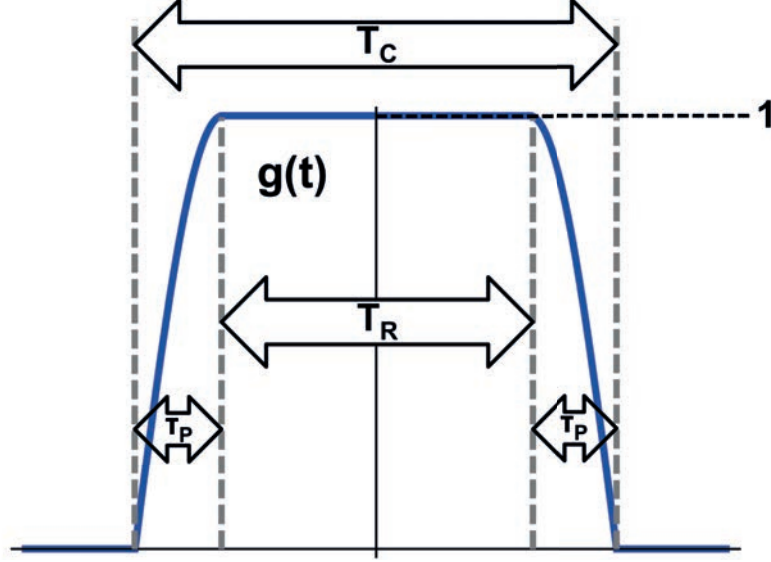


Figure 2-8: The sensitivity function $g(t)$. During the dead time $g = 0$ whereas during T_R the atomic coherence is fully established and $g = 1$. During the Ramsey pulse with length τ_P the coherence builds up and g increases as $\sin \Omega t$.

interrogation outcome is

$$\delta\nu = \frac{\int_{T_C/2}^{T_C/2} (\nu_{at}(t) - \nu_{LO}(t)) g(t) dt}{\int_{T_C/2}^{T_C/2} g(t) dt} \quad (2.1)$$

with

$$g(t) = \begin{cases} a \sin \Omega(T_R/2 + \tau_p + t) & \tau_p \quad T_R/2 \leq t \leq T_R/2 \\ a \sin \Omega \tau_p & T_R/2 \leq t \leq T_R/2 \\ a \sin \Omega(T_R/2 + \tau_p - t) & T_R/2 \leq t \leq T_R/2 + \tau_p \\ 0 & \text{otherwise} \end{cases} \quad (2.2)$$

Typically $\Omega \tau_p = \pi/2$ and, for operation at the fringe half height, $a = \sin \Delta_m T_R = 1$. (The sensitivity function is easily understood by visualising the trajectory of a spin 1/2 on the Bloch sphere.) Due to the periodicity of $g(t)$ it is convenient to use

its Fourier transform

$$g_m = \frac{1}{T_C} \int_{-T_C/2}^{T_C/2} g(t) \cos(2\pi m t/T_C) dt. \quad (2.3)$$

Using $S_y^f(f)$, the power spectral density of the LO noise, the contribution to the clock stability becomes the sum over all harmonics g_m [109]

$$\sigma_{y,Dick}^2(\tau) = \frac{1}{\tau} \sum_{m=1}^{\infty} \left(\frac{g_m}{g_0} \right)^2 S_y^f(m/T_C) \quad (2.4)$$

The $(g_m/g_0)^2$ are shown as points in figure 2-10 for our conditions. The contribution of the first few harmonics is clearly the strongest, but higher harmonics may well contribute when all summed up.

To find the Dick effect for our clock we divide the local oscillator into two principal components: the 100 MHz reference signal derived from the hydrogen maser and the frequency multiplication chain generating the 6.8 GHz interrogation signal. We characterise each independently by measuring the phase noise spectrum $S_\phi(f)$. The fractional frequency noise $S_y^f(f)$ used in eqn 2.4 is obtain from a simple differentiation as $S_y^f(f) = \frac{f^2}{\nu_0^2} S_\phi(f)$ where ν_0 is the transition frequency(See appendix A for a derivation).

We characterize the frequency multiplication chain by comparing it to a second similar model also constructed in-house. The two chains are locked to a common 100 MHz reference and their phase difference at 6.8 GHz is measured as a DC signal using a phase detector and a SR760 FFT spectrum analyzer. The measured signal is divided by $\sqrt{2}$ assuming equal noise contributions from the two chains. The beat is performed at 6.8 GHz and values are scaled to 100 MHz by subtracting 36.7 dB. The phase noise spectrum is shown in figure 2-9. It features a $1/f$ behaviour up to $f = 10$ Hz and reaches a phase flicker floor of -150 dB rad²/Hz at 1 kHz. The peak at $f = 200$ Hz is due to the phase lock inside the chain of a 100 MHz quartz to the reference signal.

The 100 MHz reference signal is generated by a 100 MHz quartz locked to a

5 MHz quartz locked with a bandwidth of 40 mHz to an active hydrogen maser (VCH-1003M). We measure this reference signal by beating it against a 100 MHz signal derived from a cryogenic sapphire oscillator (CSO) [81] which is itself locked to the maser derived reference signal but with a time constant of ~ 1000 s. This being much longer than our cycle time, we can, for our purposes, consider the two as free running. The CSO is known from prior analysis [24] to be at least 10 dB lower in phase noise than the reference signal for Fourier frequencies higher than 0.1 Hz, thus the measured noise can be attributed to the reference signal for the region of the spectrum where our clock is sensitive to LO noise ($1/T_C$ and above). The phase noise spectrum is also shown in figure 2-9. Several maxima characteristic of the several phase locks in the systems can be identified. At low Fourier frequencies, the 100 MHz noise is clearly above the chain noise. At high frequencies both have equivalent phase noise. For all frequencies, both are well above the noise floor of our measurement system. The noise of the reference signal being dominant at the scale of our cycle time, we neglect the chain noise in the following.

Combining the noise spectra with the sensitivity function Fourier coefficients one realises that Fourier frequencies in the mHz range play a considerable role, but their precise measurement is challenging as they are subject to temperature drifts in the analysis instruments. In order to verify the noise spectrum we use data from the atomic fountain clock FO1 exceptionally running with the 100 MHz reference signal rather than the usual CSO. FO1's frequency stability usually being in the low $10^{-14}\tau^{-1/2}$, here the stability is entirely dominated by the reference signal noise. Using the fountain cycle of 1.36 s and Ramsey time of 0.53 s we predict its frequency stability from the spectrum of figure 2-10 and find perfect agreement with an actual stability measurement (figure 2-11). Furthermore, to simulate the much longer cycle time of TACC and resulting sensitivity at sub-Hz Fourier frequencies, we select only every 12th point from the fountain data and compare the stability with the Dick effect prediction. Again we find perfect agreement giving us confidence in the phase noise characterisation of the 100 MHz reference signal.

Using equation 2.4 with the TACC Ramsey and cycle time, we estimate the Dick

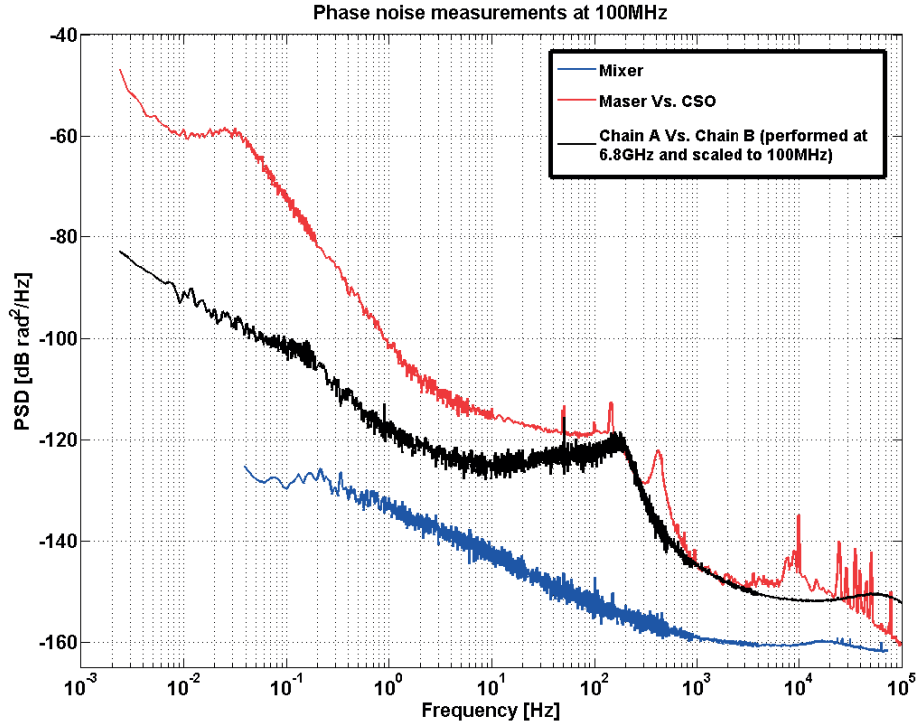


Figure 2-9: Phase noise power spectral density (PSD) of the Quartz filtered Maser reference (red) was obtained by beating it at 100MHz with the output of a cryogenic sapphire oscillator using a low noise mixer (PD-121) followed by a low pass filter. The PSD of our synthesizer chain (black) was measured by beating it with a similar chain from another group and was divided by $\sqrt{2}$ assuming equal noise contributions from the two chains. The measurement was performed with both chains locked to the same 100MHz reference and then beat by mixing the outputs at 6.8GHz. The noise level was then shifted by $10 * \log_{10}(6.8 * 10^9 / 100 * 10^6) \approx 36.7dB$ to be compared with the noise level of the Quartz filtered Maser which was performed at 100 MHz. The noise floor of the mixer is shown in blue. The noise of the 100 MHz reference signal dominates and we will neglect the added noise from the chain in the following.

effect contribution to be $\sigma_{y,Dick} = 2.7 \times 10^{-13} \tau^{-1/2}$. Thus, the Dick effect represents the third biggest contribution to the noise budget (table 2.1). This is due to the important dead time and the long cycle time which folds-in the LO noise spectrum where it is strongest. Improvement is possible, first of all, through reduction of the dead time, currently dominated by the 4 s MOT loading phase and the 3 s evaporation cooling stage. Options for faster loading include pre-cooling in a 2D MOT. Utilization of a better local oscillator like the cryogenic sapphire oscillator seems obvious but defies the compact design. Alternatively, generation of low phase noise microwaves

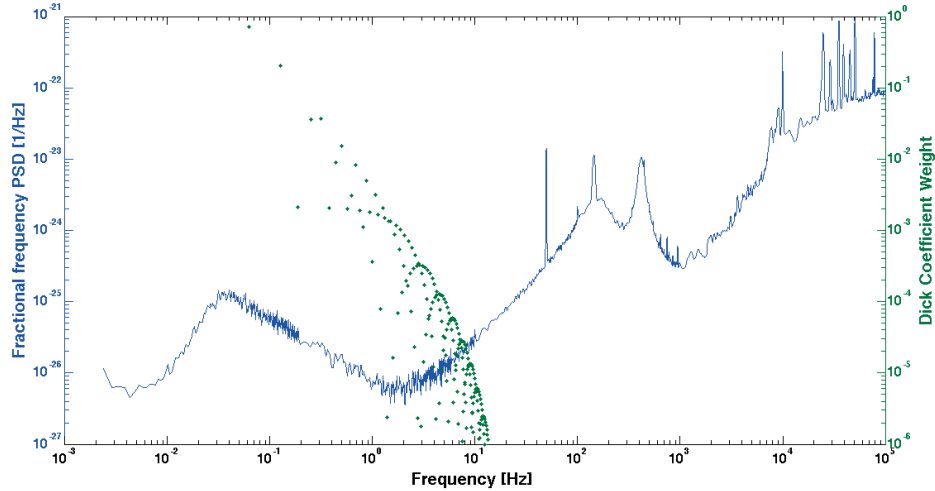


Figure 2-10: Same data as in figure 2-9 now expressed as relative frequency fluctuations using $S_y = \left(\frac{f}{f_0}\right)^2 S_\phi$. Shown are also the Dick effect coefficients $\left(\frac{g_m}{g_0}\right)^2$ for our cycle time of $T_C = 16$ s and Ramsey time $T_R = 5$ s. The lower harmonics give the strongest contribution in the Dick effect calculation.

from an ultra-stable laser with femtosecond comb has been demonstrated by several groups and on-going projects aim at miniaturisation of such systems. If a quartz local oscillator remains the preferred choice, possibly motivated by cost, non-destructive detection constitutes a promising approach for high duty cycle [12, 130].

2.4.3 Fluctuations of the atomic frequency

Atom number fluctuation

Having characterised the fluctuations of the LO frequency, we now turn to fluctuations of the atomic frequency. We begin by atom number fluctuations. Due to the trap confinement and the ultra-cold temperature, the atom density in TACC is 4 orders of magnitude higher than what is typically found in a fountain clock. Thus atom-atom interactions are strong and their effect on the atomic frequency must be taken into account even though ^{87}Rb presents a substantially lower collisional shift than the standard ^{133}Cs . Indeed, when plotting the measured clock frequency against the detected atom number $N = N_1 + N_2$, which fluctuates by 2-3% at 1 shot, we find a strong correlation (figure 2-12). The distribution is compatible with a linear fit with

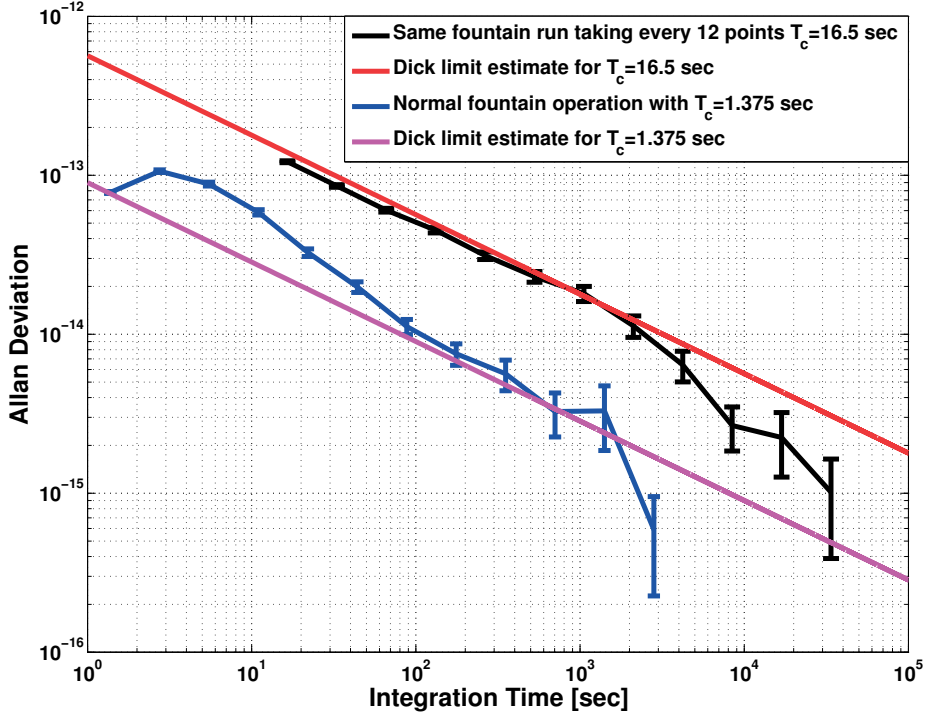


Figure 2-11: The Allan deviation of the fountain (blue line) running with the 100 MHz reference signal as its local oscillator and the Dick effect estimation (red) based on the PSD measurements in fig 2-10. The black line was generated by taking the same data as for the blue but taking a sub-sample consisting of every 12th point, thus creating a virtual measurement with a cycle time of 16.5 seconds which is close to our cycle time of 16 seconds. It allows us to test our PSD measurements and Dick effect calculations for a similar system. The good agreement validates our estimate.

slope $k = -2.7 \mu\text{Hz}/\text{atom}$. In order to compare this value with a theoretical estimate we use the mean field approach and the s-wave scattering lengths a_{ij} which depend on the atomic states only [62].

$$\Delta\nu_C = \frac{2\hbar}{m}n(\vec{r})((a_{22} - a_{11}) + \theta(2a_{12} - a_{11} - a_{22})) \quad (2.5)$$

$n(\vec{r})$ is the position dependent density and $a_{11} = 100.44a_0$, $a_{22} = 95.47a_0$, $a_{12} = 98.09a_0$ with $a_0 = 0.529 \times 10^{-10}$ m are the scattering lengths [62]. We assume perfect $\pi/2$ pulses and so $\theta \equiv (N_1 - N_2)/N = 0$. Integrating over the Maxwell-Boltzmann

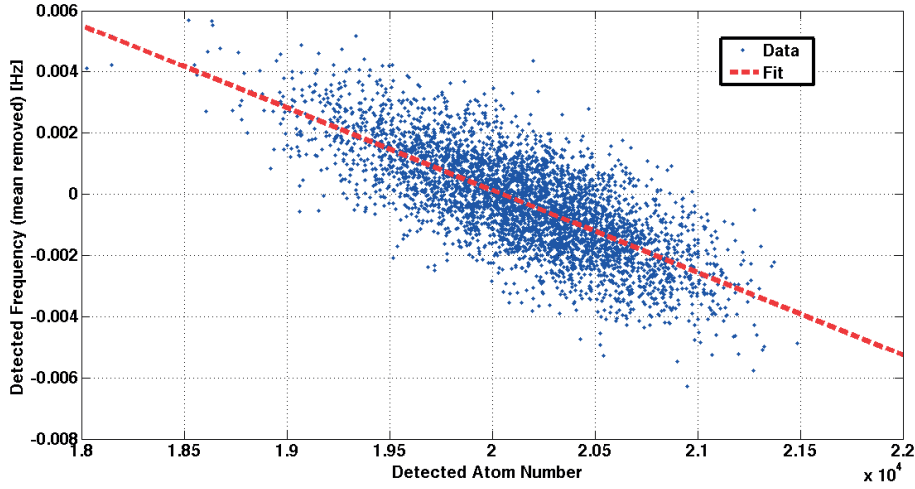


Figure 2-12: Correlation between the atom number and the measured atomic frequency for the data in figure 2-4. Fitting this with a linear regression we get a slope of $k = -2.7 \times 10^{-6} \text{ Hz/atom}$. This allows us to correct for atom number fluctuations during the experimental run. We obtain the same value from theory [62] assuming a cloud temperature of $T = 80 \text{ nK}$ which agrees with independent temperature measurements.

density distribution ² we get

$$\overline{\Delta\nu_C} = N \times \frac{-\hbar(a_{11} - a_{22})\sqrt{m}\omega_x\omega_y\omega_z}{4(\pi k_B T)^{3/2}} \quad (2.6)$$

We must furthermore consider that the atom number decays during the $T_R = 5 \text{ s}$ since the trap life time is $\gamma^{-1} = 6.9 \text{ s}$. We thus replace N by its temporal average.

$$\begin{aligned} \overline{N} &= \frac{1}{T_R} \int_0^{T_R} N_i e^{-\gamma t} dt \\ &= N_i \frac{1 - e^{-\gamma T_R}}{\gamma T_R} \\ &= N_f \frac{e^{\gamma T_R} - 1}{\gamma T_R} \\ &\approx 1.47 N_f \end{aligned} \quad (2.7)$$

where N_i and N_f are the initial and final atom numbers. Note that N_f is the actually detected atom number. Using $T = 80 \text{ nK}$, which is compatible with an independent

² For our conditions $k_B T / \hbar \omega_{x,y,z} > 20$ and the ensemble can be treated as non-degenerate.

measurement, we recover the experimental collisional shift of $k = -2.7 \mu\text{Hz}/(\text{detected atom})$. It is equivalent to an overall collisional shift of $\overline{\Delta\nu_C} = -54 \text{ mHz}$ for $N_f = 20\,000$.

Using k and the number of atoms detected at each shot we can correct the clock frequency for fluctuations. The corrected frequency is given in figure 2-4 (b) showing a noticeable improvement in the short-term and long term stability over the uncorrected data (fig 2-4(a)). Equivalently, the Allan deviation indicates a clock stability of $5.8 \times 10^{-13} \tau^{-1/2}$ at short term as compared to $7.9 \times 10^{-13} \tau^{-1/2}$ for the uncorrected data. At long term the improvement is even more pronounced changing from 6×10^{-14} to 8×10^{-15} at 16 000 s. Atom number corrections are performed in atomic fountain clocks, too, but rather with the aim of evaluating the accuracy [41]. There the atom number is deliberately varied, typically by a factor 2, and the stability degraded. In TACC the natural fluctuations are sufficient to find the collisional shift coefficient. Furthermore, our measurement shows perfect agreement with theory so that the theoretical coefficient can be used from the first shot on, without the need for post-treatment.

Limitations to the atom number correction While we have demonstrated the efficiency of the atom number correction, the procedure has imperfections for two reasons: The first, of technical origin, are fluctuations in the atom number detectivity as evaluated in section 2.4.1. The second arises from the fact that atom loss from the trap is a statistical process and the exact moment when an atom is lost is unknown. For the first, we get $\sigma_{y,correction} = \nu_0^{-1} |k| \sqrt{2} \sigma_{N,det} \sqrt{\frac{T_C}{\tau}} = 1.3 \times 10^{-13} \tau^{-1/2}$ This value is well below the measured clock stability, but may become important when other noise sources are eliminated. It can be improved by better detection, in particular at shorter time-of-flight where the cloud occupies fewer camera pixels, or reduction of the atom density. The second cause, the statistical nature of atom loss, translates into fluctuations that in principle cannot be corrected. If an atom is lost immediately after the first $\pi/2$ pulse it has almost no contribution to the collisional shift. On the contrary, if it is lost just before the second pulse, it contributes fully, but the detected

N_f is the same. Only in the limit of infinite atom number, would this fluctuation disappear. To estimate this contribution we consider a cloud with N_i initial atoms. At time t , the probability for a given atom to still be trapped is $e^{-\gamma t}$ and the probability to have left the trap is $1 - e^{-\gamma t}$. Given N_i , the probability P to have N_t atoms at t is proportional to $e^{-N_t \gamma t} (1 - e^{-\gamma t})^{N_i - N_t}$ and to the number of possible combinations:

$$P(N_t \text{ given } N_i) = \frac{N_i!}{N_t!(N_i - N_t)!} e^{-N_t \gamma t} (1 - e^{-\gamma t})^{N_i - N_t} \quad (2.8)$$

The sum of this binomial distribution over all $0 \leq N_t \leq N_i$ is by definition normalised to 1. However, we are interested in the opposite case: since we detect the final atom number N_f at $t = T_R$, we search the probability of finding N_t given N_f .

$$P(N_t \text{ given } N_f) = A \frac{N_t!}{N_f!(N_t - N_f)!} e^{-N_f \gamma t} (1 - e^{-\gamma t})^{N_t - N_f} \quad (2.9)$$

The binomial distribution is formally the same as (2.8) after replacing $N_t \rightarrow N_f$ and $N_i \rightarrow N_t$, but now normalisation sums over $0 \leq N_t < \infty$ and thus $A = e^{-\gamma t}$. Calculation of the resulting frequency fluctuations sums over all N_t and integrates (2.9) over time (see 2.6). To do so it is convenient to approximate the binomial distribution by the Gaussian

$$P(N_t \text{ given } N_f) = A (2\pi\eta)^{-1/2} e^{-(N_f - \eta(1 - e^{-\gamma t})^{-1})^2 / 2\eta} \quad (2.10)$$

with $\eta = N_t e^{-\gamma t} (1 - e^{-\gamma t})$ to obtain the analytic formula

$$\sigma_{y, \text{losses}} = \frac{k}{\nu_{at} \gamma T_R} \sqrt{N_f e^{-2\gamma T_R} (1 - 2\gamma T_R e^{-\gamma T_R} - e^{-2\gamma T_R})} \quad (2.11)$$

For our parameters $\sigma_{y, \text{losses}} = 1.1 \times 10^{-13} \tau^{-1/2}$. This can only be improved by increasing the trap lifetime well beyond the Ramsey time. For our set-up, this implies better vacuum with lower background pressure. Alternatively one can perform a non-destructive measurement of the initial atom number [74, 80].

Magnetic Field and Temperature Fluctuations

We have analysed the effect of atom number fluctuations on the clock frequency. Two other experimental parameters strongly affect the frequency: the temperature and the magnetic field. Their influence can be evaluated by measuring the clock stability for different magnetic fields at the trap center. We begin by modelling the dependence of the clock frequency.

We operate our clock near the magic field $B_m \approx 3.23$ G for which the transition frequency has a minimum of -4497.31 Hz with respect to the field free transition [62].

$$\Delta\nu_B = b(B(\vec{r}) - B_m)^2 \quad (2.12)$$

with $b \approx 431$ Hz/G². For atoms trapped in a harmonic potential in the presence of gravity, the Zeeman shift becomes position dependent

$$\Delta\nu_B = \frac{2m^2}{\mu_B^2} \left(\omega_x^2 x^2 + \omega_y^2 y^2 + \omega_z^2 z^2 - 2gz + \delta B \frac{\mu_B}{m} \right)^2 \quad (2.13)$$

with $\delta B \equiv B(\vec{r} = 0) - B_m$ and g the gravitational acceleration. Using the Maxwell-Boltzmann distribution the ensemble averaged Zeeman shift is [104].

$$\overline{\Delta\nu_B} = \frac{b}{\mu_B^2} \left(\frac{4g^2 m k_B T}{\omega_z^2} + 15k_B^2 T^2 + 6\mu_B \delta B k_B T + \delta B^2 \mu_B^2 \right) \quad (2.14)$$

Differentiation with respect to δB leads to the effective magic field

$$\delta B_0^B = \frac{-3k_B T}{\mu_B} \quad (2.15)$$

where the ensemble averaged frequency is independent from magnetic field fluctuations. For $T = 80$ nK, $\delta B_0^B = -3.6$ mG is close to the field of maximum contrast $\delta B_c \approx -35$ mG such that the fringe contrast is still 85% (figure 2-13). If $\delta B \neq \delta B_0^B$ is chosen the clock frequency fluctuations due to magnetic field fluctuations are

$$\sigma_{y,B} = \frac{\partial \overline{\Delta\nu_B}}{\partial B} \times \sigma_B = 2b |\delta B_0^B - \delta B| \sigma_B \quad (2.16)$$

We will use this dependence to measure σ_B .

Temperature fluctuations affect the range of magnetic fields probed by the atoms (2.14) and the atom density, i.e. the collisional shift (2.7). Differentiation of both with respect to temperature also leads to an extremum, where the clock frequency is insensitive to temperature fluctuations. The extremum puts a concurrent condition on the magnetic field with

$$\delta B_0^T = -\frac{15k_B T + \frac{2g^2 m}{\omega_z^2}}{3\mu_B} - \frac{\hbar(a_{11} - a_{22})(e^{\gamma T_R} - 1)\sqrt{m}N_f\mu_B\omega_x\omega_y\omega_z}{16\pi^{3/2}b(k_B T)^{5/2}\gamma T_R} \quad (2.17)$$

For our conditions, $\delta B_0^B = -3.6$ mG and $\delta B_0^T = -79$ mG are not identical but close and centered around δB_c . We will see in the following that a compromise can be found where the combined effect of magnetic field and temperature fluctuations is minimised. If $\delta B \neq \delta B_0^T$ is chosen, the clock frequency fluctuations due to temperature fluctuations are

$$\sigma_{y,T} = \frac{6bk_B}{\mu_B} |\delta B_0^T - \delta B| \sigma_T \quad (2.18)$$

thus varying δB allows to measure σ_T , too.

We determine σ_B and σ_T experimentally by repeating several stability measurements for different δB over a range of 200 mG around B_m where the contrast is above 60% allowing good stability measurements (fig 2-13). The stability at one shot is shown in figure 2-14. One identifies a clear minimum of the (in)stability at $\delta B \approx -40$ mG, which is a compromise between the two optimal points δB_0^T and δB_0^B . This means, that both magnetic field and temperature fluctuations are present with roughly equal weight. We model the data with a quadratic sum of all so far discussed noise sources. Those independent from δB give a constant offset. $\sigma_{y,B}$ and $\sigma_{y,T}$ are fitted by adjusting σ_B and σ_T . We find relative temperature fluctuations of $\sigma_T = 0.55\%$ at 1 shot and magnetic field fluctuations at 1 shot of $\sigma_B = 18\mu G$ or 6×10^{-6} relative to 3.2 G. Both noise sources being of technical origin, the results demonstrate our exceptional control of the experimental apparatus. The relative mag-

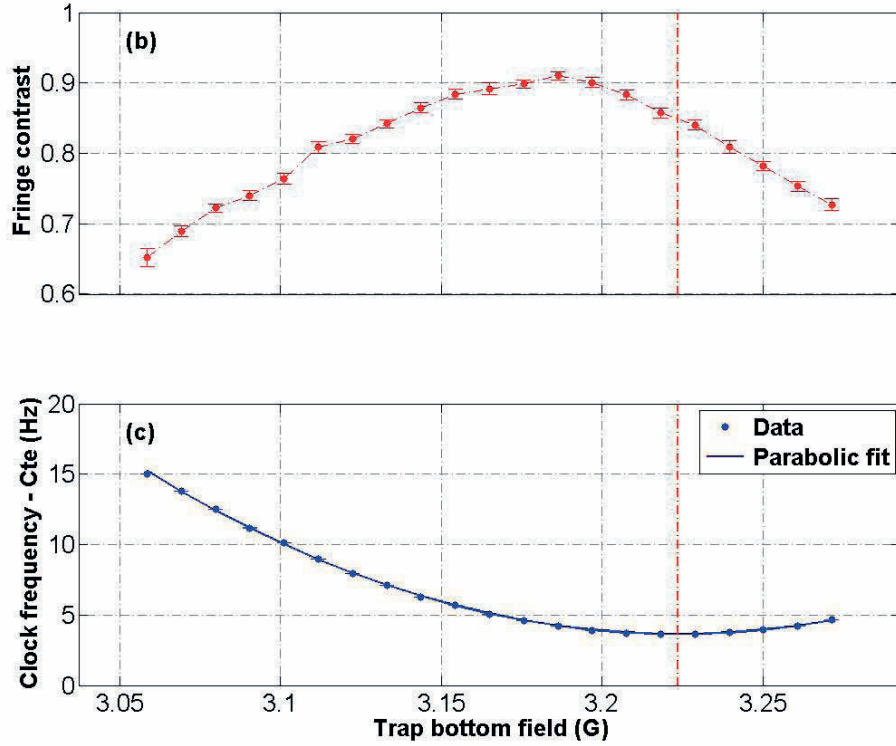


Figure 2-13: Fringe contrast and clock frequency for various bias fields. Red dashed line indicates the magic field as found by the minimum clock frequency, the maximum of contrast is offset -35 mG from the magic field.

netic field stability is compatible with the measured relative current stability of our current supplies [101]. The atom temperature fluctuations appear small compared to standard experiments where evaporative cooling is used. This may again be due to the exceptional magnetic field stability; the atom temperature is determined by the magnetic field at the trap bottom during evaporative cooling and the subsequent opening of the magnetic trap. At all stages, the current control is the most crucial.

Using equations 2.16 and 2.18 the magnetic field and temperature fluctuations translate into a frequency noise of $\sigma_{y,B} = 2.6 \times 10^{-13} \tau^{-1/2}$ and $\sigma_{y,T} = 3.8 \times 10^{-13} \tau^{-1/2}$, respectively, for the conditions of figure 2-4. The comparison in table 2.1 shows, that these two are the main sources of frequency instability. Our current supplies may be improved, e.g. by locking to low noise current transducers which can have a relative stability better than 10^{-6} . If the magnetic field fluctuations can be reduced,

the temperature fluctuations may also reduce. Even if the two are uncorrelated, small σ_B would allow to operate nearer to the sweet spot δB_0^T where temperature fluctuations have a smaller effect. We can thus expect to reduce their contribution to $\sigma_{y,B+T} \approx 10^{-13} T^{-1/2}$.

Impossibility to correct temperature from images As we image the atom cloud at each shot, we could in principle extract the atom temperature from the cloud width after time-of-flight. This analysis gives shot-to-shot fluctuations of $\sigma_T/T = 2 - 4\%$, which is much bigger than the 0.55% deduced previously. We therefore conclude that the determination of the cloud width is overshadowed by a significant statistical error. Increasing the time-of-flight, which would reduce this error, would increase the detection noise which is dominated by the number of pixels onto which the cloud is imaged.

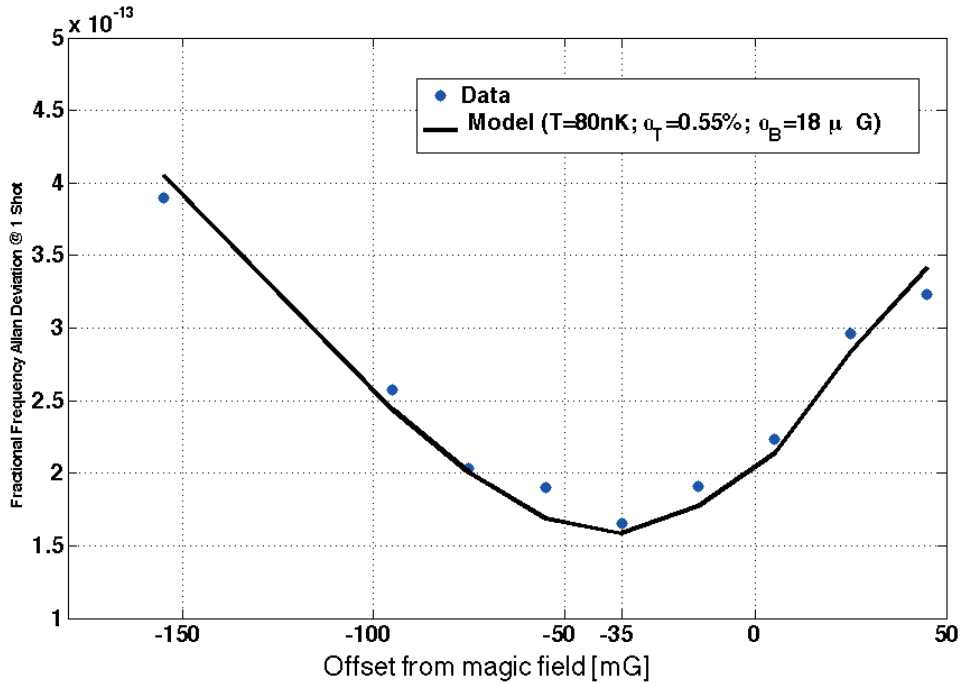


Figure 2-14: Clock stability at 1 shot for various magnetic fields at the trap bottom offset from the magic field 3.23 G. One observes a clear optimum of the clock stability at -35 mG. Fitting with the model described in the text allows to identify the temperature and magnetic field fluctuations.

2.5 Conclusion

We have build and characterised a compact atomic clock using magnetically trapped atoms on an atom chip. The clock stability reaches 5.8×10^{-13} at 1 s and integrates to 6×10^{-15} in less than 10 hours. This outperforms commercial clocks by almost one order of magnitude and is competitive with the best compact atomic clocks under development.

After correction for atom number fluctuations, variations of the atom temperature and magnetic field are the dominant causes of the clock instability followed by the local oscillator noise. The magnetic field stability may be improved by additional current sensing and feedback. This would allow to operate nearer to the second sweet spot where the clock frequency is independent from temperature fluctuations. The local oscillator noise takes an important role, because the clock duty cycle is $< 30\%$. We are now in the process of designing a second version of this clock, incorporating fast atom loading and non-destructive atom detection. We thereby expect to reduce all technical noises below the quantum projection noise and to reach a short term stability near $10^{-13}\tau^{-1/2}$.

Chapter 3

Towards an atom chip atom interferometer

3.1 Review of atom interferometers

Atomic interferometers use the interference of matter waves in order to make precise measurements of phase. In an atom interferometer, a matter wave source is coherently split into two paths which later recombine to produce an interference pattern. The phase difference deduced from such a pattern is a measure of the path length difference, resulting in the measurement of distances, rotations or accelerations with a precision often equivalent or better than optical devices [33, 54]. Atom interferometers can also be coupled to a larger variety of forces the measurement of which is hardly attainable with laser sources. Gravity in particular, can be precisely measured using atom interferometers as we will later discuss in detail, something which cannot be done with light waves.

The observation of interference fringes from atoms had to wait until the early 90's when a Young double slit experiment was performed with metastable Helium atoms diffracting from two slits in a gold foil [21]. The challenge of building interferometers with atoms lies in the difficulty of creating coherent beam splitters and mirrors for the atomic de-Broglie waves. Neutral atoms do not carry an electric charge and so cannot be manipulated with electric fields. They also cannot be easily diffracted from

gratings like neutron. Thus the road to atom interferometers has been paved by the development of coherent atom-optics elements.

3.1.1 A basic framework for comparing the sensitivity of atom interferometers

Although atom interferometers vary greatly in the schemes they employ for the separation and recombination of wavepackets, what is common to all is that their sensitivity is governed by the differential phase accumulated by the two paths. In order to be able to compare different kinds of interferometers, we will derive a figure of merit for a general interferometer. We consider the situation immediately after the splitting process, so that the external fields are constant in time and the wavepacket is assumed to be isolated. In such a system the time evolution operator of the quantum mechanical wavefunction $|\psi(t)\rangle$ can be written as:

$$U(t) = e^{-\frac{i}{\hbar}Ht} \quad (3.1)$$

Inducing the evolution:

$$|\psi(t)\rangle = U(t)|\psi(0)\rangle \quad (3.2)$$

Where H is the Hamiltonian of the system, or the "generator" of the time evolution. The phase accumulated by the state $|\psi(t)\rangle_i$ is then simply $\phi_i = \frac{1}{\hbar}H_i t$ and the relative phase accumulated between two wavefunctions at two different points in space x_1 and x_2 during a period dt is:

$$d\phi(x_1, x_2) = \frac{dt}{\hbar}(H(x_1) - H(x_2)) \quad (3.3)$$

In order to compare the sensitivity of various interferometers, we assume the Hamiltonian to contain only a linear spatial gradient, $H = H_0 + \alpha x$, which is not common to both wavefunctions and write:

$$d\phi = \frac{\Delta x dt}{\hbar} \times \alpha \quad (3.4)$$

Since interferometers have in general a spatial separation that evolves with time, the total accumulated phase during an interferometric sequence of length T is:

$$\Delta\phi = \int_0^T \frac{\alpha}{\hbar} \Delta x(t) dt = \frac{\alpha}{\hbar} \chi \quad (3.5)$$

Following a suggestion by Burke et al. [20] we have defined the figure of merit $\chi = \int_0^T \Delta x(t) dt = \hbar \frac{\Delta\phi}{\alpha}$ which characterizes the sensitivity of a general interferometer to a spatial gradient α . For many interferometers additional pulses are applied during the sequence [71, 124] but since they are all phase coherent we can treat the propagation in a piecewise manner.

Atom interferometers can either use atoms in free fall or in a trapped configuration. In the free-fall configuration, the atoms are launched or released in a long vacuum chamber and allowed to free-fall. Using laser pulses, a differential momentum is coherently imparted on the two states causing a gradual separation in space. After an evolution time T , an opposing momentum kick is applied reversing the direction of separation and causing the wavepackets to recombine after a time $2T$ thus closing the interferometer. In trapped atom interferometers, the wavefunctions are held in a harmonic confining potential which is then deformed to form a double well with a certain splitting distance between the two minima. The wavefunctions are then allowed to accumulate a phase during a period T after which the barrier is lowered and the wavefunctions recombine to close the interferometer. As we will later see, some interferometers place different paths in different internal states [71] thus resulting in an H_0 which is path dependent. However, this kind of internal state labelling is done such that both paths spend the same amount of time in each internal state, thus cancelling this contribution. Finally, at first sight this picture does not apply to free falling atoms as in an inertial frame they don't experience any gradients. Nevertheless [122] treats the gravitational gradient as a perturbation and integrates its contribution along the unperturbed paths. This treatment shows that the relative phase shift actually originates from the phase imprinted by the laser light on the atoms as a result of the three light pulses and in the end yields the same expression

of equation 3.5. We will now review in more detail the various interferometer schemes and compare their characteristics, where the performances will be compared on the basis of the figure of merit χ .

3.1.2 Free fall atom interferometers

Following a suggestion by Bordé [16], Kasevich and Chu [71] created an interferometer which incorporated internal state labeling and a Ramsey type scheme with an echo pulse in order to measure gravity. In this scheme, known as Ramsey-Bordé interferometry, Kasevich and Chu used counterpropagating Raman beams in order to impart momentum and spatially split the two paths. Besides imparting momentum the Raman pulse is also a $\pi/2$ pulse for the internal states, thus transferring an atom initially prepared in the $|F, k \rangle = |1, 0 \rangle$ state into the superposition state $|1, 0 \rangle \rightarrow 1/\sqrt{2}(|1, 0 \rangle + |2, 2\hbar k \rangle)$ where k is the wavevector of one of the Raman beams. After a time of flight T a π pulse is applied, acting as a mirror to reflect the two paths back towards each other. As they recombine another $\pi/2$ pulse is applied in order to close the interferometer (see Figure 3-1).

If the two paths have at the end of the interferometer sequence a zero relative phase the second $\pi/2$ pulse will simply complete the first and transfer all atoms to the $|2 \rangle$ state, if the atoms are π out of phase, all atoms will be transferred to the $|1 \rangle$ state. Thus the relative phase between the two paths is imprinted on the population imbalance between the two states and can be read out by counting the number of atoms in each state just like in an atomic clock. The phase difference between the two paths in such a scheme is insensitive to the initial atom velocity and scales as $\Delta\phi = 2k\alpha T^2$. In order to extend the integration time, atoms can be launched upwards in a fountain trajectory, reaching the maximum splitting distance at the apex. This scaling can also be interpreted in the following way, the relative distance of the two paths is given by $\Delta z(t) = \frac{2\hbar k}{M} * t$ where $\frac{2\hbar k}{M}$ is the relative velocity separating the two clouds and t the separation time. Immediately following the first splitting pulse the paths separate for a time T resulting in an integrated splitting distance of $\chi_T = \int_0^T \Delta z(t) dt = \frac{\hbar k}{M} T^2$. After the mirror pulse the paths follow a

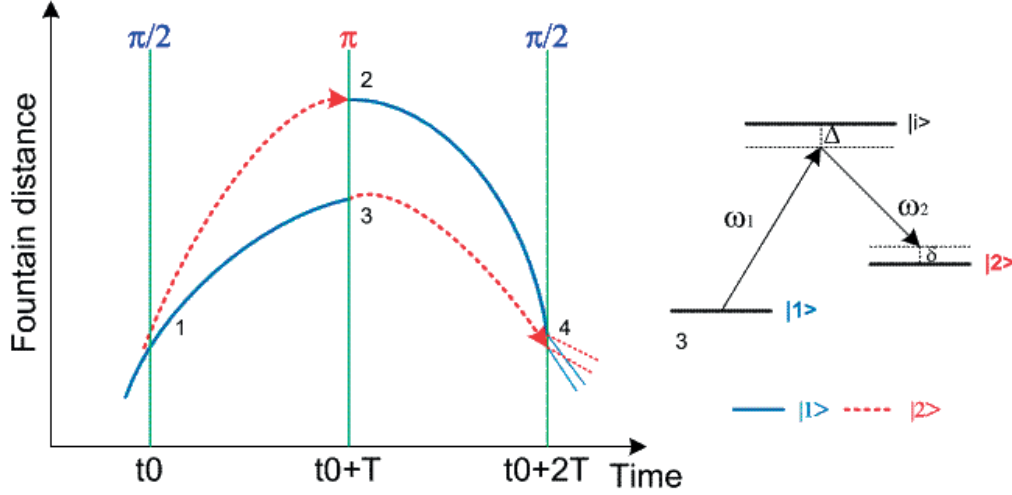


Figure 3-1: Operation of a free-fall atom interferometer. At t_0 a cloud of ultracold atoms is prepared and a $\pi/2$ pulse is applied inducing the transition: $|1, 0 \rangle \rightarrow 1/\sqrt{2}(|1, 0 \rangle + |2, 2\hbar k \rangle)$ and imparting momentum to half of the wavefunction. At $t_0 + T$ a second pulse acts as a mirror causing the paths to converge. At $t_0 + 2T$ the final $\pi/2$ pulse is applied and the different paths interfere. The pulses are performed via Raman transitions. Figure taken from [78].

symmetric trajectory yielding a figure of merit twice as big: $\chi_{2T} = 2\chi_T = \frac{2\hbar k}{M}T^2$ from which we get the original expression for the phase shift. The expression for the sensitivity of free falling interferometers makes it clear that in order to increase the sensitivity one can either increase the size of the interferometer (thereby allowing for a longer interrogation time) or increase the number of momentum kicks imparted on the wavepacket [25, 85].

The most sensitive free fall gravimeter using Raman beams was demonstrated in Kasevich's group by Dickerson et al. [39] where by using a 10 meter vacuum chamber they were capable of extending the interferometer time to $2T = 2.3$ s and split the wavepacket by 1.4 cm. They used Rubidium atoms where $k = 2\pi/780$ nm yielding a figure of merit of $\chi = 15.6$ mm · s. The associated phase shift is thus $\Delta\phi = 2.1 \times 10^8$ rad. Their system exhibits a phase noise of 1.4 mrad thus demonstrating a sensitivity to acceleration of $\delta\phi/\Delta\phi = 6.7 \times 10^{-12}$ g in one shot. Today this represents the most sensitive atom interferometer ever built.

Another possibility is to increase the amount of momentum difference between

the two interferometer paths. Giltner et al. [57] used Bragg diffraction (without state labeling) from a standing wave optical lattice in order to impart several $\hbar k$ of momentum difference (up to $6\hbar k$). The standing wave lattice acts as a thick grating on which the atomic wavepacket scatters. The diffraction criterion requires that an atom absorbs n photons from one beam and reemits them into the other one, thereby absorbing the momentum of $2n$ photons. The recoil energy difference has to be compensated by the relative detuning of the two laser beams $\Delta f = (k)^2/m\pi$ so that tuning the relative frequency selects the order of the Bragg diffraction. By setting the length of the pulse one can tune the transfer probability, thereby creating a 50/50 beamsplitter. By increasing the lattice power and improving on the wavefront quality Muller et al. [85] managed to diffract an atomic beam of cesium to the 12th order, thereby imparting $24 \hbar k$ photon momenta. The visibility of the fringes disappeared after about $T = 100$ ms, leading to a figure of merit of $\chi = 0.85 \text{ mm} \cdot \text{s}$ and an accumulated phase difference of about $\Delta\phi = 24kgT^2 \approx 1.7 \times 10^7$ rad. In a subsequent experiment, by using a sequence of Bragg diffractions, Chiow et al. [25] demonstrated the largest momentum splitting to date, with $102\hbar k$ photon momenta separation. However, due to noise from wave front distortion and population loss the integration time was on the order of only 10 ms, resulting in an accumulated phase of only $\Delta\phi \approx 8 \times 10^5$ rad. The contrast in such Bragg diffraction experiments is usually greatly reduced due to inefficiencies of the Bragg splitting, aberrations in the wavefront and the thermal motion of the atoms which results in the smearing of the phase over the atomic ensemble. Additionally, phase noise is high due to vibrations of the laboratory frame in which the phase is stabilized.

A multitude of schemes exist nowadays which use free fall atom interferometry for the most precise metrological measurements. Compared to the large 10 m free fall interferometer, smaller setups exist which allow for gravity surveys in remote places [49] while still maintaining a 10^{-9} g sensitivity after 100 seconds of integration time. This performance is comparable to the best falling cube gravimeter [86] but does not suffer from the high wear and slow integration rate (which is required to reduce vibrations) of such devices. The use of a dual cloud atom interferometer allows

the measurement of gravity gradients [83, 117]. Measurements of the gravitational constant with an atomic interferometer [51, 105] produce the best known value of G to date with a standard error on the 10^{-4} level, an impressive achievement considering the weakness of the interaction ($G \approx 6.7 \times 10^{-11} \text{ N} \cdot (\text{m}/\text{kg})^2$). Other inertial forces are measured with impressive sensitivity. Gyrometers exploit the Sagnac effect which accumulates a phase due to the area enclosed between the arms of the interferometer [43, 56]. The state of the art today being on the $10^{-10} \text{ rad} \cdot \text{s}^{-1} \cdot \text{Hz}^{-1/2}$ level [60]. Compact 3-axis gyroscope units [121] were also constructed with a sensitivity of $8.5 \times 10^{-8} \text{ rad} \cdot \text{s}^{-1} \cdot \text{Hz}^{-1/2}$ and a volume of less than 125 liters. Purely scientific applications are plentiful, from the testing of general relativity [40] and gravitational wave detection [58] to the determination of the fine structure constant [17].

3.1.3 Confined atom interferometers

As previously discussed, the sensitivity of free fall interferometers is limited by the apparatus size. In order to obtain large phase shifts while maintaining a compact system, wave packets can be confined by trapping potentials in order to overcome gravity. With the advent of laser cooling, optical molasses and evaporative cooling techniques, atoms can now be trapped and prepared in their momentum ground state reaching Bose-Einstein condensation, thus creating a source with a very narrow momentum distribution.

A distinction is made between trapped and guided interferometers. In trapped atom interferometers the wavepacket is confined in all three directions by an harmonic trap and the beam splitter is implemented by deforming the trapping potential into a double well configuration. The wavepacket is split in space, held for a period of time and then recombined in order to measure the relative phase accumulated in the two wells. In guided atom interferometers the wavepacket is confined in only two directions while allowing it to propagate along the waveguide. The beam splitter is implemented by either bifurcating the waveguide into two adjacent guides [36] or by splitting the wavepacket by laser pulses collinear with the waveguide axis [129], similar to the methods developed for free falling interferometers.

Guided atom interferometers

Early attempts with guided atom interferometers focused on splitting BECs using Y-shaped wire waveguides fabricated on atom chips [22, 23, 36], but were only able to physically split a cloud of thermal atoms without observing interference fringes. The more common method today is to use a combination of magnetic trapping and light induced beam splitters: Wang et al. demonstrated a Michelson interferometer (symmetrical splitting) on an atom chip [129] by trapping a BEC in a magnetic waveguide and then splitting it with a pulse of a standing wave optical lattice aligned parallel to the magnetic waveguide axis. The pulse couples atoms into the $|p = \pm 2\hbar k\rangle$ states (Raman-Nath regime) splitting the clouds in opposing directions. After some propagation time a Bragg pulse is applied in order to reverse the direction of propagation. The interferometer is then closed with a recombination pulse when the clouds overlap. With such a method Wang et al. managed to split the condensate by $120\mu\text{m}$ but could obtain a contrast of only 20% after 10 ms. They attributed the loss of contrast to inhomogeneities of the trapping potential and interaction processes. Horikoshi et al. [66] performed a similar scheme but in a Mach-Zehnder configuration (asymmetrical splitting) using Bragg pulses to impart $2\hbar k$ momenta to half of the condensate but were able to preserve coherence for only a few ms. One way to compensate for asymmetries is to use "free oscillating" interferometers [65, 68]. In such a scheme the atoms are held in a three dimensional trap having one shallow axis and the atoms are split with a standing wave pulse, the trap curvature then guides the atoms back towards each other instead of applying a mirror pulse. The interferometer is closed with the final pulse after each cloud has performed a full oscillation. This scheme greatly increases the coherence time. Burke et al. [20] have demonstrated arm separations of 1.7 mm and an integration time of 0.9 s with $\approx 30\%$ contrast. Horikoshi et al. [65] also observed increased coherence times using this method and demonstrated that the phase becomes stable by increasing the longitudinal trapping frequency ω , indicating that the fluctuations are due to low-frequency external noise, such as mechanical vibrations of the experiment. However, it must be noted that such

a freely oscillating "double-8" scheme cannot be used to measure potential gradients, since both paths of the interferometer probe the same regions of space. In a ring shaped trap such a method would be sensitive to rotations via the Sagnac effect and could be exploited to build an atomic gyroscope [55].

We take these experiments as a proof of concept for the capabilities of trapped atom interferometers. Assuming the randomness of the phase can be controlled by better vibration stabilization systems, a separation of 1.7mm and an integration time of 0.9 s in such a configuration gives a figure of merit of $\chi = 1.6 \text{ mm} \cdot \text{s}$, which is only an order of magnitude less than the large free fall interferometer used by Kasevich but in a much smaller setup. This point is encouraging and stimulates further research on trapped atom interferometers.

Trapped atom interferometers

We now turn our attention to trapped atom interferometers, where the wavepacket is coherently split by modifying the trapping potential. In free and guided atom interferometry, atoms are separated by imparting momentum quanta on the atoms, which after a time evolution translate into a spatial separation. This allows very precise and stable splitting since the transferred momentum is fixed. In trapped atom interferometers, the coherent separation is done directly in position space by deforming the shape of the trapping potential. This depends on macroscopic field sources which cannot be controlled on the individual quanta level. Additionally, the splitting process must be adiabatic so as not to induce excitations of the trapped wavepacket, thus the interaction times are longer and the mechanism more susceptible to inhomogeneities which cause decoherence. Meeting these challenges is however worthwhile, since as we previously saw trapped atom configurations can lead to very high sensitivities with compact setups due to the long interrogation times and large splitting distances.

Double well potentials were initially attempted by using multiple wire configurations on an atom chip [47, 52]. They initially demonstrated interference fringes [115] but with a random phase, indicating that the splitting process did not preserve a

common phase between the two condensates. In 2005, the first phase coherent double well potential was demonstrated by Schumm et al. [112] which used adiabatic RF dressed state potentials [31, 64, 79, 137] in order to deform the shape of a magnetic trap on an atom chip. The RF field originating from one of the chip wires coupled the various Zeeman sublevels of the magnetically trapped atoms. The coupling mixes the magnetic moment of the trapped atoms (low field seekers) with that of untrapped states having opposite magnetic dipole moments (high field seekers) for which the trapping potential minimum is instead a potential hill. This coupling resulted in an effective potential given by the superposition of the trapped and anti-trapped potentials experienced by the different Zeeman sub levels. In such a way, a potential maximum originating from the mixing in of the anti-trapped states is "grown" in the center of the harmonic potential and transforms the trap into a double well. The first attempt by Schumm et al. displayed modest performances, with a maximum splitting distance of less than $5\mu\text{m}$ and a coherence time on the order of 2ms, resulting in a figure of merit of approximately $\chi \approx 10^{-5} \text{ mm} \cdot \text{s}$.

An issue with RF dressed state interferometry is the estimation of the spatial shape of the dressing field. Baumgartner et al. [11] demonstrated a measurement with a 10% error bar using an RF induced double well potential, far from current state of the art free falling interferometers. They estimate that they could reduce the error of such a device to the 1% level but that beyond that the spatial inhomogeneity of the RF field strength will introduce systematic errors since the trap bottom in the two different positions will have an offset which will cause the accuracy of the gravity estimate to be limited by the estimation of the RF field distribution. On the positive side, trapped atom interferometers are ideal for probing short range potentials and are capable of scanning fields with a spatial resolution on the μm scale, something which is unattainable with free fall interferometers. Ockeloen et al. [88] recently demonstrated a measurement of near field magnetic fields on an atom chip and shows promise in that direction.

Finally, dressed state potentials can be also generated with microwave fields where instead of coupling different Zeeman sublevels, the microwave dressing couples dif-

ferent hyperfine states and can thus generate state dependent potentials. Microwave dressed state potentials have been demonstrated more than 20 years ago [6, 119] by using atoms in the far field of a microwave source. However, due to the relatively large wavelength (4.4 cm for Rubidium), the far field gradients are very weak. In [119] for example, 0.5MW of power was circulated in a cavity without even being able to hold the atoms against gravity. In contrast, atom chips allow atoms to be trapped in the near field of wires ($d \ll \lambda_{MW}$) which can be fabricated on the chip in the form of a transmission line. Such near field potentials exhibit much larger gradients. In our system for example, we trap atoms about $50\mu\text{m}$ above the surface of a coplanar waveguide so that even by dressing the atoms with a large detuning of 0.5MHz we can still create gradients comparable to that of gravity with a power of only 25mW. For a dressing with a detuning of 0.5 MHz from the $|1, -1\rangle \rightarrow |2, -1\rangle$ transition for example, it allows us to displace the $|1, -1\rangle$ state along z by $11.7\mu\text{m}$ without forming a double well. It thus becomes interesting to explore the possibility of using the near field interaction of a CPW in order to create a beam splitter for atoms.

Bohi et al. [15] used microwave dressed ^{87}Rb atoms and demonstrated an interferometer with a splitting distance of $4.3\mu\text{m}$ and could resolve fringes with a controlled phase after 8.5 ms and after 17 ms with a random phase, resulting in a figure of merit on the order of $\chi \approx 7 \times 10^{-5} \text{ mm} \cdot \text{s}$. The work of Bohi et al. did not use a double well configuration, instead they state selectively shifted one of the two clock states of ^{87}Rb within a Ramsey sequence, measuring the relative phase shift of the two states. In the next sections, we propose a scheme using microwave dressed state double well potential, a first of its kind in atom interferometry.

Possible sensitivities of trapped atom interferometers

We will now extrapolate possible sensitivities of trapped atom interferometers based on the performances of previous experiments. Given that coherence times of trapped atoms on the order of one minute have been demonstrated [19, 38] (although not in an interferometric scheme) and that separation distances of 1.7mm [20] were already shown, we can envisage a possible trapped atom interferometer with a figure of merit

on the order of $\chi \approx 10 \text{ mm}\cdot\text{s}$ which is on the same order of magnitude as the large free fall interferometer demonstrated by the Kasevich group (with $\chi = 15.6 \text{ mm}\cdot\text{s}$). Thus it seems in principle possible to reach sensitivities comparable and even superior to large scale interferometers with compact trapped atom setups. Turning more modest, if we consider a coherence time of 1 second and a splitting distance of $\approx 100 \mu\text{m}$ we can still reach a figure of merit on the order of $\chi \approx 0.1 \text{ mm}\cdot\text{s}$, allowing a sensitivity of 10^{-9} g by assuming a phase noise of 1 mrad on the detection system. Said differently, this represents a precision of $\approx 0.7 \mu\text{Gal}$ at one shot. Assuming a sequence 10 seconds long and a system integrating as white noise this corresponds to a sensitivity of $\approx 2\mu\text{Gal}\sqrt{\text{Hz}}$ which is an order of magnitude better than state of the art absolute gravimeters using a falling corner cube architecture [86] and which display a sensitivity of $\approx 15\mu\text{Gal}\sqrt{\text{Hz}}$.

3.1.4 Microwave dressed potentials and our proposed interferometer scheme

One major problem of current trapped atom interferometers is related to the dynamical deformation of the trapping potential. As the barrier is increased, the energy of the first excited state progressively approaches that of the ground state until they eventually become degenerate. Thus, an ideally adiabatic transfer cannot be reached even for long ramping times [115] since at a certain point the transfer will excite higher vibrational states. Populating several vibrational states is detrimental, since each vibrational level has a different energy, and thus a different rate of phase accumulation causing a reduction of contrast. Abruptly changing the trapping potential will on the other hand induce mechanical perturbations of the condensates with dissipation or coupling to internal excitation modes [90] which would also result in an unpredictable relative phase between the two condensates. An alternative option [114] is to prepare two condensates in a double well potential with the barrier lower than the chemical potential thus allowing the two condensates to lock their phase. The barrier can then be raised further in order to fully separate the condensates. Another direction is to

prepare two condensates in different positions and then imprint on them a phase from an external field. Saba et al. [107] demonstrated this principle by scattering light from two condensates prepared at different positions.

In this chapter we present a new scheme for double well interferometry which overcomes these problems by using a new kind of fast and robust beam splitter. We elaborate a proposal by Philipp Treutlein [125] who suggested microwave dressing to create a single and a double well potential depending on the internal state. The idea (see Fig. 3-2) is to create a state selective double well potential in an unpopulated state and then transfer an ensemble of atoms to this split potential with a π pulse. Such a scheme has the distinctive advantage that it does not require the dynamical variation of the trapping potential in order to populate a double-well and is thus expected to greatly reduce the excitation of the condensate.

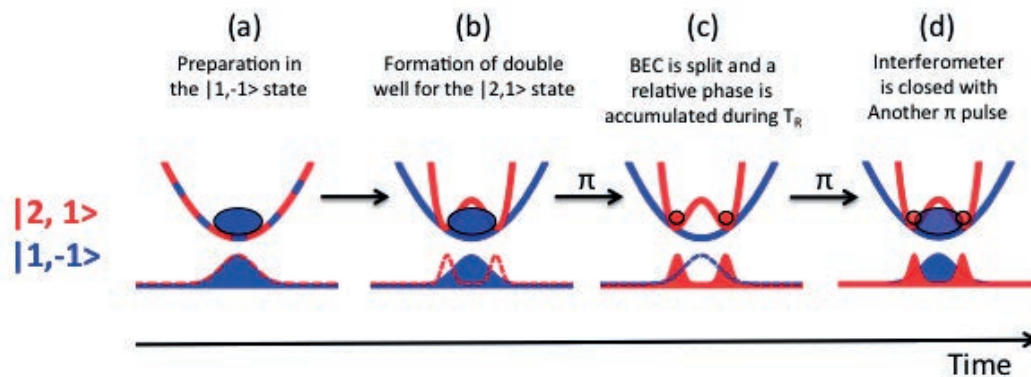


Figure 3-2: Scheme of the proposed interferometer. At first (a), a BEC is prepared in the ground state of the $|1, -1\rangle$ state. Then (b), the trap in the $|2, -1\rangle$ state is dressed to form a double well and a π pulse transfers the atoms from $|1, -1\rangle$ to $|2, 1\rangle$ (c). After a Ramsey time T_R , a second π pulse closes the interferometer sequence and the relative phase between the two wells is read (d) from the relative occupation of the two hyperfine states.

Such a scheme offers several advantages:

1. The issues associated with passing through a quartic potential are eliminated since the generation of the double well is done when the state is unpopulated. The atoms are transferred to an already formed double well without inducing excitations due to the ramping of the barrier.
2. The atoms are split in the same internal state, making the accumulated relative

phase insensitive to level shifts.

3. The relative phase accumulation starts when the π pulse ends. While the transfer pulse is active, the two wells are coupled through the single well state and thus do not develop a relative phase. This means that the phase evolution starts at a well defined moment facilitating the analysis.

4. Our scheme shares the advantages of Ramsey type trapped atom interferometers, namely the possible large interrogation times allowed by the trapping potential and the simplified phase readout in the form of relative atom number counting between the two states.

In order to implement a state dependent double well potential we employ a microwave dressing scheme on the magnetically trapped clock states of ^{87}Rb $|1, -1\rangle$ and $|2, 1\rangle$ (see figure 3-3 and figure 3-4). In such a way we are able to form a double well potential for just the $|2, 1\rangle$ state by coupling the $|2, 1\rangle \rightarrow |1, 1\rangle$ transition with the microwave field originating from the coplanar waveguide (CPW) on our atom chip. The coplanar waveguide is a structure made of three parallel wires fabricated on our atom chip. This structure forms a microwave mode which (as we will later see) allows for a strong coupling with atoms trapped directly above the central wire. Since the atoms are trapped in a magnetic trap with a field at the trap bottom of $B_0 \approx 3G$, the Zeeman splitting creates a detuning of at least 7MHz between the $|2, 1\rangle$ dressing and any transition coupling the $|1, -1\rangle$ state with the $|2\rangle$ manifold, thus this state is virtually unmodified and remains trapped in the initial harmonic trap.

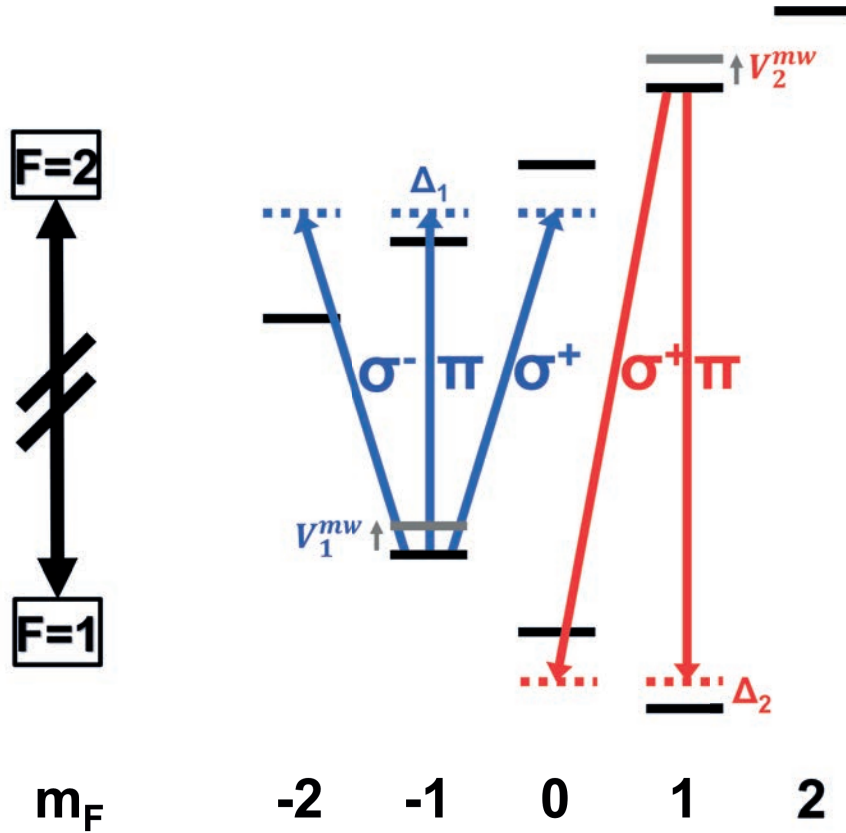


Figure 3-3: Level scheme for the proposed interferometer. We dress the $|1, -1\rangle$ state with a π transition coupling it to the $|2, -1\rangle$ state with a blue detuning of Δ_1 . The $|2, 1\rangle$ state is also dressed via a π transition to the $|1, 1\rangle$ state with a detuning Δ_2 . Even though the dressing detuning are closer to resonance with the π transition, other σ polarizations couple as well. The dressing is seen to be asymmetric as the $|1, -1\rangle$ state has an additional σ^- transition coupling it to $|2, -2\rangle$ for which there is no counterpart for the $|2, 1\rangle$ state. We will later see how this asymmetry is beneficial in creating a double well potential for the $|2, 1\rangle$ state while keeping the $|1, -1\rangle$ state in a single well potential and at the same vertical position. This ensures a good wavefunction overlap and allows the transfer of atoms between the two states.

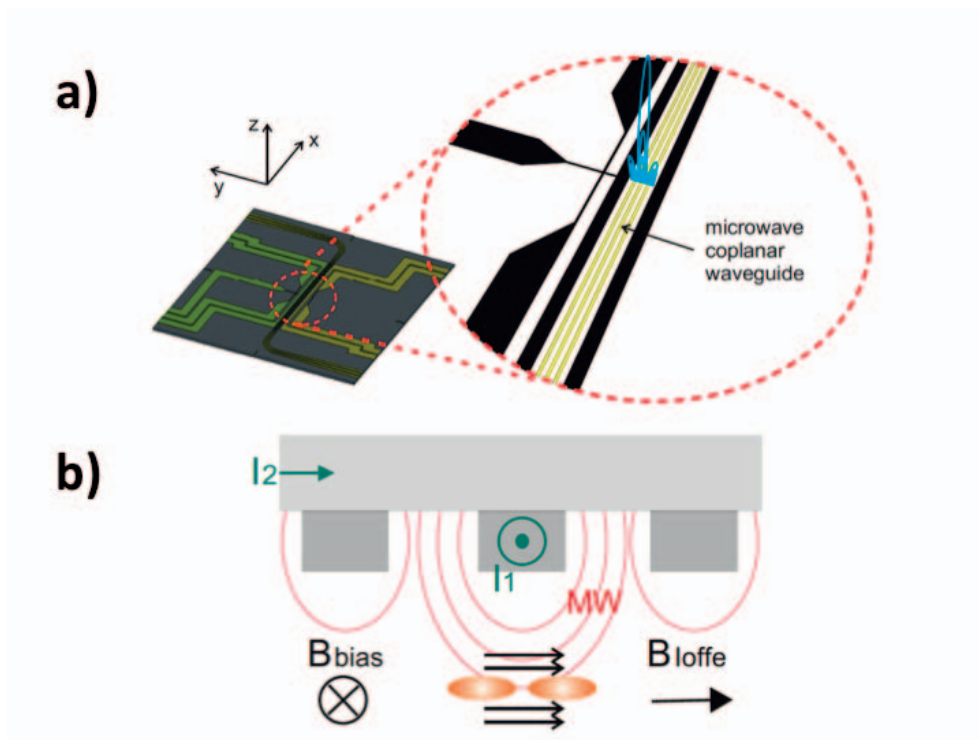


Figure 3-4: Schematics of the chip first layer (a) and the microwave and static fields employed for the formation of a double well potential (b). A zoom at the center of the chip shows the three wires which form the microwave coplanar waveguide. The central wire of the CPW is used, in addition, to carry the stationary current for the generation of the magnetic trap. In (b) we show the schematics of the two layer chip with the main fields for the realization of the microwave dressed double well potentials. The currents I_1 and I_2 flow in dedicated wires in the first and second layer of the chip respectively and contribute together with the Ioffe magnetic field B_{Ioffe} and bias field B_{bias} to the formation of the static magnetic trap where the atoms are kept. Due to the action of the microwave a double well is created along the longitudinal axis of the trap (y-axis) for the two states $|1, -1\rangle$ and $|2, 1\rangle$ when the microwave frequency is tuned close to the π -polarization driven transition as shown in figure 3-3.

3.2 Theory

3.2.1 General considerations

The double well potential exploits the spatial dependence of the Rabi frequency, which can be written as:

$$\begin{aligned}\Omega_0 &= \sqrt{\frac{3}{16} \frac{\mu_B}{\hbar} |B_{MW}| \vec{e}_{MW} \cdot \vec{e}_{trap}} \\ \Omega_\pi &= \sqrt{\Omega_0^2 + \Delta^2}\end{aligned}\tag{3.6}$$

Where Ω_0 and Ω_π are the bare and generalized Rabi frequencies, $|B_{MW}|$ is the microwave field amplitude, \vec{e}_{MW} , \vec{e}_{trap} the unit vectors of the microwave and static trap respectively and Δ the detuning. The Rabi frequency has a spatial dependence originating from 3 terms:

1. The detuning is position dependent due to the Zeeman effect induced by the trap $\Delta = \Delta_0 + \frac{\mu_B}{\hbar} (|B_s(\vec{r})| - B_0)$. B_s is the trap field, B_0 the field at the trap center.
2. The microwave polarization depends on the projection of the microwave on the static field ($\vec{e}_{MW} \cdot \vec{e}_{trap}$) and thus depends on the variation of the direction of the trap and microwave fields.
3. The microwave field amplitude $|B_{MW}|$ has a spatial variation given by the field distribution of the CPW.

The first effect has the smallest contribution since the detuning at the center of the trap Δ_0 is in our case set to be much larger than the trap frequencies which are on the order of a few kHz at most. Bringing the dressing closer to resonance will cause Landau-Zener transitions to other states [128] which in our case are untrapped and will thus lead to losses. We observe in our system losses at a detuning smaller than 30 kHz where at a 10 kHz detuning we loose all atoms.

The second option is the dominant one for our configuration and is also the basis of the first RF dressed double well experiment by Schumm et al. [112]. The coupling of the microwave field to the atoms depends on the relative orientation of the two fields.

In the case of π polarization, it is the component of the microwave field parallel to the static magnetic field in the trap ($\Omega_\pi \propto |\vec{B}_{MW} \cdot \vec{B}_s|$) while in the case of σ transitions it is the perpendicular component ($\Omega_\sigma \propto |\vec{B}_{MW} \times \vec{B}_s|$). There are then two extreme variants of this method, either the microwave field is quasi-constant and the trap field rotates with position (such as in [112]) or the static field is quasi-constant and the dressing field orientation rotates which is the case for our configuration.

The third effect, the variation of the microwave amplitude, has a smaller contribution than that of the field orientation for microwave sources originating from straight wires. To realize why, we look at a plot of the absolute field equipotential lines next to those of only the y and z components (see Fig. 3-5) for a single straight current carrying wire. In the case where the quantization axis in the trap is oriented mainly along the y axis (such as in our case), the y and z components are the ones contributing to the π and σ polarizations respectively. It is easily visible that for fields generated by wires the gradients and curvatures of the individual components are stronger than those of the total field amplitude. This arguments can fail when adding several wires as in the case of our CPW, but for static traps positioned directly above the central CPW wire, and for deformations of the trap smaller than the CPW wires separation, the gradients and curvatures are mainly due to the central wire and our graphical explanation survives.

3.2.2 Transfer between a single and a double well

An additional issue concerns the transfer pulse. The requirement for a coherent transfer between the ground state of the single well trap in the $|1, -1\rangle$ state and the double well potential in the $|2, 1\rangle$ state sets some bounds for the Rabi frequency of the transfer pulse $\Omega_{transfer}$. In order to be able to transfer to the ground states of the double well, the transfer pulse needs to be able to spectrally resolve the energy levels of the double well potential, thus setting an upper limit for the Rabi frequency, requiring $\Omega_{transfer} < \omega_{ho}$ where ω_{ho} is the trap frequency at the bottom of the double well potential. On the other hand, for our state $|2, 1\rangle$ the lifetime is limited by losses due to spin exchange collisions where the process $|2, 1\rangle + |2, 1\rangle \rightarrow |2, 0\rangle + |2, 2\rangle$

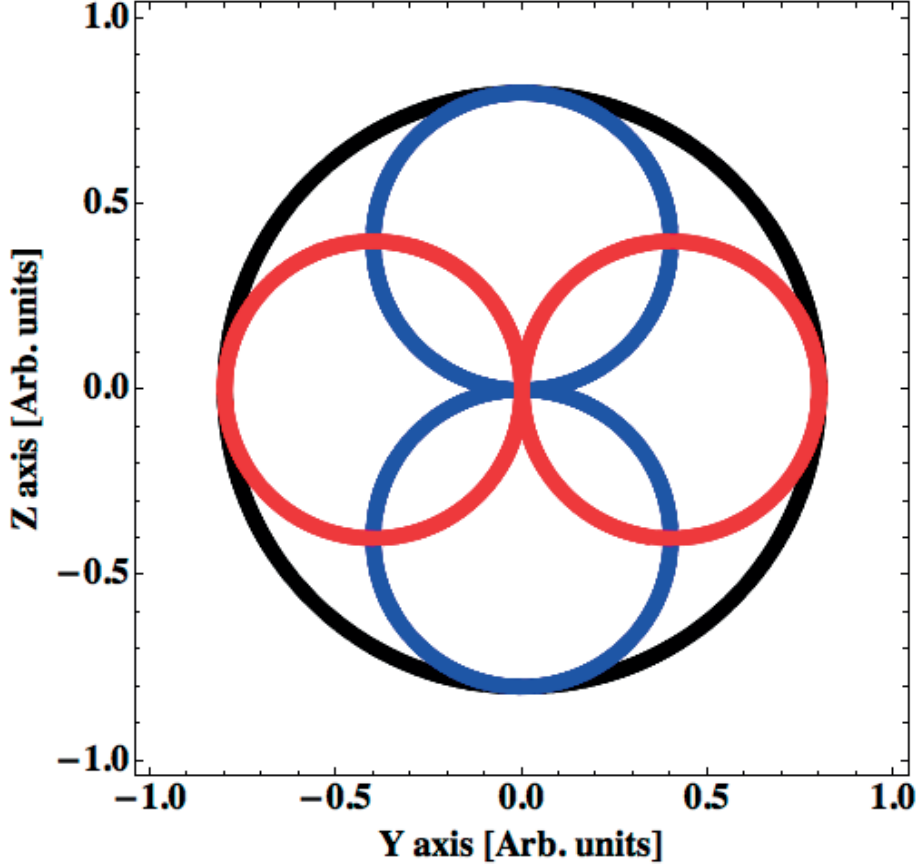


Figure 3-5: Equipotential lines of the total field $|B_{MW}|$ (black), B_y (Blue) and B_z (Red) above a straight wire collinear with the x axis and passing through $(y,z)=(0,0)$. The curvatures of the y and z components are seen to be stronger indicating that inhomogeneities of the polarization play a greater role than those of the amplitude when wires are used as sources for the dressing field.

occurs and atoms end up in either an untrapped state or one where they experience a different static and dressed potential, in either case removing their contribution from the signal. The lifetime depends on the density of the cloud and although we work with relatively shallow traps where $(\omega_x, \omega_y, \omega_z) \approx 2\pi(150, 90, 120)\text{Hz}$ the lifetime is still on the order of only 300 ms. We thus require a pulse length on the order of 100ms so that following the first transfer pulse, the Ramsey time and the final recombination pulse the signal will not be severely attenuated. As the dressing increases, the trap frequency along the y axis will reduce and eventually reach 20-40 Hz. This means that $(2 - 4) \times \Omega_{transfer} \approx \omega_y$ which is at the limit of resolving the sidebands.

An additional constraint is set by interactions in the condensate shifting the resonance frequency during transfer. Depending on the ratio between the interaction energy and the Rabi frequency $\Lambda = U/\Omega_{transfer}$, with $U = \frac{2\hbar}{m}\bar{n}(a_{11} - a_{22} + f(2a_{12} - a_{11} - a_{22}))$ where a_{ij} are the scattering lengths, \bar{n} the mean density and $f = (n_1 - n_2)/(n_1 + n_2)$ the relative occupation, different regimes are expected [136]. For $\Lambda < 1$ we are in the Rabi regime where the linear coupling is governing the time evolution and single-particle coherence is preserved [18]. For $\Lambda > 1$ we enter the Josephson regime and for $\Lambda > 2$ self-trapping modes appear. Then, the atom transfer within internal states is progressively inhibited and also single-particle coherence is gradually lost [18, 27]. An ideal coherent atom transfer would thus require $\Lambda < 2$ and preferably $\Lambda \leq 1$. As the sideband resolving requirements set an upper limit on $\Omega_{transfer}$, $\Lambda \leq 1$ is fulfilled only for small enough interaction energies U . These are achievable in current experiments, for example, with the use of Feshbach resonances [136] or via the reduction of the density by the use of even shallower traps. Another possibility is to chirp the Rabi pulse in order to compensate for the effects of the interparticle interactions.

3.2.3 The dressed state picture in the microwave regime

We will now develop the Hamiltonian for the interaction of a ^{87}Rb atom in the hyperfine ground state with a microwave field. This work is based on the thesis of P. Treutlein [127] and is adapted to our particular characteristics.

The Hamiltonian of our system has three parts, that of an atom trapped in a magnetic field \hat{H}_A , the microwave field \hat{H}_F and the interaction between the atom and the field \hat{H}_{AF} :

$$\hat{H} = \hat{H}_A + \hat{H}_F + \hat{H}_{AF} \quad (3.7)$$

For the description of a ^{87}Rb atom in the hyperfine split ground state we start with the Breit-Rabi Hamiltonian and neglect the interaction of the static magnetic field with the nuclear angular momentum as it is three orders of magnitude smaller

($g_I/g_J \approx 10^{-3}$) than the orbital angular momentum:

$$\hat{H}_A = A_{hfs} \mathbf{I} \cdot \mathbf{J} + \mu_B B (g_J J_z + g_I I_z) \approx A_{hfs} \cdot \mathbf{I} \cdot \mathbf{J} + \mu_B g_J B_z J_z \quad (3.8)$$

Since $\mu_B B \ll \hbar \omega_{hfs}$ (the Larmor frequency for our trapping field is 2-4 MHz whereas the hyperfine transition is 6.8 GHz) we can treat the magnetic field as a perturbation and take the eigenstates $|F, m_F\rangle$ of the unperturbed ($B = 0$) Hamiltonian and eigenenergies to first order (as done in standard perturbation theory):

$$E_{F, m_F} \approx (F - 1) \hbar \omega_{hfs} + (F - \frac{3}{2}) m_F \mu_B B \quad (3.9)$$

Where $F = I + J$ is the total angular momentum and where $F = 1$ ($F = 2$) for the lower (upper) hyperfine state. The atomic Hamiltonian provides us with 8 states, three for the $F = 1$ manifold of the hyperfine ground state and five for the $F = 2$ manifold.

The microwave field Hamiltonian is simply given by:

$$\hat{H}_F = \hbar \omega (a^\dagger a + 1/2) \quad (3.10)$$

With eigenstates $|n\rangle$ and eigenenergies $E_n = \hbar \omega (n + 1/2)$. The photon number originating from the field Hamiltonian is however not fixed resulting in an infinitely large Hilbert space. At this point we assume the weak coupling limit, where the Rabi frequency of the microwave driving is much smaller than the splitting of these levels (also known as the Jaynes-Cummings model) and will later perform the rotating wave approximation to remove these higher order terms. We will also assume that the detuning of the microwave signal is small in comparison with the hyperfine splitting. We thus limit ourselves to the case where the number of excitation quanta is conserved and focus on the subset of the Hilbert space containing only 8 states:

$$K(n) = |F = 1, m_F = -1, 0, 1\rangle |n + 1\rangle, |F = 2, m_F = -2, -1, 0, 1, 2\rangle |n\rangle \quad (3.11)$$

The labeling "n" here is superfluous, since the overall energy of the total field ($\hbar\omega n$) has no effect on the dynamics and will be removed from the following calculations. It's just here to make it explicit that the number of quanta are conserved in our system, that if a photon is taken from the field it transforms into an atomic excitation and if an excitation is taken from an atom it goes to the field. See Figure 3-6.

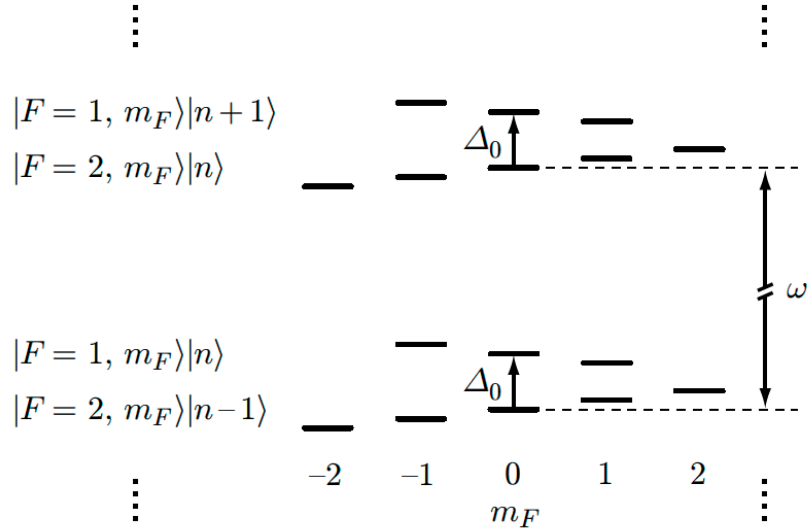


Figure 3-6: Level scheme of the bare states with microwave dressing. Taken from Philipp Treutlein thesis.

We now define the detuning $\Delta_0 = \omega - \omega_{hfs}$ with respect to the resonance at $B = 0$ and write:

$$\begin{aligned} \hat{H}_A + \hat{H}_F = \sum_{m_2} & \left(\frac{1}{2} \hbar \Delta_0 + \hbar \omega_L m_2 \right) |2, m_2\rangle \langle n| \langle n| \langle 2, m_2| \\ & + \sum_{m_1} \left(\frac{1}{2} \hbar \Delta_0 - \hbar \omega_L m_1 \right) |1, m_1\rangle \langle n+1| \langle n+1| \langle 1, m_1| \end{aligned} \quad (3.12)$$

Where $\omega_L = \frac{\mu_B}{2\hbar} |B|$ is the Larmor frequency and where we have removed the total field energy ($\hbar\omega n$) and one common excitation quanta ($\hbar\omega$) so that an atom in the $|F = 1, m_F\rangle |n + 1\rangle$ and one in $|F = 2, m_2\rangle |n\rangle$ are seen as being offset by just the detuning Δ_0 and the relative Zeeman splitting $\hbar\omega_L(m_2 + m_1)$ as seen in figure

3-6).

The atom-field coupling is given by the coupling of the atom's angular momentum to the magnetic field of the microwave signal:

$$\hat{H}_{AF} = \mu_B(g_J \mathbf{J} + g_I \mathbf{I}) \cdot \hat{B}_{MW} \approx \mu_B g_J \hat{B}_{MW} \cdot \mathbf{J} \quad (3.13)$$

Where we again neglected the coupling to the nuclear spin and where \hat{B}_{MW} is the quantized field operator in the Schrödinger picture given by [127]:

$$\hat{B}_{MW} = \frac{B_{MW}}{2\sqrt{\bar{n}}}(\epsilon_{MW} a + \epsilon_{MW}^* a^\dagger) \quad (3.14)$$

With B_{MW} the classical field amplitude, ϵ the polarization vector, a^\dagger and a the raising and lowering operators for the field and \bar{n} the mean number of photons.

We now calculate the expectation values for this Hamiltonian between the 8 states discussed:

$$\begin{aligned} \frac{1}{2} \hbar \Omega_{1,m_1}^{2,m_2} &\equiv \langle n | \langle 2, m_2 | \hat{H}_{AF} | 1, m_1 \rangle | n+1 \rangle = \\ &\langle n | \langle 2, m_2 | \mu_B g_J \frac{B_{MW}}{2\sqrt{\bar{n}}} (\epsilon a + \epsilon^* a^\dagger) \cdot \mathbf{J} | 1, m_1 \rangle | n+1 \rangle = \\ \frac{1}{2} \mu_B g_J B_{MW} \frac{\langle n | a | n+1 \rangle}{\sqrt{\bar{n}}} &\langle 2, m_2 | \epsilon \cdot \mathbf{J} | 1, m_1 \rangle \\ &\approx \mu_B B_{MW} \langle 2, m_2 | \epsilon \cdot \mathbf{J} | 1, m_1 \rangle \end{aligned} \quad (3.15)$$

Where we defined the Rabi frequency Ω_{1,m_1}^{2,m_2} between the two states $|F=1, m_F=m_1\rangle$ and $|F=2, m_F=m_2\rangle$ and took $\langle n | a | n+1 \rangle \approx \sqrt{\bar{n}}$ since for $n \gg 1$ we have $\sqrt{n+1} \approx \sqrt{\bar{n}}$. We also made the replacement $g_J = 2$.

We decompose the $\langle 2, m_2 | \epsilon \cdot \mathbf{J} | 1, m_1 \rangle$ term as following:

$$\begin{aligned} \epsilon \cdot \mathbf{J} &= \epsilon_x J_x + \epsilon_y J_y + \epsilon_z J_z \\ &= \frac{1}{2}(\epsilon_x - i\epsilon_y) J_+ + \frac{1}{2}(\epsilon_x + i\epsilon_y) J_- + \epsilon_z J_z \\ &= \epsilon_+ J_+ + \epsilon_- J_- + \epsilon_\pi J_z \end{aligned} \quad (3.16)$$

The values of the J matrix elements are the Clebsch-Gordan coefficients multiplied by the polarization vector of the atom quantization axis. The orientation of the quantization axis, which determines the axis z over which J_z is defined, is in principle position dependent. As the atoms move in the trapping potential the orientation of the quantization axis follows the field lines of the trap. The polarization vectors of the dressing field ϵ_x, ϵ_y and ϵ_z are also position dependent as the microwave field mode is not homogeneous as we have previously discussed. We will show in the next chapter in detail how this term contributes the majority of the deformation of the trapping potential due to the dressing field.

In the end we get for the Hamiltonian of the total reduced 8-level system:

$$\begin{aligned}
\hat{H} = & \\
& \hbar \begin{bmatrix} \frac{1}{2}\Delta_0 + \omega_L & 0 & 0 & 0 & 0 & 0 & 0 & 0 \\ 0 & \frac{1}{2}\Delta_0 & 0 & 0 & 0 & 0 & 0 & 0 \\ 0 & 0 & \frac{1}{2}\Delta_0 - \omega_L & 0 & 0 & 0 & 0 & 0 \\ 0 & 0 & 0 & -\frac{1}{2}\Delta_0 - 2\omega_L & 0 & 0 & 0 & 0 \\ 0 & 0 & 0 & 0 & 0 - \frac{1}{2}\Delta_0 - \omega_L & 0 & 0 & 0 \\ 0 & 0 & 0 & 0 & 0 & 0 - \frac{1}{2}\Delta_0 & 0 & 0 \\ 0 & 0 & 0 & 0 & 0 & 0 & -\frac{1}{2}\Delta_0 + \omega_L & 0 \\ 0 & 0 & 0 & 0 & 0 & 0 & 0 & -\frac{1}{2}\Delta_0 + 2\omega_L \end{bmatrix} \\
& + \begin{bmatrix} 0 & 0 & 0 & -\sqrt{\frac{3}{4}}\epsilon_- J_- & -\sqrt{\frac{3}{16}}\epsilon_\pi J_\pi & \sqrt{\frac{1}{8}}\epsilon_+ J_+ & 0 & 0 \\ 0 & 0 & 0 & 0 & -\sqrt{\frac{3}{8}}\epsilon_- J_- & -\sqrt{\frac{1}{4}}\epsilon_\pi J_\pi & \sqrt{\frac{3}{8}}\epsilon_+ J_+ & 0 \\ 0 & 0 & 0 & 0 & 0 & -\sqrt{\frac{1}{8}}\epsilon_- J_- & -\sqrt{\frac{3}{16}}\epsilon_\pi J_\pi & \sqrt{\frac{3}{4}}\epsilon_+ J_+ \\ -\sqrt{\frac{3}{4}}\epsilon_- J_- & 0 & 0 & 0 & 0 & 0 & 0 & 0 \\ -\sqrt{\frac{3}{16}}\epsilon_\pi J_\pi & -\sqrt{\frac{3}{8}}\epsilon_- J_- & 0 & 0 & 0 & 0 & 0 & 0 \\ \sqrt{\frac{1}{8}}\epsilon_+ J_+ & -\sqrt{\frac{1}{4}}\epsilon_\pi J_\pi & -\sqrt{\frac{1}{8}}\epsilon_- J_- & 0 & 0 & 0 & 0 & 0 \\ 0 & \sqrt{\frac{3}{8}}\epsilon_+ J_+ & -\sqrt{\frac{3}{16}}\epsilon_\pi J_\pi & 0 & 0 & 0 & 0 & 0 \\ 0 & 0 & \sqrt{\frac{3}{4}}\epsilon_+ J_+ & 0 & 0 & 0 & 0 & 0 \end{bmatrix}
\end{aligned} \tag{3.17}$$

The diagonalization of the complete Hamiltonian is required only when dressing with high power (compared to the Zeeman splitting). In our scheme however ($\Omega < 200\text{kHz} \ll \omega_L \approx 2.3\text{MHz}$) and we will thus use a simple two level model as described

in the next section.

The two level approximation

The Rabi frequencies applied in our experiment are on the order of a few tens of kHz, and are thus much smaller than the Zeeman splitting. We thus have $|\Omega_{1,m_1}^{2,m_2}| \ll \omega_L$ and can assume the AC Zeeman effect shifts only the pair of states being coupled via the microwave field and does not affect neighboring levels. Therefore we can treat the microwave dressed potential pairwise and analyze the system as a two level one. For a two level atom, the energy splitting between the two bare states is simply the generalized Rabi frequency (coherent Rabi splitting) and is given by [30]:

$$\Delta E(B_{MW}) = E_+ - E_- \approx \hbar \sqrt{|\Omega_{1,m_1}^{2,m_2}|^2 + |\Delta_{1,m_1}^{2,m_2}|^2} \quad (3.18)$$

Where the + (-) refers to the upper (lower) dressed state. The contribution of the microwave field to the shift of a single level is obtained by subtracting the shift occurring at zero microwave amplitude, we get:

$$V_{MW}^{\pm} = \frac{1}{2}(\Delta E(B_{MW}) - \Delta E(0)) = \pm \frac{\hbar}{2} \left(\sqrt{|\Omega_{1,m_1}^{2,m_2}|^2 + |\Delta_{1,m_1}^{2,m_2}|^2} - |\Delta_{1,m_1}^{2,m_2}| \right) \quad (3.19)$$

Where we have divided by two to account for the shift of just one level (the shift is symmetric for both states).

The potential including all polarizations

In our system, the microwave coplanar waveguide generates a polarization vector $\vec{\epsilon}_{MW}$ with a mixture of circular and linear polarizations. Thus, for a large microwave field amplitude the two level description begins to fail, and we will need to consider the couplings to all three transitions. For the microwave amplitudes required to create a double well, these extra polarization contributions are important and we will later see how they cause an asymmetry in the dressing of the two clock states. We will add the contributions of the additional σ polarizations to the potential without diagonalizing

the full Hamiltonian, thus neglecting coherent processes. This is justified since the contribution from these states to the total wavefunction is of order $\Omega_\sigma/\Delta_\sigma \ll 1$ [127]. And we work in a situation where the dressing field is closest to the resonance of the π transition and so is detuned by $\Delta_\sigma = \Delta_\pi \pm \omega_L \approx 2\text{MHz}$ from the relevant levels. Furthermore, the Rabi frequency of the σ transitions is proportional to the microwave field component perpendicular to the quantization axis, and so in the center of the trap, where both fields are almost parallel, the Rabi frequency is reduced to $\Omega_\sigma \approx 100\text{kHz}$ even for powers strong enough to create a double well. We thus have $\Delta_\sigma^2 \approx 100 \times \Omega_\sigma^2$ so that we can approximate the potential by:

$$V_\sigma = \frac{\hbar}{2} \left(\sqrt{\Omega_\sigma^2 + \Delta_\sigma^2} - |\Delta_\sigma| \right) \approx \frac{\hbar\Omega_\sigma^2}{4\Delta_\sigma} \quad (3.20)$$

We will thus write the total potential for the $|1, -1\rangle$ state as:

$$V = \frac{\hbar}{2} \left(\sqrt{\Omega_\pi^2 + \Delta_\pi^2} - \Delta_{0\pi} + \frac{\Omega_{\sigma-}^2}{2\Delta_{\sigma-}} - \frac{\Omega_{\sigma+}^2}{2|\Delta_{\sigma+}|} \right) - mgz \quad (3.21)$$

Besides the contribution from the σ_- transition, this potential is identical for both clock states, assuming every blue detuned microwave for the $|1, -1\rangle$ state is replaced with a red detuned field for the $|2, 1\rangle$ state. For the $|2, 1\rangle$ state however, the expression involving $\Omega_{\sigma-}$ must be removed as there is no coupling to the non existent $|1, 2 >$ state. We will later see how this causes an asymmetry in the dressing and to the formation of a double well for the $|2, 1\rangle$ state while $|1, -1\rangle$ remains a single well.

The microwave field modes

We will now describe the microwave mode shape by decomposing the coplanar waveguide into a set of three wires. The field of an infinitely long current carrying wire of width s collinear with the x axis is given by [127]:

$$\vec{B}_{wire}(y, z) = \begin{pmatrix} B_y \\ B_z \end{pmatrix} = \begin{pmatrix} \frac{\mu_0 I}{2\pi s} \left[\arctan\left(\frac{s/2 - y}{z}\right) - \arctan\left(\frac{s/2 + y}{z}\right) \right] \\ \frac{\mu_0 I}{2\pi s} \frac{1}{2} \left[\ln\left(\frac{(s/2 - y)^2 + z^2}{(s/2 + y)^2 + z^2}\right) \right] \end{pmatrix} \quad (3.22)$$

Since we will always work well within the near-field region $\lambda_{MW} \gg z \approx 50\mu\text{m}$ we can derive the microwave field amplitude from Biot-Savart law. Using this basic wire field 3.22 we define the field of a microwave coplanar waveguide (CPW) as being composed of a central wire carrying current I_{MW} and two adjacent wires with a current of $\frac{1}{2}I_{MW}$ and a spacing of w :

$$\vec{B}_{CPW}(y, z) = \vec{B}_{wire}(y, z) + \frac{1}{2}\vec{B}_{wire}(y - w, z) + \frac{1}{2}\vec{B}_{wire}(y + w, z) \quad (3.23)$$

This wire configuration produces the field mode seen in figure 3-7.

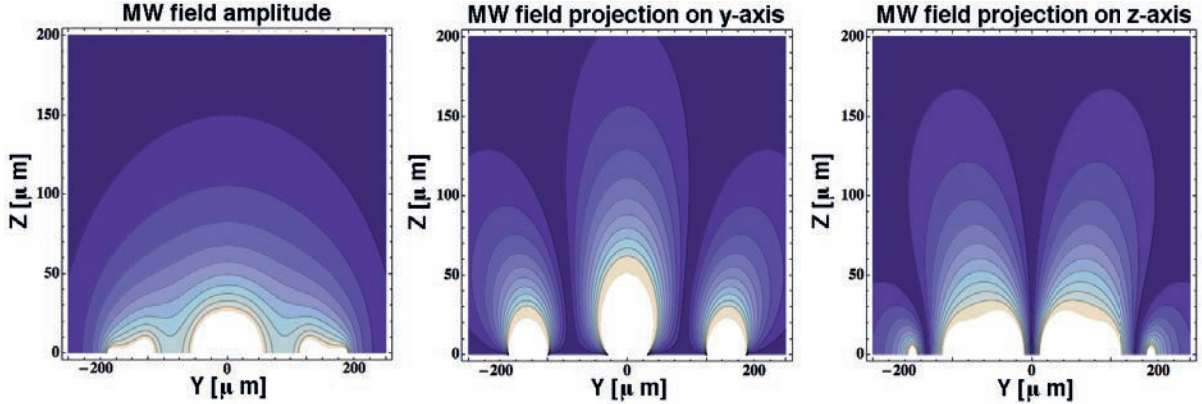


Figure 3-7: The coplanar waveguide mode shape for an arbitrary current I_{MW} . Shown is the amplitude of the total field (left) and the two projections on the y (center) and z (right) axes. At $y=0$ the amplitude and y -projection have $\partial_y = 0$ and exhibit a curvature $\partial_y^2 \neq 0$ the latter allows the creation of a double well potential. The CPW spacing is in our case $w = 175\mu\text{m}$ and all wires have a width $s = 50\mu\text{m}$.

Analytical expressions for the dressing potential

For our trapping configuration, where the quantization axis is oriented along the y axis and placed directly above the central CPW wire, the Rabi frequencies can be

written in the following form:

$$\begin{aligned}
\Omega_\pi &= C_\pi \frac{\mu_B}{\hbar} |\vec{B}_{MW} \cdot \vec{e}_s| = \sqrt{\frac{3}{16}} \frac{\mu_B}{\hbar} |B_{MW}| \cos \phi_s \cos(\theta_{MW} - \theta_s) \\
\Omega_{\sigma^+} &= C_{\sigma^+} \frac{\mu_B}{\hbar} \frac{1}{2} |\vec{B}_{MW} \times \vec{e}_s| = \sqrt{\frac{1}{32}} \frac{\mu_B}{\hbar} |B_{MW}| \sqrt{\cos^2 \phi_s \sin^2(\theta_{MW} - \theta_s) + \sin^2 \phi_s} \\
\Omega_{\sigma^-} &= C_{\sigma^-} \frac{\mu_B}{\hbar} \frac{1}{2} |\vec{B}_{MW} \times \vec{e}_s| = \sqrt{\frac{3}{16}} \frac{\mu_B}{\hbar} |B_{MW}| \sqrt{\cos^2 \phi_s \sin^2(\theta_{MW} - \theta_s) + \sin^2 \phi_s}
\end{aligned} \tag{3.24}$$

where the C_i are the Clebsch-Gordan coefficients, \vec{B}_{MW} the microwave field, \vec{e}_s a unit vector pointing in the direction of the static magnetic field, θ_{MW} the angle on the y-z plane of the microwave field, θ_s the angle on the y-z plane of the static magnetic field and ϕ_s the angle of the static magnetic field on the x-y plane. The factor 1/2 appearing in front of the σ polarization components is due to the decomposition of the circular polarizations done in equation 3.16.

The detunings can be written as:

$$\begin{aligned}
\Delta_\pi &= \Delta_0 + \frac{\mu_B}{\hbar} (|B| - B_0) \\
\Delta_{\sigma^+} &= \Delta_0 + \frac{\mu_B}{\hbar} \left(\frac{1}{2} |B| - B_0 \right) \\
\Delta_{\sigma^-} &= \Delta_0 + \frac{\mu_B}{\hbar} \left(\frac{3}{2} |B| - B_0 \right)
\end{aligned} \tag{3.25}$$

where B_0 is the field at the bottom of the trap where the detuning is Δ_0 . This neglects second order corrections to the trapping potential and assumes the Zeeman splitting is the same for both states. Given that such corrections are on the order of a few kHz, and that Δ_0 is always above 50kHz such an approximation is reasonable.

At the center of the trap, directly above the central CPW wire the mode of the microwave field has an extremum along the y axis for all polarizations thus cancelling the gradient along y. Additionally, the mode is homogeneous along the x axis resulting in a much simplified form for the dressing at the center of the trap. We will thus treat the displacement and formation of a double well along the line $(x, y, z) = (0, 0, z) = r_z$ which passes through the trap center on the x-y plane. At the position of the trap

directly above the central CPW wire the microwave field is oriented along the y axis and is thus almost perfectly collinear with the quantization axis. Also, the minimum of the trap (shifted by gravity) is located for our trap less than a micron away from the center of the quadrupole field and thus the static field along x is nearly cancelled, only by considerably pushing the trap away from its minimum along the z axis will this contribution become important. We thus write:

$$\cos(\theta_{MW} - \theta_s) \cos(\phi_s)|_{r_z} = \cos(\phi_s)|_{r_z} \approx 1 \quad (3.26)$$

Since $z_0 \approx 50\mu\text{m}$ and $w = 175\mu\text{m}$, the central CPW wire is about 3.5 times closer to the atoms than the ground plane wires and is situated exactly below them such that its field is almost fully collinear with the quantization axis as we have discussed. Thus it provides about 90% of the field amplitude allowing us to take only the central wire into account and write for the Rabi frequency:

$$\begin{aligned} \Omega_\pi &= \sqrt{\frac{3}{16}} \frac{\mu_B}{\hbar} \vec{B}_{MW} \cdot \vec{e}_s \approx \sqrt{\frac{3}{16}} \frac{\mu_B}{\hbar} |B_{MW}| = \\ &= \frac{\sqrt{\frac{3}{16}} I_{MW} \mu_0 \mu_B}{\hbar \pi s} \cdot \arctan \frac{s}{2(z_0 + \delta z_{MW})} \end{aligned} \quad (3.27)$$

Where $z_0 \approx 50\mu\text{m}$ is the position of the undressed trap and δz_{MW} is the displacement due to the microwave field.

The low power and large detuning limit

In order to obtain analytical expressions that will allow us to better understand the dressing configuration we will here make the following approximations:

1. We will take the low power limit and neglect the contribution from the σ polarizations
2. We assume the detuning is much larger than the Rabi frequency $\Delta \gg \Omega_\pi$ and larger than the trapping frequencies $\Delta \gg \omega_{trap}$

3. We assume that since the Rabi frequency is low it induces only small displacements $\frac{\delta z_{MW}}{z_0} \ll 1$
4. Since the displacement is small and the detuning large, we assume the Zeeman shift due to the trap to be negligible in comparison to the detuning and write $\Delta \approx \Delta_0$.
5. We treat all three CPW wires only for the zero order term where we take the contribution of the ground wires to second order in w/s , for higher order terms their contribution becomes negligible and we will consider only the central wire.
6. Since the displacement is small we assume that we are still in the region where the static trap can be considered harmonic and thus the trap frequencies ω_x , ω_y and ω_z are assumed to be independent of the displacement δz_{MW} .

Taking these approximations into account we develop the total potential to second order around the point $(0, 0, z_0 + \delta z_{MW})$:

$$\begin{aligned}
V \approx & \frac{1}{2}m (\omega_x^2 x^2 + \omega_y^2 y^2 + \omega_z^2 \zeta^2) + \\
& \frac{3\mu_0^2 \mu_B^2 I_{MW}^2}{64\pi^2 s^2 \hbar \Delta_0} \left(\left(\arctan \frac{s}{2z_0} - \frac{1}{2} \frac{z_0 s}{w^2 + z_0^2} \right)^2 - \frac{4s \arctan \frac{s}{2z_0}}{s^2 + 4z_0^2} \zeta + \frac{4s(s + 4z_0 \arctan \frac{s}{2z_0})}{(s^2 + 4z_0^2)^2} (\zeta^2 - y^2) \right)
\end{aligned} \tag{3.28}$$

Where $\zeta = z - (z_0 + \delta z_{MW})$. Gravity enters only through $z_0 = \frac{g}{\omega_z^2}$ and we have omitted the energy offset $-\frac{1}{2}m\frac{g^2}{\omega_z^2}$. In this expression we see that the microwave dressing has a gradient only along the z axis. As we discussed, it does not exhibit gradients in the x-y plane at the position of the trap directly above the central CPW wire. Furthermore, the curvature along the x axis is only due to the static trap curvature (the microwave field itself has no inhomogeneity along x). This effect is three orders of magnitude smaller than the curvatures for the y and z and is thus neglected. For a detuning of 500kHz this approximation gives reasonable results up to a dressing of about 10dBm. For such detunings the formation of a double well occurs only at much higher powers and so this expression is not suitable for the study of double well potentials and in that respect all we take from it is the fact that the dressing contributes a negative curvature along the y axis which scales like the

current squared I_{MW}^2 . For the full treatment of the formation of the double we will use numerical simulations when the analytical expressions will become too cumbersome.

zero order - the frequency shift

Our approximation for the zero order gives the frequency shift of the dressed state:

$$\frac{1}{\hbar}V(0, 0, z_0) \approx \frac{1}{\hbar} \frac{3\mu_0^2\mu_B^2}{64\pi^2s^2} \frac{I_{MW}^2}{\hbar\Delta_0} \left(\arctan \frac{s}{2z_0} - \frac{1}{2} \frac{z_0s}{w^2 + z_0^2} \right)^2 \approx 2 \times 10^6 \frac{P_{mW}}{\Delta_{f_0}} \frac{\text{kHz}}{\text{mW}} \text{Hz} \quad (3.29)$$

Assuming a 50Ω impedance and where P_{mW} is the power in miliwatts and Δ_{f_0} the detuning in kHz. So for example, for a power of 1mW and a detuning of 500kHz we will get a frequency shift of about 4kHz. Plugging $\delta z_{MW} = 0$ overestimates the frequency shift as the displacement would be towards regions of lower microwave power (for our detuning).

first order - the displacement

In order to find a simple analytical expression for the displacement along the z axis we will take equation 3.28 to first order in δz_{MW} and find the value of δz_{MW} which cancels the gradient along z:

$$\delta z_{MW} \approx \frac{3\mu_0^2\mu_B^2}{\Delta_0 16\pi^2 \hbar} \cdot \frac{I_{MW}^2}{m\omega_z^2} \frac{\arctan(\frac{s}{2z_0})}{s(s^2 + 4z_0^2)} \quad (3.30)$$

We see that we can easily tune the displacement state selectively by choosing an appropriate detuning, we will use this fact later on when we will show how we tune the wavefunction overlap between the two states in the interferometer scheme.

In figure 3-8 we see our approximation next to a numerical calculation of the full dressing potential which takes into account the contributions from all polarizations. We see that for a 500kHz detuning and for powers less than about 5dBm it gives a good approximation but starts to overestimate when reaching a displacement of about $2 \mu\text{m}$. The graph also shows the power needed to form a double well for the $|2, 1\rangle$ state with a detuning of 50kHz.

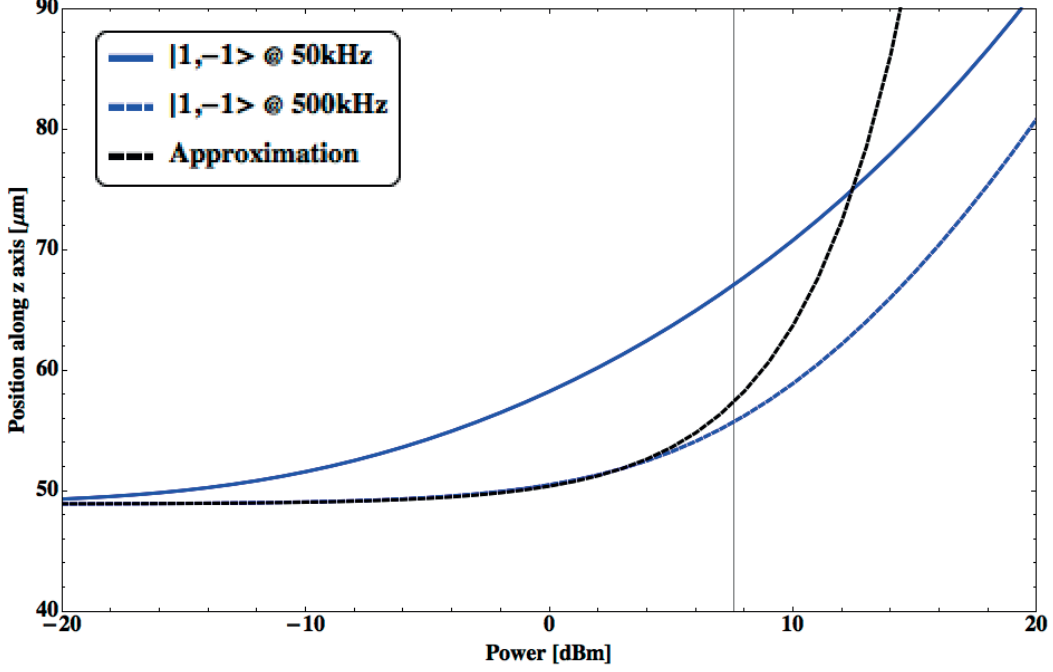


Figure 3-8: Displacement of the trap center along the z-axis due to a microwave dressing with $\Delta_0 = 2\pi 50\text{kHz}$ and $\Delta_0 = 2\pi 500\text{kHz}$. Since the displacement of both states is nearly identical on this scale (see figure 3-9) we only give the $|1, -1\rangle$ displacement. The approximation (in black) is calculated for a detuning of 500kHz and gives the correct displacement only for powers lower than about 5dBm. It overestimates the shift for higher powers as it does not take into account the reduction of the Rabi frequency due to the displacement along z taking the cloud farther away from the chip. Secondly, farther away from the chip an increase of the angle ϕ_s reduces the coupling of the π polarization. The vertical line shows the power needed to form a double well for a detuning of 50kHz for the $|2, 1\rangle$ state.

Figure 3-9 shows the relative displacement between the two states ($\delta_{z_2} - \delta_{z_1}$) along the z-axis for identical but opposite detunings $\Delta_1 = -\Delta_2 = \Delta_0$. The $|2, 1\rangle$ state is pushed further by about 10nm for powers required to form a double well. The reason for the discrepancy is the contribution from the σ^- polarization which does not exist for the $|2, 1\rangle$ state. Since the undressed trap minimum is positioned close to the center of the quadrupole creating the transverse confinement, any displacement along z will increase the contribution of the x-component of the quantization axis due to the quadrupole field. This then increases the contribution from the σ polarizations (which couple to the x component of the quantization axis) creating a positive gradient along z.

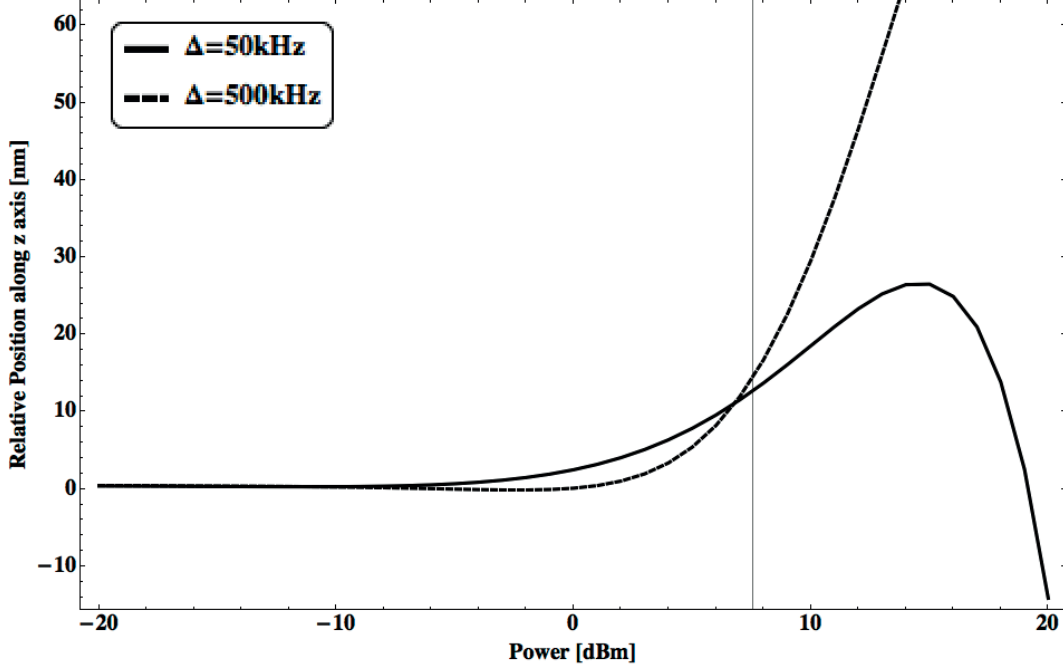


Figure 3-9: Differential displacement along the z-axis of the $|1, -1\rangle$ and $|2, 1\rangle$ state for $\Delta_0 = 2\pi 50\text{kHz}$ and $\Delta_0 = 2\pi 500\text{kHz}$. The $|2, 1\rangle$ state is pushed further by about 10nm for powers needed to form a double well. This discrepancy is due to the contribution from the σ^- polarization which does not exist for the $|2, 1\rangle$ state.

Second order - deformation of the trap

Changing the transverse trapping frequencies

We find an expression for the curvature along the z axis (∂_z^2) by taking the dressing potential to second order in δz_{MW} and write:

$$\partial_z^2 V \approx m\omega_z^2 \left(1 + \frac{3\mu_0^2 \mu_B^2 (s + 4z_0 \arctan \frac{s}{2z_0})}{8\hbar\pi^2 (s^2 + 4z_0^2)^2} \frac{I_{MW}^2}{m\omega_z^2 \Delta_0} \right) \quad (3.31)$$

We see that the effective trapping frequency ω_z is increased linearly with the dressing power as the curvature of the microwave field adds to that of the static trap. This expression neglects the fact that, as we push away the trap from the chip, the field gradients due to the trapping wires reduce, thus reducing the trap frequencies. We however notice that, since the dimple wire creating the transverse confinement is wider ($125\mu\text{m}$ for the dimple Vs. $s = 50\mu\text{m}$ for the CPW wires) and since it is placed on the bottom chip which is $\approx 400\mu\text{m}$ below the CPW, it's gradients are lower for

the same currents. At the position of the new trap the currents in the CPW and dimple are such that the dressing gradient equals that of the static trap since the trap is at equilibrium. Therefore the dressing field contributes the majority of the curvature for the total potential. The more the trap is pushed, the more the dressing curvature becomes dominant over that of the static trap.

In the case of the x-axis trap frequency, the microwave curvature is negligible and thus the trap frequency reduces as the trap gets pushed away from the chip.

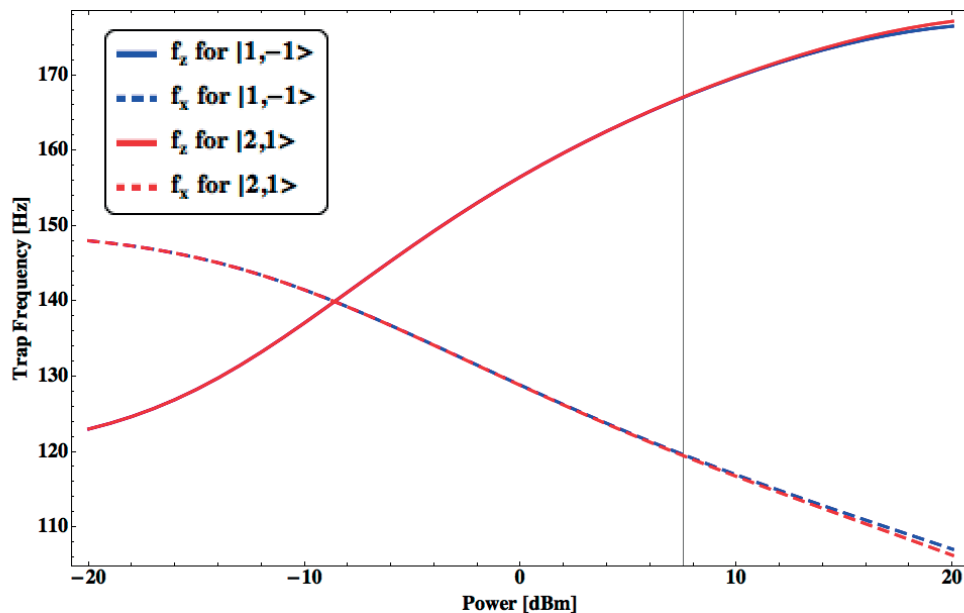


Figure 3-10: The trap frequencies for the x and z axes calculated for the two states. The trap frequencies are calculated for a dressing detuning of 50kHz.

Figure 3-10 shows the calculated trap frequencies along the x and z axes for the two states. The simple approximation derived in 3.31 is not shown since for this low detuning the approximation is poor.

The formation of a double well

In equation 3.28 of the previous section we saw that the dressing field adds to the potential a term proportional to y^2 which reduces the curvature of the total potential. The dressing term originates from the curvature of the microwave field amplitude and polarization and is scaled by the current squared I_{MW}^2 . On the other hand, the static trapping potential contributes a positive curvature term in the form of the harmonic

trapping potential $\frac{1}{2}m\omega_y^2y^2$. Thus, as the power of the microwave field is increased, the total curvature of the potential decreases until it reaches a quartic potential. By increasing the power beyond this point a double well is formed as can be seen in Figure 3-11.

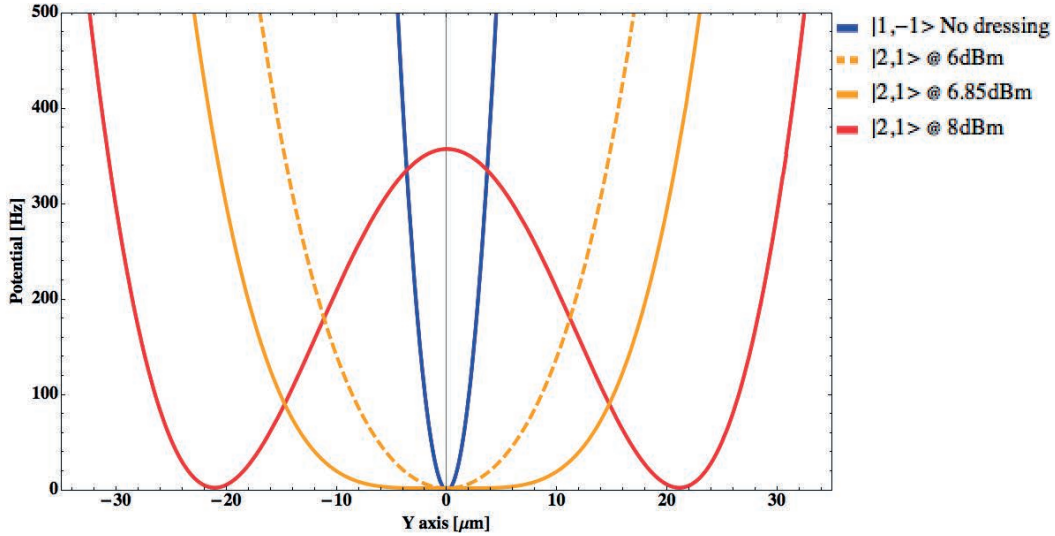


Figure 3-11: The potential for the undressed $|1, -1\rangle$ state and the dressed $|2, 1\rangle$ state for a red detuning of 50kHz from the $|2, 1\rangle \rightarrow |1, 1\rangle$ transition. Similar potentials will emerge for the $|1, -1\rangle$ state if we will replace the frequency of the dressing to be blue detuned to the $|1, -1\rangle \rightarrow |2, -1\rangle$ transition. Without any dressing the trapping potentials of both states are nearly identical as the Ioffe field is close to the magic field. When the power of the dressing is low (6dBm), the negative curvature added is not sufficient to fully compensate the static trap potential and the trap frequency is simply reduced. At a certain power (6.85dBm in this case) the microwave curvature completely compensates the static trap and the potential minimum is flat or "quartic". At higher powers (8dBm) a double well is formed as the total curvature becomes negative at the center of the trap.

Also, as the dressing pushes the atoms farther away from the chip, the static trap along the splitting axis is reduced since the gradients of the trapping wires are reduced farther away from the chip. The simple model developed in 3.28 will however not suffice to characterize the effect of the dressing since we will need to describe the potential for high dressing powers where most of the approximations performed will not hold. We will thus derive analytical expression until they will become too cumbersome and then resort to numerics for the full analysis of the problem.

Taking the potential in 3.21 and differentiating it with respect to y , we get the

following expression for the curvature of the trap:

$$\begin{aligned}
\partial_y^2 V = & \frac{1}{\sqrt{\frac{\Omega_\pi^2}{\Delta_\pi^2} + 1}} \left(\frac{\hbar}{4\Delta_\pi} \partial_y^2 \Omega_\pi^2 + m\omega_y^2 \right) - \frac{\hbar}{4|\Delta_{\sigma+}|} \partial_y^2 \Omega_{\sigma+}^2 + \frac{\hbar}{4\Delta_{\sigma-}} \partial_y^2 \Omega_{\sigma-}^2 \approx \\
& \frac{1}{\sqrt{\frac{\Omega_\pi^2}{\Delta_\pi^2} + 1}} \left[m\omega_y^2 + \frac{\hbar\Omega_\pi^2}{2\Delta_\pi} \left(\underbrace{\frac{\partial_y^2 |B_{MW}|}{|B_{MW}|}}_{\text{Amplitude}} - \underbrace{(\partial_y \theta_{MW} - \partial_y \theta_s)^2}_{\text{Polarization}} \left(\underbrace{1}_{\pi} + \frac{\Omega_\pi}{\Delta_Z} \cdot \left(\underbrace{\frac{1}{6}}_{\sigma^+} - \underbrace{1}_{\sigma^-} \right) \right) \right) \right] \quad (3.32)
\end{aligned}$$

Where we made use of 3.24 and 3.25 and where we have neglected second order terms in ϕ_s and took the approximation $\Delta_0 \ll \Delta_Z$ writing for the detunings of the σ polarizations: $|\Delta_{\sigma+}| \approx |\Delta_{\sigma-}| \approx \Delta_Z$ where Δ_Z is the Zeeman splitting in rad/sec. Here ω_y is understood to be dependent on δz_{MW} and not a static value since as we previously said the static trap frequency is reduced as it is being pushed away from the chip. The curvature of the microwave amplitude $\partial_y^2 |B_{MW}|$ is negative (as can be seen in figure 3-7) and so contributes to the formation of the double well potential by reducing the effective trap frequency. The term $(\partial_y \theta_{MW} - \partial_y \theta_s)^2$ is the largest contribution of the dressing field to the curvature along y (see Figure 3-12) and contains contributions from all polarizations. The contribution from the rotation of the static trap field $\partial_y \theta_s$ is negligible for our trap and the whole polarization effect can be seen as due to the rotation of the microwave field orientation $\partial_y \theta_{MW}$. Although the σ polarizations have a smaller coupling at the center of the trap, their curvatures are larger by the same amount (see Figure 3-7 for example, and compare the y and z components curvatures at the center of the trap). Their contributions are reduced only due to the ratio Ω_π/Δ_Z without the additional scaling due to ϕ_s . For a dressing field of 8dBm and a detuning of 50kHz for example, we get $\Omega_\pi/\Delta_Z \approx 0.07$ and the σ^- polarization reduces the variation due to the polarization by 7%. The difference in the power needed to form the double well for the two states (the power mismatch) is on the order of 1dBm for equal but opposite detunings. This difference, although small, is fundamental to our scheme as it allows us to create a double well

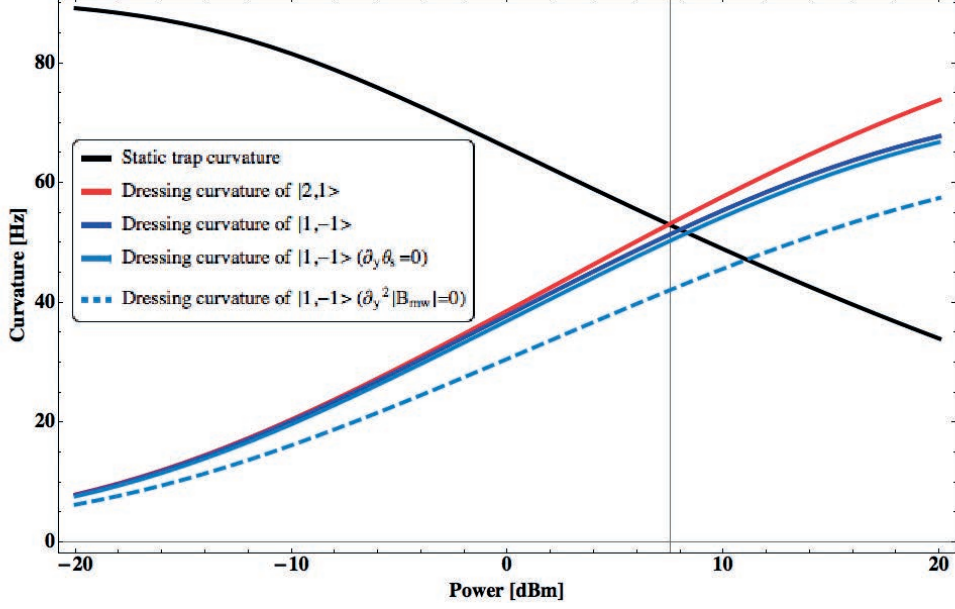


Figure 3-12: All contributions to the curvatures of the dressed potential at $y=0$ expressed in terms of the trap frequency ($\frac{\omega_y}{2\pi} = \frac{1}{2\pi} \sqrt{\frac{1}{m} \partial_y^2 V}$) and where we flipped the sign of the microwave contributions. The simulation is done for an identical detuning $|\Delta_1| = |\Delta_2| = 50$ kHz for both states. The black line shows the static trap contribution which is reduced as the trap is pushed away from the chip. The blue line show the contribution of the dressing field for $|1, -1\rangle$. At the point where they meet (≈ 8 dBm) the total curvature is zero and the potential is quartic. For higher powers the double well starts to form. The red line shows the contribution of the dressing field for the $|2, 1\rangle$ state, which due to the absence of the σ contribution starts to form a double well for lower powers (as indicated by the vertical line). The light blue line shows the $|1, -1\rangle$ dressing without the term $\partial_y \theta_s$ which is the static field rotation. This line is almost identical to the full curvature of the dressing and demonstrates that this contribution is negligible. The light blue dashed line shows the dressing without the $\partial_y^2 |B_{MW}|$ term which is the contribution from the microwave amplitude. It shows that although such a contribution is not negligible, it is 3 times less important than the contribution from the polarization term due to the microwave field orientation $\partial_y \theta_{MW}$.

in $|2, 1\rangle$ state while preserving a single well in $|1, -1\rangle$. It also helps overcome the reduction of the wavefunction overlap along the z direction. This difference means that by dressing both states with identical powers and detunings we can displace them by nearly the same amount (as seen by Figure 3-9), recovering the overlap but still forming a double well for the $|2, 1\rangle$ state. The fact that the power mismatch is small is also advantageous, since although we would like the $|1, -1\rangle$ state to remain

in a harmonic trap, it is beneficial to have its trapping frequency along the splitting axis reduce, increasing the cloud size so that it better overlaps with the double well potential in the $|2, 1\rangle$ state.

Imperfections

An asymmetry of the microwave mode or a displacement of the static trap along the splitting axis (both incorporated in the calculations of 3-12) will increase the z component of the microwave field at the center of the trap, leading to an increased coupling of the σ polarizations and thus to an increased power mismatch. One can also tune the mismatch by changing the Ioffe field. By reducing the Ioffe field the Zeeman splitting will decrease, increasing the Ω_π/Δ_Z term and leading to an enhanced contribution of the σ^- polarization. Changing the Zeeman splitting away from the magic field is of no consequence for our scheme since in any case the interferometer splitting occurs in the same internal state. Increasing the dressing detuning will also increase the power mismatch since for larger detunings the splitting will occur at higher powers thus increasing Ω_π/Δ_Z .

We will now analyze the characteristics of the double well potential including the barrier height, the splitting distance and the trap frequencies at the bottom of the double well potential and will then go on to measure the microwave field generated by our coplanar waveguide.

Barrier height

As the power is increased beyond the critical power for the formation of the double well, the barrier height between the two wells increases. The barrier should be raised beyond the chemical potential of each of the wells so that tunneling between the two wells is suppressed and the split condensates will be able to accumulate a relative phase. Figure 3-13 shows the barrier height as a function of power for the dressing of the two states. The chemical potential for the $|2, 1\rangle$ state is also plotted as a reference. The barrier height crosses the chemical potential for an increase of 0.2dBm beyond the quartic potential point which is still less than what is required to form a quartic

potential for the $|1, -1\rangle$ state indicating that we can transfer atoms to a fully split double well potential and still maintain a harmonic potential in the $|1, -1\rangle$ state and wavefunction overlap along the z axis.

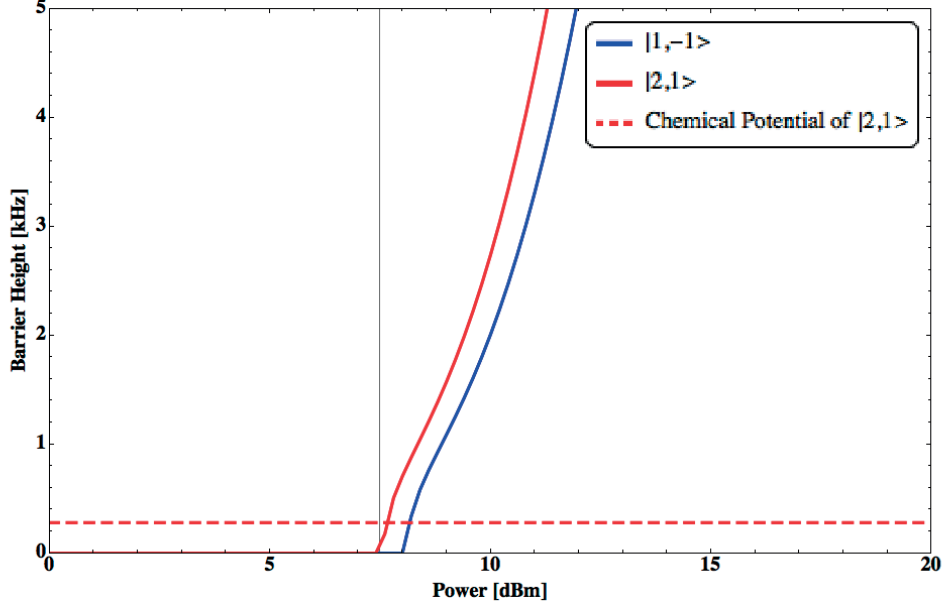


Figure 3-13: Barrier height of the double well potential for a dressing detuning $|\Delta_1| = |\Delta_2| = 50$ kHz. The $|2, 1\rangle$ state becomes a double well ≈ 1 dB before the $|1, -1\rangle$ state. The dashed line shows the chemical potential for 4000 atoms.

Splitting distance

In figure 3-14 we plot the distance between the two wells as a function of power for a detuning of 50kHz. We see that we can create a splitting of $\approx 150\mu\text{m}$ for the moderate power of less than 50mW. We also see that for the power required to cross the chemical potential, the splitting distance for the double well in the $|2, 1\rangle$ state is $\approx 15\mu\text{m}$, for this power the harmonic potential in the $|1, -1\rangle$ state has a trap frequency $\omega_y \approx 2\pi 10\text{Hz}$ and a Thomas-Fermi radius of $\approx 20\mu\text{m}$ (for 4000 atoms) thus reaching the position of the two wells.

Trap frequencies

In figure 3-15 we plot the trap frequencies vs. power. It is interesting to notice that there is a power for which both states have the same trap frequencies for the harmonic

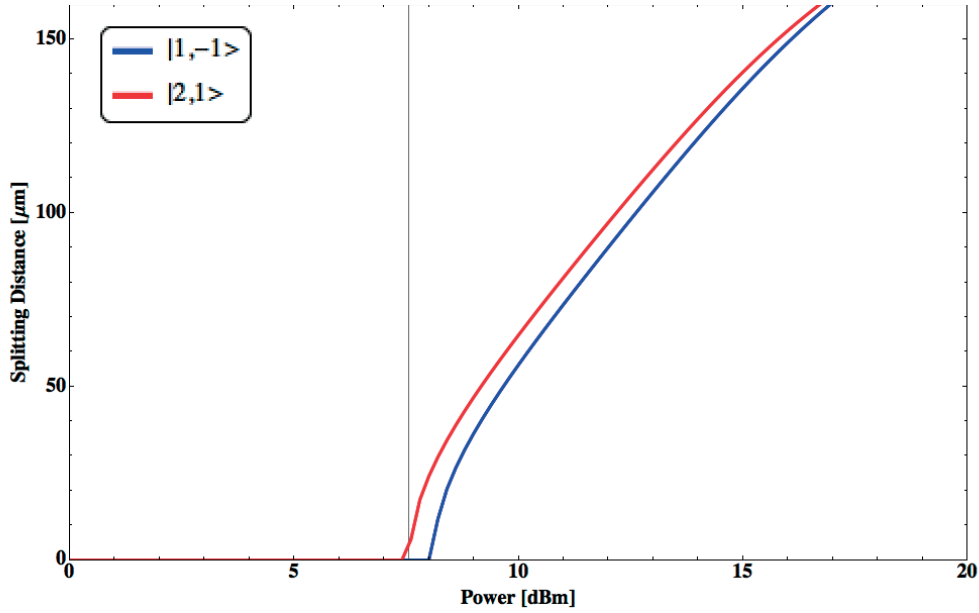


Figure 3-14: Splitting distance of the double well as a function of power for a detuning of 50kHz for the two states.

trap of the $|1, -1\rangle$ state and the double well trap in the $|2, 1\rangle$ state.

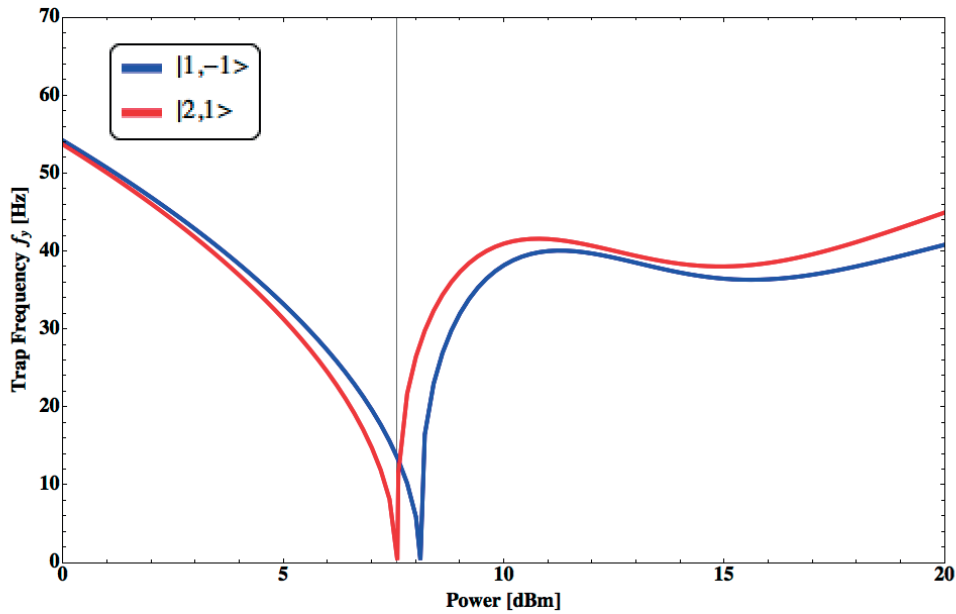


Figure 3-15: The y trap frequency for a detuning of 50kHz for the two states. For powers lower than those required to form a double well, the single trap frequency is plotted. For higher powers the trap frequency at the bottom of the double well is shown. Just above the formation of the double well for the $|2, 1\rangle$ state the double well frequency and the single well frequency can be made identical.

3.3 Measurement of the microwave dressed potential

In the previous section we analyzed the dressing potential using the mathematical form of a perfect CPW mode. In reality however as we will see, the CPW mode is asymmetric due to parasitic couplings from adjacent wires or the back plane chip. In order to characterize the microwave mode we employ a method developed in by the Treutlein group in Basel [14]. We use ultracold atoms from our optical molasses and apply the microwave field from our CPW to couple the two hyperfine ground states. By driving Rabi oscillations and imaging only the $F=2$ states we are able to deduce the spatial distribution of the Rabi frequency from which we are able to deduce the current distribution in the waveguide wires.

3.3.1 Measurement of the microwave mode shape with cold atoms

We prepare a cloud of ^{87}Rb atoms via a magneto-optical trap followed by a 3 ms stage of optical molasses thereby cooling the atoms to $10\mu\text{K}$. We then apply an optical pumping pulse to transfer the atoms in the $|1, -1\rangle$ state. We then launch the atoms towards the chip using a magnetic gradient and as the atoms approach the chip a homogeneous field is switched on to provide a quantization axis that lifts the degeneracy of the Zeeman sublevels, allowing us to couple only one polarization at a time. Then a 20 dBm microwave pulse on resonance with one of the transitions is switched on abruptly for a varying amount of time inducing Rabi oscillations. The atoms are imaged by a laser pulse on resonance with the $|2 \rangle \rightarrow |3' \rangle$ state thus enabling a state selective detection allowing us to measure the Rabi oscillations for each point in the image. Such an image is shown in 3-16 where the microwave was turned on for a period of $100\mu\text{s}$. By scanning the pulse length, the Rabi frequency for each pixel can be deduced as seen in figure 3-17. We perform such a measurement for each of the three polarization (σ^- , π and σ^+) by changing the frequency of the

microwave source to be on resonance with the appropriate transition.

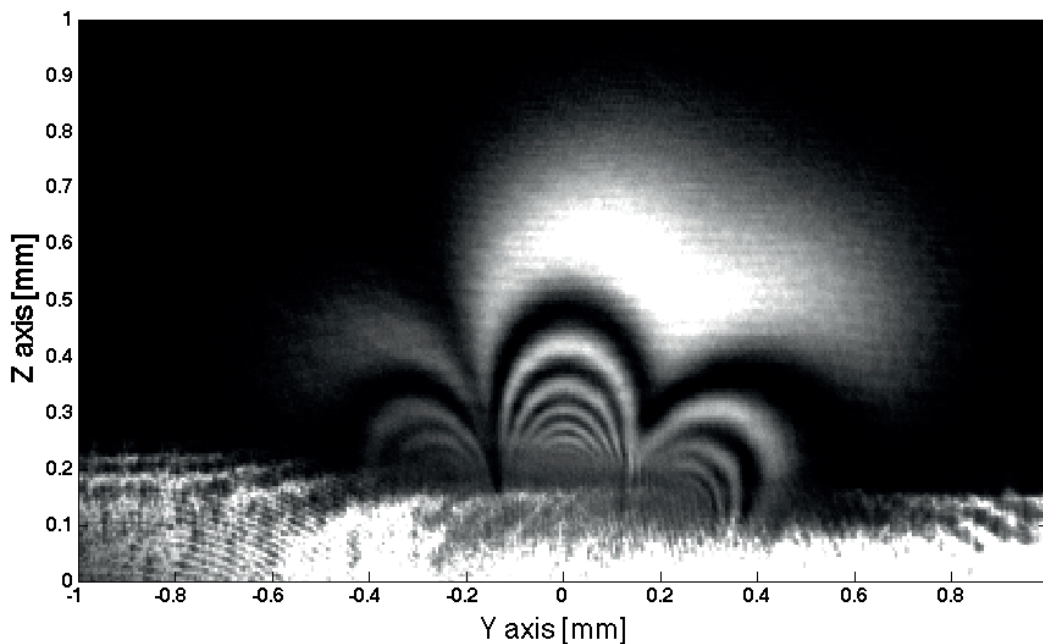


Figure 3-16: Absorption image of a $10 \mu\text{K}$ ^{87}Rb cloud undergoing Rabi oscillations. The chip is positioned parallel to the y axis at $z=0$ with the CPW collinear with the x axis. Here a homogeneous bias field oriented along the y axis is switched on at a value of 3G , after which a microwave field on resonance with the π transition is turned on for a period of $100\mu\text{s}$ before the atoms are imaged. By performing a succession of such images with a varying pulse duration the Rabi frequency can be reconstructed for each pixel.

3.3.2 Extracting the dressing parameters

After measuring the spatial distribution of the Rabi frequency we fit the data with a model of the CPW with three free parameters, the three currents in the three CPW wires. In our initial theoretical treatment we assumed a symmetric mode, here we allow these parameters to change in order to account for the evident asymmetry of the mode (see Fig. 3-16) which is seen to lean to the left. Figure 3-18 shows the fitting procedure on a cross section of the Rabi frequency measurements for all three polarizations.

The mismatch seen farther away from the center of the mode is due to coupling to adjacent wires but does not affect the estimate of the splitting up to a splitting

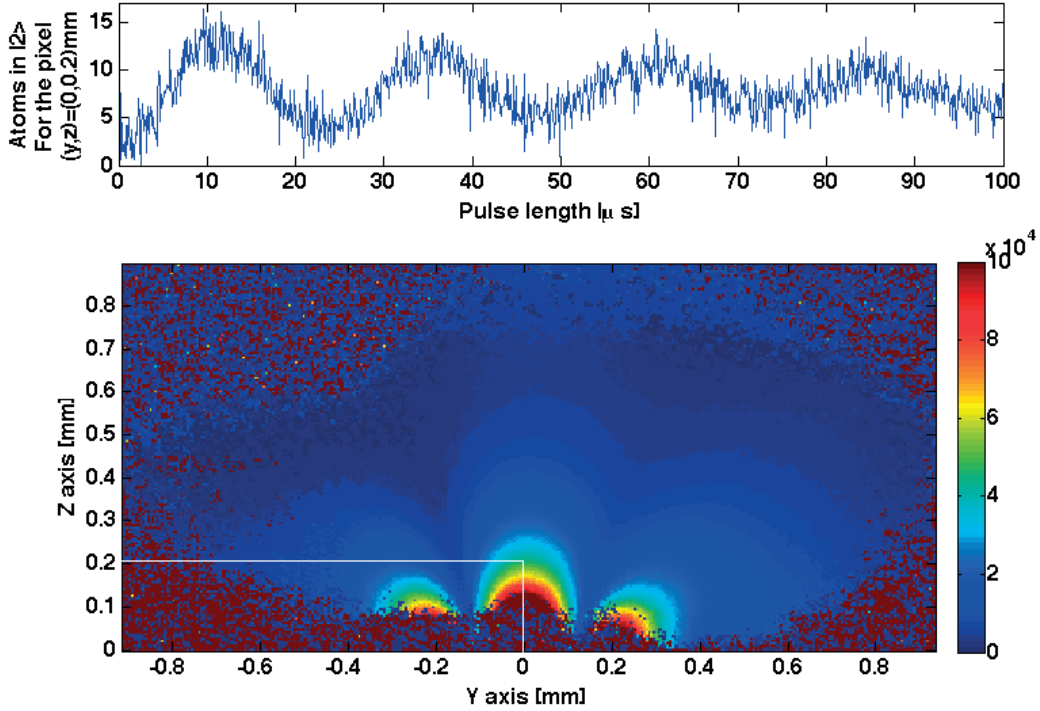


Figure 3-17: Spatial distribution of the Rabi frequency for the π transition as recomposed from images like that in figure 3-16. The trap is positioned at $(y,z)=(0,0)$. The number of atoms detected in $F=2$ (top) for the pixel positioned $(y,z)=(0,0.2)$ mm from the trap position are fit with a sinusoidal function to extract the Rabi frequency. The same is done for all pixels giving the spatial distribution of the Rabi frequency (bottom). The color bar gives a scale for the Rabi frequency in Hz.

distance of $\approx 150\mu\text{m}$. The fitting (seen in figure 3-18) gives a loss of 2.3 dB with respect to the synthesizer output and a current 10% higher in the left ground wire with a return current 5% lower than input indicating possible losses to adjacent wires.

3.3.3 Experimental results confirming our characterization

Taking the fitted mode shape we estimate the frequency shift induced on the cloud by the dressing at low power of only the $|1, -1\rangle$ state. Figure 3-19 shows the result vs. the detuning of the microwave dressing the $|1, -1\rangle$ transition. Each point in the graph was taken by performing a Ramsey measurement on the clock transition while the dressing of ≈ 0 dBm was turned on. The dressing field detuning was then scanned across the resonances of the $|1, -1\rangle \rightarrow |2, -2\rangle$ and $|1, -1\rangle \rightarrow |2, -1\rangle$ transitions.

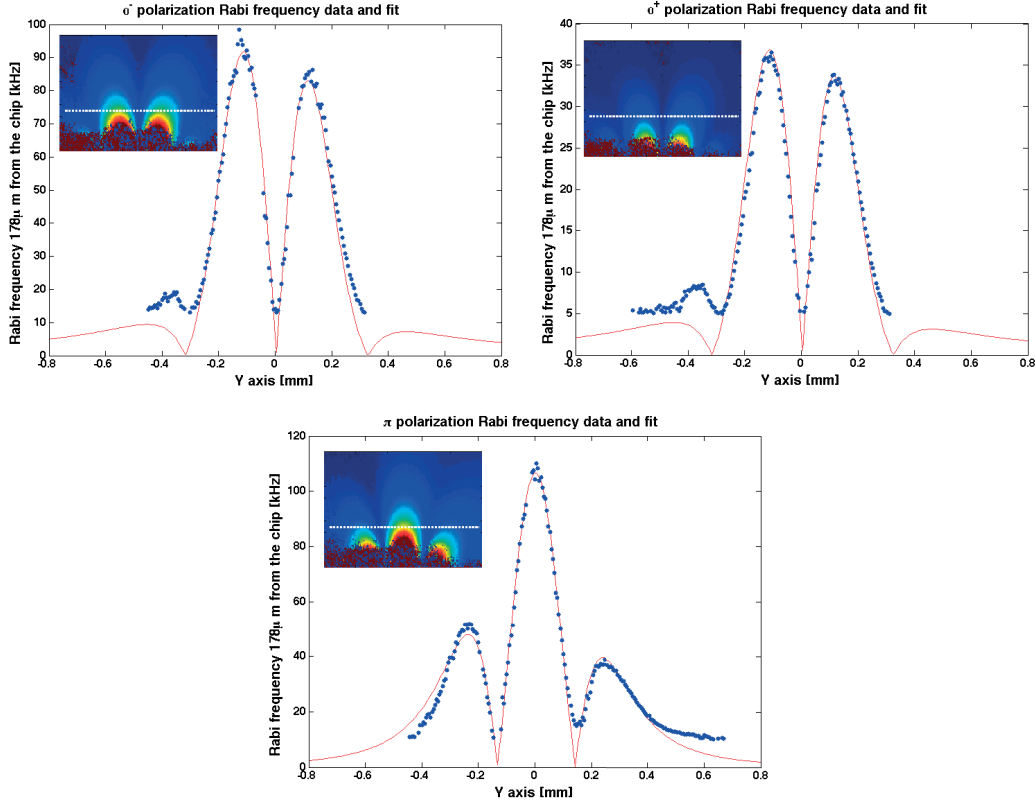


Figure 3-18: On resonance Rabi frequency distribution above the waveguide for σ^- (left), π (center) and σ^+ (right) polarizations. The graphs give the cross section positioned $z=0.18$ mm from the position of the trap (marked by white dotted lines in the insets). We fit (solid red lines) the microwave mode (using equation 3.22) with three independent currents in the CPW. The fitting gives a loss of 2.3dB with respect to the synthesizer output and a current 10% higher in the left ground wire. The return current is found to be 5% lower than input indicating possible losses to adjacent wires. We checked for consistency on several cross section positions and found a good agreement.

The simulation which incorporates the fitted microwave mode shape is shown as a solid line.

In order to fit the simulation to this measurement, we allowed 2 free parameter: the attenuation of the microwave field was reduced by $\approx 1\text{dB}$ in order to accommodate the data. This scaling is reasonable given that measurements were taken a few months apart and the fact that the microwave power was observed to fluctuate by a fraction of a dB on a weekly basis and would fluctuate by up to 2dB when disconnecting and reconnecting cables on the path from the synthesizer to the CPW. Secondly, the

position of the trap from the center of the mode was shifted by 3 microns in order to accommodate the bump at the resonance with the $|1, -1\rangle \rightarrow |2, -2\rangle$ transition. Without such a shift we could perfectly recover the other features but could not replicate the bump. Such a small shift is reasonable considering that a displacement of the y coils relative to the central CPW wire by one mm would shift the trap center by $\approx 10\mu\text{m}$. The displacement augments the contribution of the σ^- coupling since by displacing the trap from directly above the CPW central wire the microwave field obtains a component along z which is transverse to the static trap field, thus enhancing the coupling to σ transitions at the center of the trap.

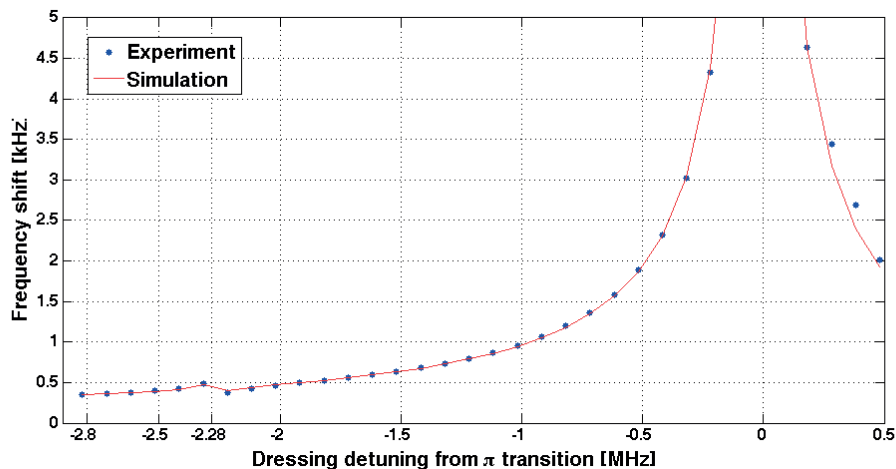


Figure 3-19: Shift of the clock frequency measured by Ramsey spectroscopy when dressing the $|1, -1\rangle$ state. The dressing power is $\approx 0\text{dBm}$. The dressing detuning is given with respect to the $|1, -1\rangle \rightarrow |2, -1\rangle$ transition. The theory curve fits well after adjusting the attenuation of the microwave signal by $\approx 1\text{ dB}$ relative to the value found in our analysis of the microwave mode shape (figure 3-18).

3.4 Results: state selective single well potentials

Before presenting experimental results on the double well potential we dress only $|1, -1\rangle$ and use the z-gradient of the dressing to create an interferometer where $|1, -1\rangle$ is shifted with respect to $|2, 1\rangle$ to spatially separate the two. Following the idea of Treutlein [125] and Böhi et al. [15] we enclose the microwave dressing of the $|1, -1\rangle$

state in between the two Ramsey $\pi/2$ pulses of a clock measurement, thereby leaving the $|2, 1\rangle$ state to act as a reference for the measurement of the $|1, -1\rangle$ frequency shift.

In such a scheme, similar to a Ramsy-Bordé interferometer, we reversibly entangle the internal and external states of the atoms and read the resulting frequency shift from the relative population of the two clock states. In Fig. 3-20 the main idea of the experiment is shown. We start by applying a $\pi/2$ pulse from a horn antenna, thereby placing the atoms in a superposition of the two clock states ($|1, -1\rangle \rightarrow \frac{1}{\sqrt{2}}(|1, -1\rangle + |2, 1\rangle)$). Immediately following the first pulse we switch on the microwave dressing within $50 \mu\text{s}$, sufficiently slow compared to the Larmor frequency but much faster than the trap frequencies so that the $|1, -1\rangle$ state experiences a sudden displacement of the trapping potential and starts to oscillate in the trap. After a varying amount of time we switch off the microwave and apply the second $\pi/2$ pulse to close the interferometer. The two-photon transition in our Ramsey sequence is calibrated to be on resonance when the states are undressed, thus the frequency of the Ramsey fringes is due only to the shift of the $|1, -1\rangle$ state just like in the measurement performed in figure 3-19.

We dress the $|1, -1\rangle$ state with a power of -0.6dBm and a detuning of $+382\text{kHz}$ for the π transition creating a nominal displacement of $0.6\mu\text{m}$ along the z axis. After the $|1, -1\rangle$ state oscillates half a period the atoms reach the opposing side of the dressed trap with a separation of $1.2\mu\text{m}$. Even at this maximum splitting the two wavefunction are not completely separated as they have a Thomas-Fermi radius of $3\mu\text{m}$ ($N=4000$).

The Ramsey fringes in the time domain seen in Fig. 3-20 have a frequency of 2kHz and exhibit a modulation of the contrast due to the varying overlap between the two states. When the dressing is stopped, the interferometer is immediately closed leaving the $|1, -1\rangle$ state at a position based on the phase of its oscillation in the dressed trap. The overlap with the $|2, 1\rangle$ state will then oscillate with the trap frequency ($\omega_z = 2\pi \cdot 125 \text{ Hz}$) leading to the observed modulation of the contrast.

The total frequency shift is mainly composed of the AC Zeeman shift induced by the microwave potential; at the new trap position, the Zeeman shift for the static po-

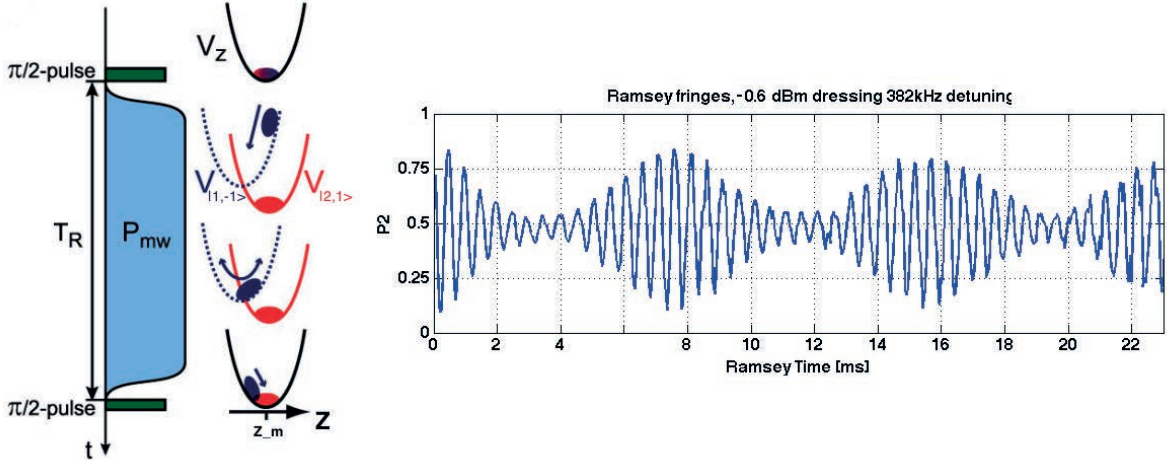


Figure 3-20: Ramsey fringes in the presence of a microwave dressing for the $|1, -1\rangle$ state. The Ramsey sequence with microwave dressing is depicted on the left (taken from [15]). A 50ms long $\pi/2$ pulse is followed by microwave dressing which is switched on within $50\mu\text{s}$ and induces a displacement along z of the $|1, -1\rangle$ state. After a varying Ramsey time the microwave field is turned off and a second $\pi/2$ pulse is immediately applied to close the interferometer. The resulting Ramsey fringe contrast is modulated by the trap frequency of the dressed potential ($\omega_z = 2\pi \cdot 125$ Hz).

tential contributes only $\Delta f_t = \frac{1}{2}m\omega_z\delta z^2 \approx 35\text{Hz}$ out of the total 2 kHz. Unlike in the experiment of Böhi et al., we displace the atoms vertically and are thus in principle sensitive to gravity with an associated frequency shift of $mg = 2\text{kHz}/\mu\text{m}$. The experiment shown in 3-20 has then an average gravity induced shift of $mg\Delta z \approx 1.3\text{kHz}$. However, as we saw in equation 3.28 gravity does not enter into the expression of the frequency shift directly since it is exactly cancelled out by the harmonic trapping potential. Thus any displacement from the equilibrium point $z_0 = g/\omega_z^2$ will induce a frequency shift only due to the trapping potential, whereby g only sets z_0 . A way to work around this difficulty was proposed in the work of Baumgartner et. al. [11] discussed previously, where by performing spectroscopy on the Zeeman sublevels one can separate the electromagnetic contribution from that of gravity. The transfer of a trapped state to an untrapped state occurs in the position of the trapped wavefunction and thus both states have a common gravity term thus allowing one to measure only the contribution from the magnetic (static + dressing) fields. In our scheme for example, one could measure the frequency shift of the $|1, -1\rangle$ state relative to the

untrapped $|1, 0\rangle$ or $|2, 0\rangle$ states via RF or microwave spectroscopy and subtract from it the shift of the $|1, -1\rangle \rightarrow |2, 1\rangle$ transition. The difference between the two will give the contribution of gravity $mg\delta z$.

In any case, whether one wishes to measure gravity or any other field distribution using such a scheme, the precision of the measurement will depend on the exact estimation of the displacement δz . We would thus like to extract the exact displacement, along all axes directly from the data without the need to resort to simulations of the potentials. The separation between two interfering wavefunctions can be extracted either directly from the image of the clouds or from the fringe spacing of the resulting interference signal. In the next sections we will propose a new method which elaborates on the fringe spacing technique by using a homodyne measurement to extract the spatial phase gradients from a Ramsey measurement.

3.4.1 Internal and external coherence

Up to now we have only discussed the time variation of the internal state coherence i.e. the probability to find atoms in the $|2, 1\rangle$ state (Ramsey fringes) which only required us to count the number of atoms in each state. We will now analyze the external coherence taking the images of the atom clouds from which we will extract important information about the dynamics of the split wavepacket. When the wavepackets are recombined with a certain separation, the spatial gradient of the relative phase causes spatial interference fringes in addition to the internal state Ramsey oscillations.

We analyze this situation by writing the total wavefunction in the following way [93]:

$$\Psi(\hat{r}, t) = \sqrt{N_1}\psi_1(\hat{r}, t)e^{i\phi(t)} + \sqrt{N_2}\psi_2(\hat{r}, t) \quad (3.33)$$

Where ψ_1 and ψ_2 are the single particle wavefunctions of the states $|1, -1\rangle$ and $|2, 1\rangle$, N_1 and N_2 their atom numbers and $\phi(t)$ a relative phase between the two states.

When detecting the atom clouds we get for the density:

$$n(\hat{r}, t) = |\Psi(\hat{r}, t)|^2 = N_1|\psi_1|^2 + N_2|\psi_2|^2 + 2\sqrt{N_1N_2}\Re(\psi_1\psi_2^*e^{i\phi(t)}) \quad (3.34)$$

where \Re denotes the real part of the product of the two wavefunctions. The interference pattern after release from the trap and following a t_{TOF} expansion time will be given by [34]:

$$2\sqrt{N_1N_2}\Re(\psi_1\psi_2^*e^{i\phi(t)}) \approx A(r, t) \cos\left(\frac{m \cdot d \cdot x}{\hbar t_{TOF}} + \phi(t)\right) = A(r, t) \cos\left(\frac{m \cdot d \cdot x}{\hbar t_{TOF}} + \Delta_R t\right) \quad (3.35)$$

Where $A(r, t)$ is the envelope of the expanding condensates representing the overlap, d the wavefunction separation at t_{TOF} the time of detection, x the detection position, $\phi(t)$ the homogeneous phase associated with the Ramsey oscillations ($\phi(t) = \Delta_R t$) with Δ_R the detuning between the Ramsey pulse and the energy spacing between the two states. The first term in the cosine is equivalent to a Young's double slit experiment with a slit separation d where the spatial phase associated with the relative motion of the two condensates produces spatial fringes [9]. When the two condensates occupy the same spatial position, d vanishes and we recover the simple Ramsey oscillations. Alternatively, when the two condensates are released with a separation d , a phase gradient is superimposed on the common phase of the atoms.

Some details of the theory given here should be elaborated upon. Reference [34] from which equation 3.35 is taken discusses the interference of two BEC's in the same internal state. In our case, the two wavefunctions interfere after a Ramsey sequence and can thus be in any general superposition of the two internal states. This however does not pose a problem since interference can occur between identical coherent superposition states. As long as the interferometer sequence (Ramsey sequence) is properly closed (the two paths are indistinguishable) spatial interference can occur and the use of equation 3.35 is allowed. The term $\frac{m \cdot d \cdot x}{\hbar t_{TOF}}$ which describes the spatial phase gradient contribution originates from the relative velocity of the two interfering

paths. After the release from the trap, two interfering paths spaced by d have a relative velocity both due to the expansion of the clouds and due to any center of mass relative velocity they might have had in the trap. After an expansion time t_{TOF} the two paths interfere at point x , the phase gradient is extracted and the total relative velocity (expansion+center of mass velocity) is deduced. Since the expansion time t_{TOF} is known, the initial separation d can be extracted.

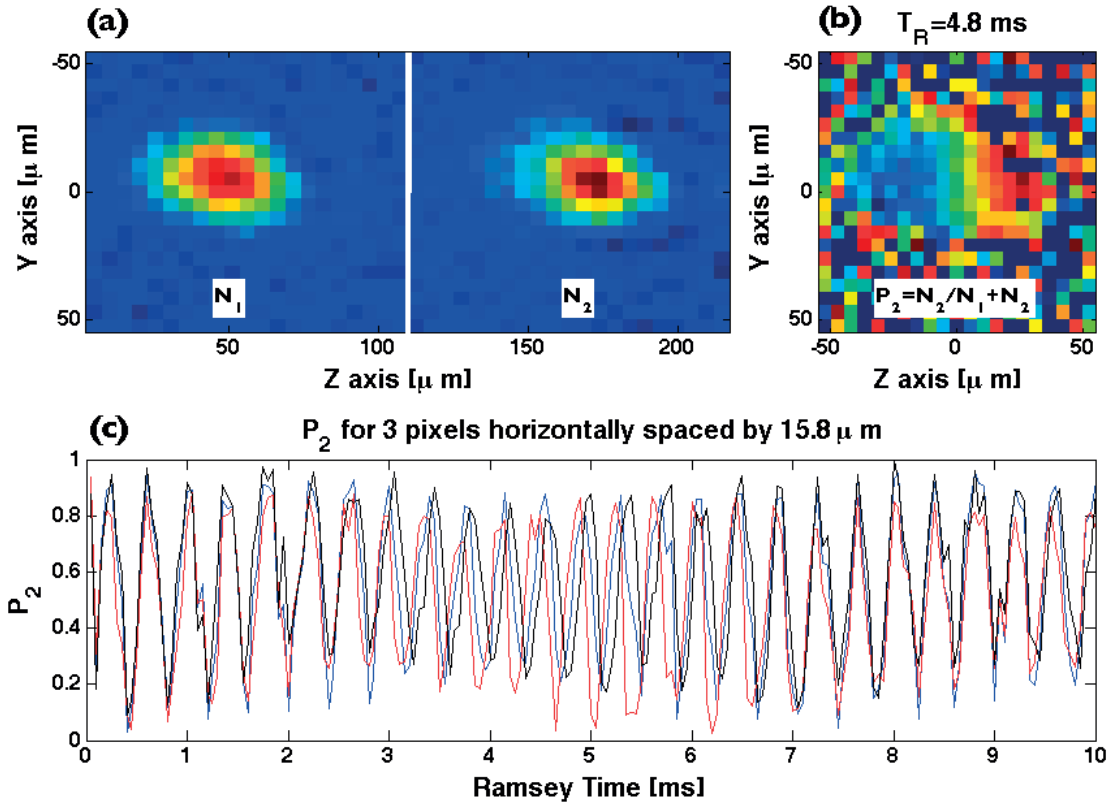


Figure 3-21: Spatial distribution of Ramsey fringes. The sequence was taken with a dressing of 0dBm, a detuning of 382kHz and a dressing power ramp of 10ms. Immediately after the second $\pi/2$ pulse we release the trap and detect both states after 15ms of time-of-flight (a). We superimpose the images of $|1, -1\rangle$ and $|2, 1\rangle$ and calculate the P_2 for each pixel (b). In order to find the best overlap of the frames we calculate the correlation between the images and find the relative offset which produces the largest anti-correlation. We get such an image for every Ramsey time providing us with a film of the P_2 dynamics. In (c) we plot the Ramsey sequence for three different pixels horizontally separated by $15.8\mu\text{m}$ (which is the spacing of 3 pixels) around the central pixel at $(y,z)=(0,0)$. We see that the decrease in contrast of the total P_2 is also due to a phase shift in the oscillations at different positions in the cloud due to the appearance of a spatial phase gradient which then reduces the contrast for the whole ensemble.

The appearance of spatial fringes introduces an additional reduction of contrast in addition to the reduced overlap. We analyze this reduction with a simple 1 dimensional toy model where we take the shape of the overlap function to be a Gaussian envelope $A(x) = A_0 \frac{1}{\sqrt{2\pi}\sigma} e^{-\frac{x^2}{2\sigma^2}}$

For each shot of the Ramsey experiment, the count of atoms in one of the states will be given by a spatial integration of the density, or:

$$\int_{-\infty}^{\infty} A(x) \cos\left(\frac{mdx}{\hbar t_{TOF}} + \omega t\right) dx = \int_{-\infty}^{\infty} A_0 \frac{1}{\sqrt{2\pi}\sigma} e^{-\frac{x^2}{2\sigma^2}} \cos\left(\frac{mdx}{\hbar t_{TOF}} + \omega t\right) dx = A_0 e^{-\frac{1}{2}\left(\frac{dm\sigma}{\hbar t_{TOF}}\right)^2} \cos(\omega t) \quad (3.36)$$

We see that the contrast decays like e^{-d^2} regardless of the contribution from the overlap (which is encoded in A_0 and σ). As the separation between the two wavepackets d becomes larger, the spatial oscillations become stronger and more fringes appear in the image. At the limit of large d , the spatial fringes will integrate to zero and the oscillating term in equation 3.34 will vanish. The average population in each shot will then be 50% and the Ramsey oscillation will not be visible.

The correlation between the internal and external coherence can be seen in figure 3-21 (c) which shows the Ramsey fringes for three pixels displaced by $15.8\mu\text{m}$ ($=3$ pixels). As the wavepackets separate, the Ramsey signal for adjacent pixels is phase shifted by the corresponding term $\frac{md\Delta x}{\hbar t_{TOF}}$ where Δx ($= 15.8 \mu\text{m}$) is the separation between the two pixels. This phase shift results in a reduced contrast when all pixels are summed up.

3.4.2 Wavepacket separation from phase gradients

Further exploiting the phase information encoded in each pixel, we take the spatial P_2 images and generate a map of the relative phase from which we can accurately obtain the spatial separation at t_{TOF} by fitting the phase gradients. In figure 3-22 we take the images of a Ramsey experiment and using a running interval 0.5 ms long [t-0.25 ms, t+0.25 ms] we extract the phase of the Ramsey oscillation for each pixel. In such a way we get a phase map of the interference pattern from which we fit the

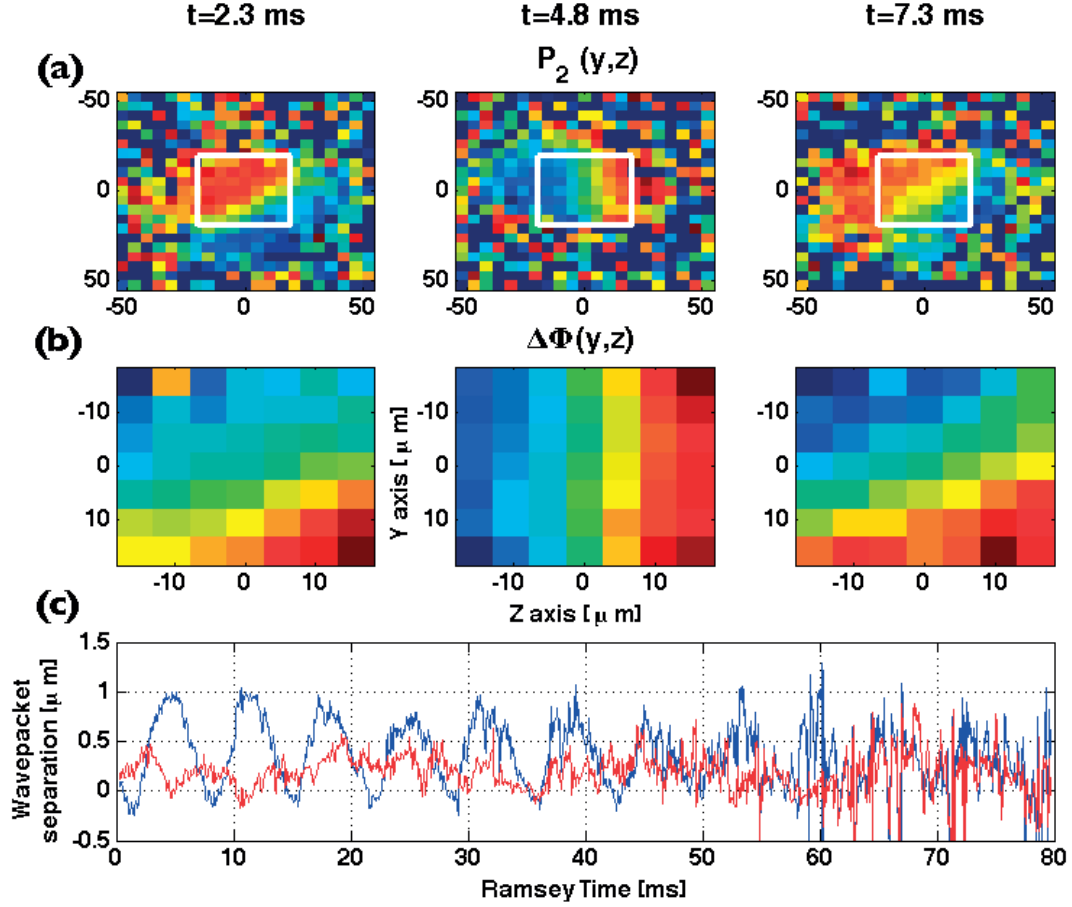


Figure 3-22: The wavepacket separation at $t_{TOF} = 15$ ms deduced from the phase gradients. In (a) we see three examples of the spatial P_2 images for three different times $T_R = (2.3, 4.8, 7.3$ ms). For each such image we take the central 7x7 pixels region (white rectangles) and find for each pixel the phase of the Ramsey signal from the P_2 oscillations. To do so we take a time interval 0.5ms long ($[t-0.25\text{ms}, t+0.25\text{ms}]$) which is slightly longer than the average Ramsey period of 0.4ms so that we always fit at least one full oscillation. We then construct a spatial map of the phase relative to the central pixel (b) and fit a tilted plane to find the phase gradients along y and z. By using equation 3.37 we extract the wavepacket separation along the two axes (c). At $t=4.8\text{ms}$ for example, the displacement is maximal for the z axis and 0 for the y axis, this is represented on the spatial phase distribution by a gradient which is fully along z. The oscillation along z is approx. 140Hz while the oscillation along y is a beat of the oscillation along the x ($\omega_x = 2\pi 166$ Hz) and y ($\omega_y = 2\pi 88$ Hz) axes indicating that the imaging plane is tilted relative to the orientation of the trap.

phase gradients along the two axes ($\phi(y, z) = \phi_0 + \partial_y\phi \cdot y + \partial_z\phi \cdot z$). From the phase gradients we can then extract the wavepacket separation using:

$$d_i = \partial_i \phi \times \frac{t_{TOF} \hbar}{m} \quad (3.37)$$

Where d_i and $\partial_i \phi$ are the wavepacket separation after time-of-flight and phase gradient along the direction i ($=y,z$). In figure 3-22 we see the extracted wavepacket separation as a function of time. The separation signal of the z axis shows a clear oscillation at a frequency of 140 Hz which is close to ω_z . The separation along the y axis contains contributions from the x axis oscillation at $\omega_x = 2\pi 166$ Hz and that along y with $\omega_y = 2\pi 88$ Hz indicating that the imaging axis has a tilt relative to the trap axis. We observe a maximal separation of $1.2 \mu\text{m}$ along the z axis. This matches our simulation as we have estimated a displacement of the trap minimum of $\delta z_{MW} = 0.6 \mu\text{m}$ generating a maximal displacement of $2\delta_z$ as the atoms reach the opposing turning point at the other side of the trap (see fig. 3-20).

The low noise characteristic of our method is seen by the low standard deviation of the extracted signal. On the z axis oscillations we get a root mean square noise on the distance estimation of ≈ 70 nm which is almost two orders of magnitude smaller than the the $5.23 \mu\text{m}$ pixel size.

3.5 Results: state selective double well potentials

In this section we present results on the population of the double well potential formed in the $|2, 1\rangle$ state from atoms trapped in a single well potential in the $|1, -1\rangle$ state. After the characterization of the potentials we present results from two regimes characterized by different transfer Rabi frequencies:

1. Rabi frequencies larger than any trap frequency $\Omega_{transfer} \approx 5\omega_x$ where ω_x is the highest trap frequency
2. Rabi frequencies smaller than any trap frequency $\Omega_{transfer} \approx 0.5\omega_y$ where ω_y is the smallest trap frequency

3.5.1 Characterization of the double well potential

We begin by characterizing the formation of a state selective double well. Figure 3-23 shows the atoms in $F=2$ and $F=1$ after 8 and 11 ms time-of-flight respectively (we have chosen a convention where the image is turned to the side and gravity points to the left). The trap was dressed with a power of 10.5 dBm and a detuning $\Delta_1 = -\Delta_2 = 52$ kHz. A $\pi/2$ pulse was driven on the clock transition to populate both potentials. One observes that the $F=1$ cloud originates from a single well and that the $F=2$ cloud is split into two along the horizontal axis (of the lab frame) with a splitting distance of $50 \mu\text{m}$ in this image.

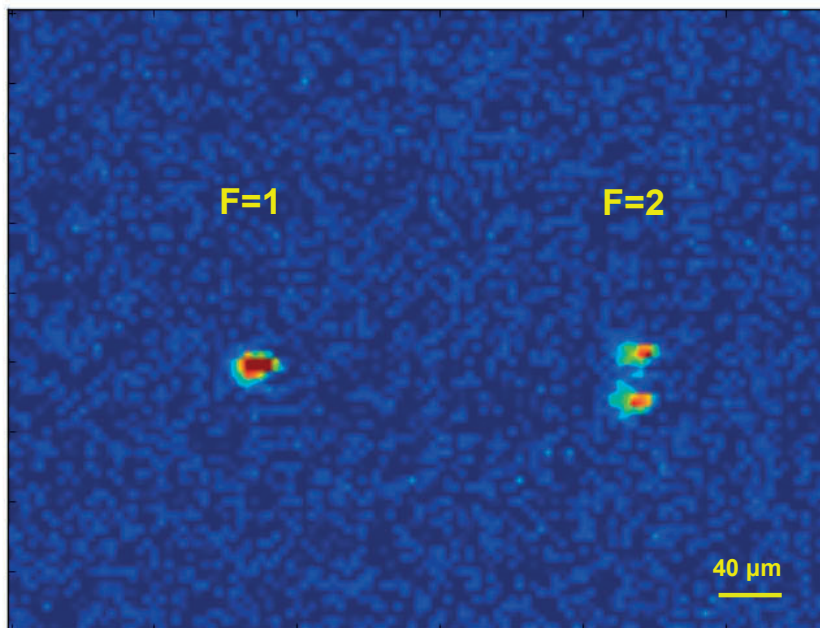


Figure 3-23: Absorption image of the atoms in $F=2$ and $F=1$ after 8 and 11 ms time-of-flight respectively. Gravity in this image points to the left. The two states were dressed with a power of 10.5 dBm and an equal detuning of $\Delta_1 = -\Delta_2 = 52$ kHz followed by a $\pi/2$ pulse on the clock transition to equally populate the two states. One observes that the $F=1$ cloud originates from a single well and that the $F=2$ cloud is split into two indicating the presence of a double well potential. The splitting distance for the $|2, 1\rangle$ state is in this image $50 \mu\text{m}$.

In order to determine the in-situ splitting distance, we record time-of-flight images

like the one in figure 3-23 for various hold times in the trap spanning a few trap periods. We dress the two states with a detuning of $\Delta_1 = \Delta_2 = 382$ kHz and various powers. The central position is then extracted from the fit of the oscillation. Figure 3-24 shows the results together with our previously calibrated simulation. The agreement with theory is good and is limited by uncertainties in the static magnetic field distribution generated by the coils. For high power of 15 dBm and above, we also observe the formation of a double well potential for the $F=1$ state showing our ability to form several versatile combinations: two single wells; a single and a double well; and two double wells.

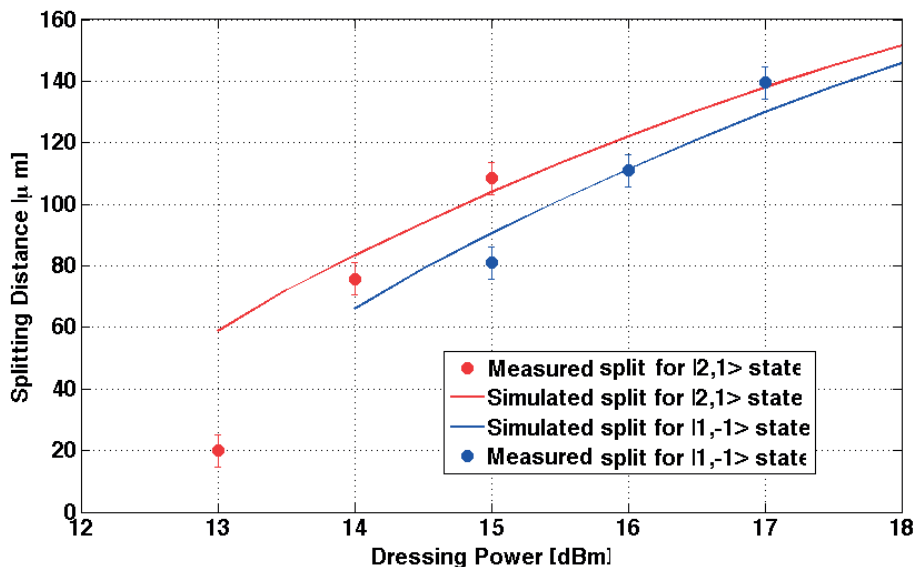


Figure 3-24: In situ double well splitting distance, measurement and simulation for a dressing detuning of $\Delta_1 = \Delta_2 = 382$ kHz and various dressing powers. To extrapolate the in situ splitting distance we record time-of-flight images for various hold times in the trap spanning a few trap periods and extract the central position from a fit to the oscillation. Shown are splitting distances up to $140 \mu\text{m}$. The data agree well with a prediction from our theoretical model calibrated by the field mapping in Fig 3-18.

3.5.2 High Rabi frequency transfer

Being able to create and control the state selective single and double well potentials, we now investigate the transfer between them. First, we apply 2-photon Rabi fre-

quencies (~ 200 Hz) which are much faster than the trap frequency along the splitting direction ω_y so that the atoms are quasi at stand-still during the transfer. Therefore, for the duration of the transfer pulse, the two wavefunctions have identical spatial extension and the difference in interaction energy is only given by the difference in scattering lengths $U = \frac{2\hbar}{m}\bar{n}(a_{22}-a_{11}-f(2a_{12}-a_{11}-a_{22}))$ where $f = (n_1-n_2)/(n_1+n_2)$ goes from -1 to +1. For a typical number of 2000 atoms in our trap, the variation of the interaction energy (the difference between $f=-1$ and $f=1$) is 1.5 Hz. The interaction energy is thus much smaller than the Rabi frequency and all atoms are spectrally coupled.

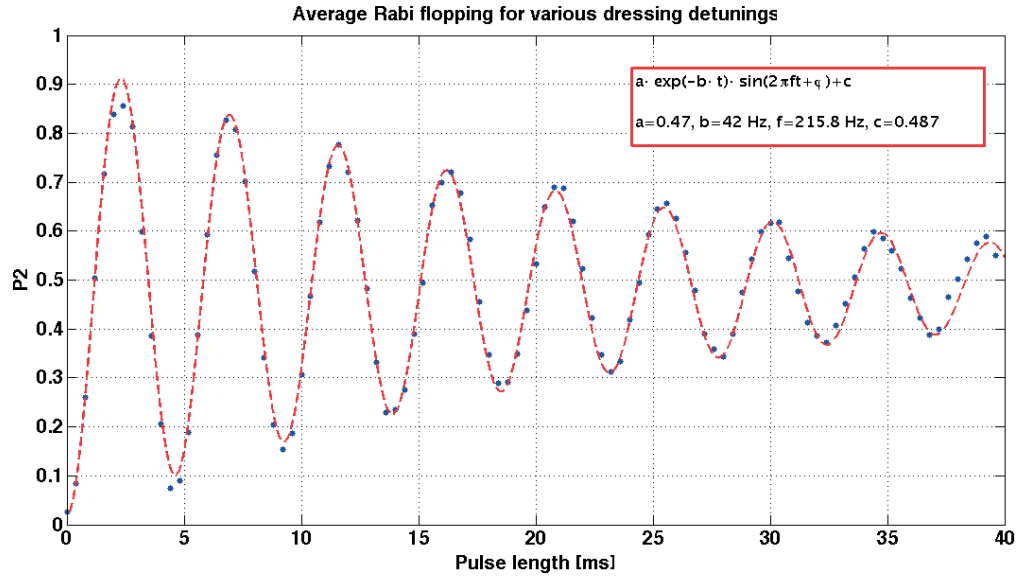


Figure 3-25: Rabi flopping between a single and double well for a Rabi frequency of $\Omega_{transfer} = 2\pi 215$ Hz. The dressing power is 11.2 dBm and the detuning 52 kHz causing a double well to form only for the $|2, 1\rangle$ state. We are in the regime where $\Omega_{transfer}$ dominates all other timescales (ω_y and internal interactions are smaller than $\Omega_{transfer}$) so that the transfer can be seen as quasi-instantaneous with respect to the atoms motion. This allows almost full contrast on the first flop but for times longer than 2 ms the the two wavefunctions begin to separate as the atoms start to roll down in the double well potential, reducing the overlap and subsequently the contrast of the Rabi flopping.

In figure 3-25 we see Rabi flopping between $F=1$ and $F=2$ for a dressing power of 11.2 dBm and a detuning of $\Delta_1 = -\Delta_2 = 52$ kHz creating a double well only for the $|2, 1\rangle$ state. The atoms are transferred from the single well to the top of the barrier of

the double well with a Rabi frequency $\Omega_{transfer} = 2\pi \cdot 215 \text{ Hz} \approx 5 \times \omega_y$. The contrast on the first π flop is high ($\sim 90 \%$) while for times longer than 2 ms, the F=2 clouds start to "roll" down the barrier and move away from the F=1 wavefunction, reducing the overlap and Rabi flopping contrast.

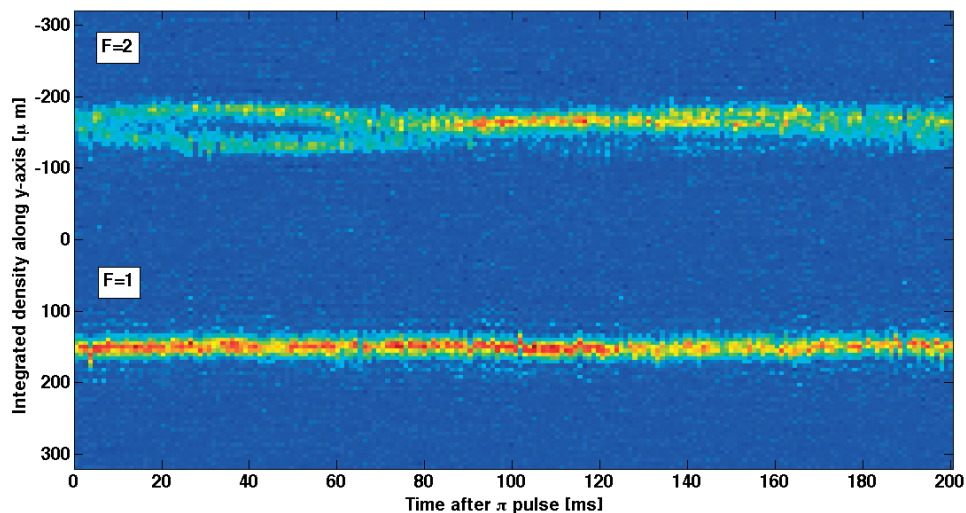


Figure 3-26: Evolution of the F=2 and F=1 atoms in the dressed potential. The dressing power is 10 dBm and the detuning 52 kHz. At $t=0$ a 10ms 2-photon pulse transfers $\sim 50\%$ of the atoms to F=2. The atoms are then held in the dressed potential for a variable time before being imaged with 16 ms time-of-flight. Images like that in fig. 3-23 are integrated along the z axis over 5 pixels around the cloud center. The resulting line scans are plotted against the hold time in the trap. The F=2 and F=1 state have been displaced vertically for better visibility. One observes a clear splitting of the F=2 atoms as they roll down from the center of the barrier into the two wells and perform a full oscillation. A second oscillation is damped probably due to collisions as the two clouds recombine. The rolling period is slightly different for the left (71 ms) and right (100 ms) wells, indicating asymmetries in the dressing microwave mode shape. The minima of the two wells is also asymmetrical and normally leads to the population of only the right well. In order to balance the two minima we apply a $\approx 40\text{G/m}$ static field gradient along the splitting axis from a pair of anti-Helmholtz coils.

3.5.3 Dynamics in the double well potential

This "rolling" dynamics can be observed by varying the hold time in the trap after a short transfer pulse. Images like in figure 3-23 are integrated over 5 pixels along

the z axis around the cloud center. The resulting line scans are then plotted against the hold time in the trap. Figure 3-26 shows such a film. The dressing power is 10 dBm with $\Delta_1 = -\Delta_2 = 52$ kHz. While the F=1 atoms remain steady in a single well potential, the F=2 atoms roll down from the center of the barrier into the double well and come back to the central position after a period of 71 ms for the left well (top arm in the figure) and 100 ms for the right. The different periods indicate asymmetries in the dressing microwave mode shape confirmed by our Rabi frequency mapping (figure 3-18). The depth of the two wells is also asymmetric and normally leads to the population of only the right well. In order to balance the two minima we here apply a ≈ 40 G/m static field gradient along the splitting axis from a pair of anti-Helmholtz coils. At the point of recombination one expects to observe fringes in the F=2 atom density. In figure 3-26 we see horizontal lines above and below the main atomic cloud, in particular in F=1, but we attribute these to optical fringes created in the imaging beam by diffraction from the dense atom cloud. Their high reproducibility excludes their interpretation as fringes in the atom density. The absence of atomic fringes can have several causes:

1. The fringe period is too small to be resolved. Indeed, the optical resolution of our imaging system is such that we could identify only a single interference fringe within the size of the cloud. But, since the two wells have slightly different oscillation periods, the two clouds meet with a relative velocity producing small period fringes.
2. The left and right clouds are not coherent or coherence is lost during the rolling.
3. a phase diffusion mechanism destroys any coherence by the time the two clouds meet again.

A clear interpretation cannot be given at this point.

Unable to identify spatial interferences in the atom density, we attempted to detect an interference signal in the population difference between $|1, -1\rangle$ and $|2, 1\rangle$. At $t=0$, a 1.2 ms long $\pi/2$ pulse transfers half the population to the $|2, 1\rangle$ state and the two states are allowed to evolve for a varying time in the trap before applying a second $\pi/2$ pulse and imaging. This sequence realizes our original interferometer idea. In figure 3-27 we show the absorption images for such a sequence for a detuning

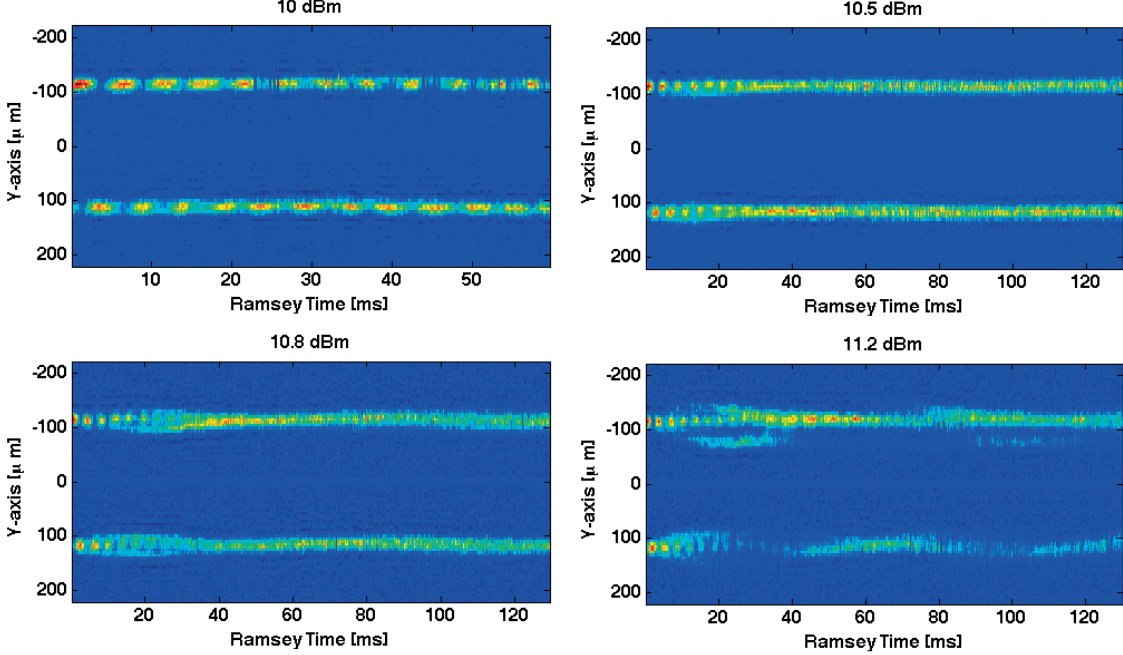


Figure 3-27: Ramsey sequence for high Rabi frequency transfer. The data was obtained similarly to the measurement in figure 3-26 but with a second $\pi/2$ pulse ($\Omega_{transfer} = 2\pi 208\text{Hz}$) at the end of the holding time thus creating a Ramsey sequence. The data was taken for a dressing detuning of 85 kHz and 4 different dressing powers below (10,10.5) dBm and above (10.8,11.2) dBm the threshold for the formation of the double well in $F=2$ (10.7 dBm for this detuning). For the lowest powers one sees the clear oscillation of the population between the two states as is expected from a Ramsey type clock measurement (both potentials quasi identical). For 10.8 and 11.2 dBm a clear "rolling" out motion is observed in $F=2$. The second pulse also transfers the split atoms back to $F=1$. Even for the biggest separation, coherence with the $F=1$ state is preserved indicated by the oscillating populations. The contrast is particularly good at the recombination time, when the $F=2$ atoms recover the initial position. Whether we observe oscillations at a second period which could indicate interference between the left and right paths requires further investigation.

of $\Delta_1 = \Delta_2 = 85\text{kHz}$ and various dressing powers. For a power of 10 and 10.5 dBm, not yet sufficient to form a double well (it forms for this detuning at 10.7 dBm), we see standard Ramsey oscillations between the two states just like in a clock measurement. This shows that coherence is preserved between the two dressed states. For higher powers (10.8 and 11.2 dBm) the double well in the $|2, 1\rangle$ has formed and the atoms oscillate in the double well. Initially, as the $F=2$ atoms start to roll off the barrier, they still overlap with the $|1, -1\rangle$ state and the second $\pi/2$ pulse is able to transfer them to the same position in the $|1, -1\rangle$ state. For longer times, the $F=2$ atoms have

moved outwards and the second pulse transfers them back to highly excited states of the $F=1$ potential, making also the $F=1$ cloud wider. Coherence between $F=1$ and $F=2$ is preserved for all powers observed as oscillation of the relative population, but it is not clear, whether a second oscillation period can be extracted which could indicate interference between the left and right double well. This needs a refined analysis of the data.

3.5.4 Low Rabi frequency transfer

In the previous fast Rabi frequency regime, the difficulty of identifying interference fringes between the left and right arm may be due to the relative motion of the atoms. In order to avoid this motion, we have tried to reach the sideband resolved regime, where the transfer pulse couples $F=1$ atoms to the vibrational ground state of the double well.

When attempting to populate the ground state of the double well, we must ensure that we populate only one vibrational state for each axis. As we discussed before, the σ^- transition $|1, -1\rangle \rightarrow |2, -2\rangle$ does not have a counterpart for the $|2, 1\rangle$ state and thus causes an asymmetry in the trap frequencies and vertical positions of the two states. The overlap along the vertical axis can however be easily tuned by individually choosing the detuning of the two tones ($|\Delta_1| \neq |\Delta_2|$).

In order to ensure good wavefunction overlap in the z direction we perform Rabi spectroscopy of the trap sideband at a dressing power of 11.2 dBm and detuning of 52 kHz where only the $F=2$ is a double well. We vary the differential detuning $\delta_1 = |\Delta_1| - |\Delta_2|$ in order to shift the $F=1$ potential with respect to that of $F=2$. Figure 3-28 shows the spectra for 4 different values $\delta_1 = (-9, -3, 3, 10)$ kHz. For each curve, beside the main resonance, one identifies a blue detuned sideband offset by 130 Hz corresponding to ω_z . The height of the sideband varies with δ_1 . For $\delta_1 = 3$ kHz it disappears, indicating perfect overlap, such that the potentials are quasi identical for the z motion and thus different vibrational states are orthogonal. The lack of a sideband corresponding to $\omega_x \approx 160$ Hz indicates that the overlap along the x axis is maintained as well. In passing we note the absence of the red sideband, indicating

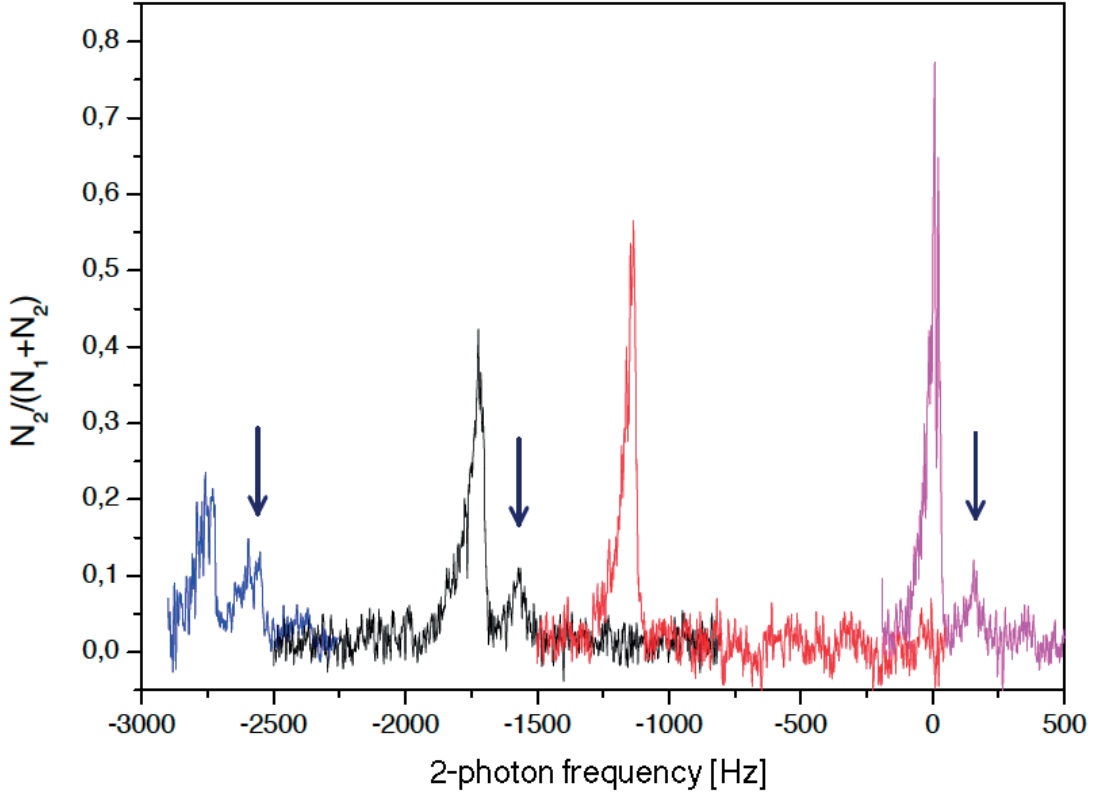


Figure 3-28: Optimizing the wavefunctions overlap along z between the single and double well potentials. The graphs shows Rabi spectroscopy for various differential dressing detunings $\delta_1 = |\Delta_1| - |\Delta_2|$ where $|\Delta_2| = 52$ kHz and a dressing power of 11.2 dBm creating a double well only for the $|2, 1\rangle$ state. The blue line represents a detuning of $\delta_1 = 9$ kHz, the black line corresponds to $\delta_1 = 3$ kHz, the red line to $\delta_1 = 3$ kHz and the purple to $\delta_1 = 10$ kHz. The arrows point to the sideband at $\omega_z \approx 130$ Hz. A difference in the vertical position of the two clouds leads to the appearance of sidebands on the transfer pulse. The best wavefunction overlap for the two clouds along the vertical direction is found for $\delta_1 = 3$ kHz where the sideband is eliminated. There the good overlap causes different vibrational states to be orthogonal. The absence of a sideband corresponding to the trap frequency along x ($\omega_x \approx 160$ Hz) indicates that the overlap along this axis is also maintained

that indeed we start from the ground state.

After having found the detuning which maximizes the overlap along the x and z axes, we set out to find the optimal pulse which will allow us to transfer atoms to the ground state of the double well. The length of the pulse is bound by two timescales: it cannot be longer than the lifetime in the $|2, 1\rangle$ state which we have measured to be around 300 ms and it must be sufficiently spectrally broad compared to the variation

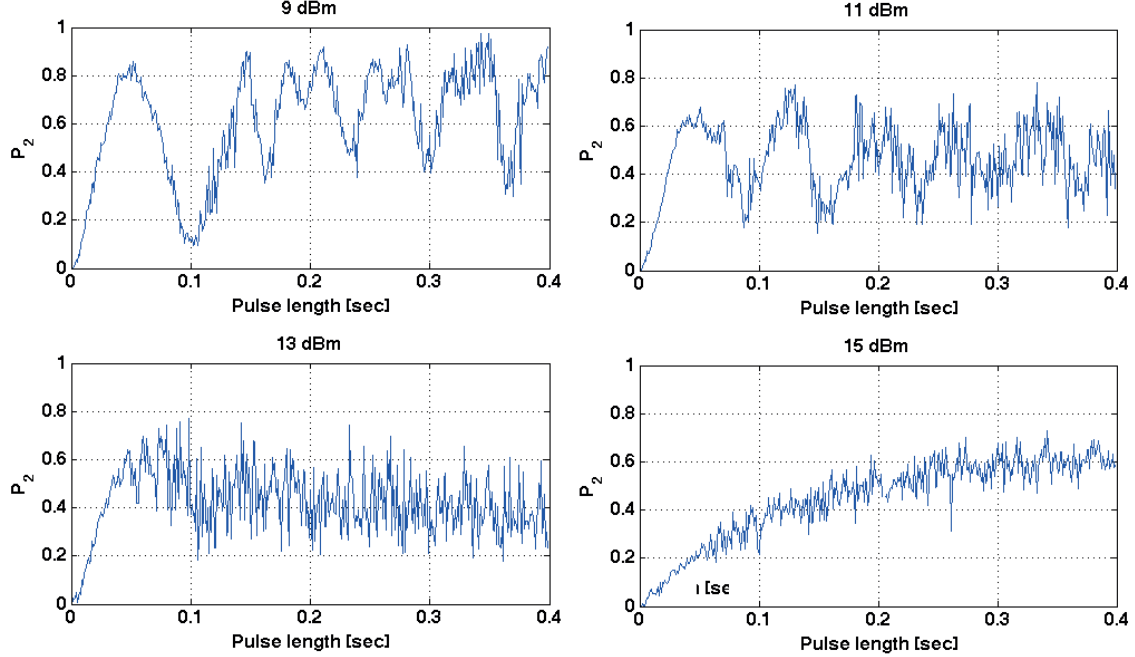


Figure 3-29: Slow Rabi flopping for various dressing powers. The measurement was taken with a common dressing detuning of $\Delta_1 = \Delta_2 = 400$ kHz and a transfer pulse power calibrated to produce a π pulse in 45 ms between the undressed potentials. For these detunings the double well is formed at 14 dBm. For each dressing power, the 2-photon frequency is tuned to maximize transfer. The lowest trap frequency is $\omega_y \approx 2 \times \Omega_{transfer}$. For the dressing powers of 9, 11 and 13 dBm, the Rabi oscillations start out with a single period but eventually excite higher vibrational states along the y axis causing a modulation of the Rabi oscillations by $\omega_y = 2\pi 40$ Hz. At 15 dBm the transfer is to a double well potential where the overlap between the two states is strongly reduced due to the displacement of the double well minima along the y axis, causing the breakdown of the flopping. With increasing dressing the interaction energy difference increases up to a few hundred Hz since the two states are now separated and the interaction energy becomes dependent on the density distribution in each state. The pulse then leaves the linear coupling regime and the transfer between internal states saturates.

of the interaction energy (which shifts the clock transition) so that we remain in the linear transfer regime.

In figure 3-29 we show Rabi oscillations for various dressing powers with a transfer pulse calibrated to π in 45 ms between the undressed potentials. The dressing detuning in these measurements is 400 kHz for which the double well is formed at around 14 dBm. For each dressing power, the 2-photon frequency is tuned to the maximum of the spectrum. For lower powers (9, 11 and 13 dBm) the transfer is between two

single wells with a longitudinal trap frequency of around 20-40 Hz. Since the F=1 and F=2 potential differ the transfer also couples to higher vibrational states of the F=2 potential seen as modulation by ω_y of the Rabi flopping. However, at low power, the overlap between F=1 and F=2 is still good meaning that each state interacts in a similar way with itself and with the other state so that the change in interaction energy during the pulse depends mainly on the scattering lengths difference, which for ^{87}Rb and our atom densities is small (1-2 Hz) compared to the pulse length, placing us safely in the linear coupling regime. When transferring to a double well (15 dBm) the overlap is attenuated by the splitting distance as the ground states of the double well are displaced from the F=1 harmonic potential. The interaction energy then varies by ≈ 500 Hz during the pulse. The transition is thus shifted out of resonance with the LO and the transfer will be progressively inhibited [18, 27]. In order to circumvent this problem the pulse would need to be chirped in order to keep it on resonance with the transition. This could be done in future investigations.

Despite the incomplete transfer into the double well potential, we record Rabi spectra to look for the vibrational levels in the double well. Resolving the vibrational levels is the first criterion for selectively addressing the ground state. In the end we were not able to spectrally resolve the individual levels in the double well and could only transfer atoms to a superposition of vibrational states. In figure 3-30 we show Rabi spectroscopy between the $|1, -1\rangle$ and $|2, 1\rangle$ states for a dressing detuning of 85 kHz and various powers. The 2-photon detuning is plotted relative to the frequency corresponding to the central peak. We notice that as the dressing power increases, the spectrum of the transfer broadens and a low frequency tail forms at 10.25 dBm for which a double well has probably formed. We cannot identify individual lines which could correspond to the vibrational levels. In order to increase our spectral resolution, we repeat the high power spectrum with a 500ms long transfer pulse and fine scanning. Figure 3-31 gives a spectroscopy run for 650 atoms a dressing power of 11 dBm and detuning of 85 kHz. The spectrum has the same form of a clear maximum with high frequency cut-off and a low frequency tail. However, even with the fine sampling it is difficult to identify individual lines. From simulations of the

vibrational levels of a single particle in a double well potential we have indications that the spectrum peak corresponds to population of the first state above the barrier and the tail to states within each double well. The spectroscopy cannot resolve these lines; we believe this is due to the fact that the left and right trap frequencies in the double well are not identical (as we saw in figure 3-26), thus creating a forest of tightly spaced lines which require even longer pulses to fully resolve.

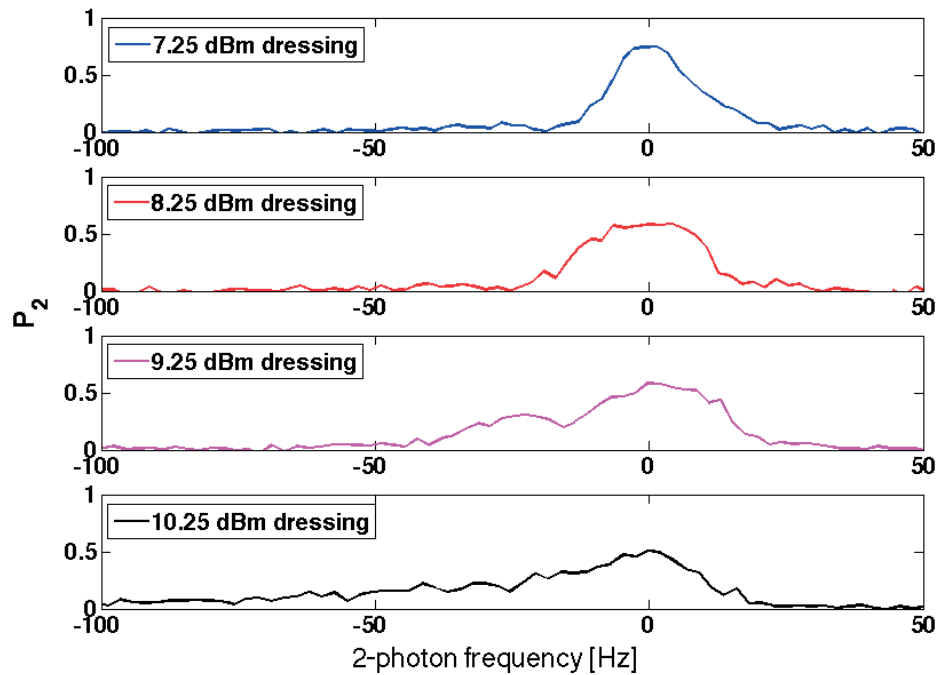


Figure 3-30: The transfer probability vs. the 2-photon frequency for increasing dressing power with a dressing detuning of 85 kHz. The transfer pulse was 55 ms long. The plotted 2-photon detuning was offset around the central peak for each graph for better comparison. We notice that as the dressing power increases, the spectrum of the transfer pulse broadens and a low frequency tail forms at 10.25 dBm for which a double well has probably formed.

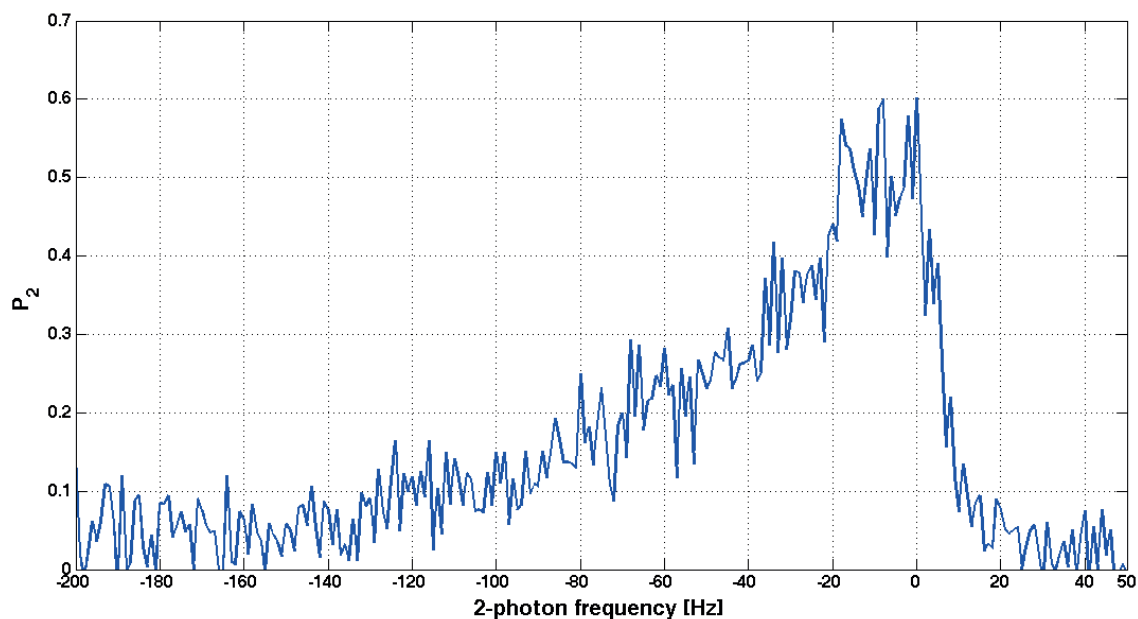


Figure 3-31: Rabi spectroscopy between a single well in the $|1, -1\rangle$ state and a double well in the $|2, 1\rangle$ state. The dressing power is 11 dBm with a detuning of 85 kHz and a transfer pulse 500 ms long. From simulations of the vibrational levels of a single particle in a double well potential we have indications that the spectrum peak corresponds to population of the first couple of states above the barrier and the low frequency tail to states within each double well. Unfortunately the spectrum does not allow to identify individual frequencies corresponding to the vibrational levels in the double well potential.

3.6 Conclusion

In this chapter we have proposed a new interferometer scheme based on microwave dressed potentials preparing a double well in just one of the hyperfine states of ^{87}Rb . The main feature of our proposal is the use of a transfer pulse to populate a double well initially prepared in a different internal state. Such a scheme circumvents the need to dynamically vary the trapping potential which leads to excitations of the condensate and to loss of coherence.

We were successful in creating a double well potential for the $|2, 1\rangle$ state while keeping the $|1, -1\rangle$ state in a single well. We could control the splitting distance and wavefunctions overlap in the transverse directions. We were also able to transfer atoms from a single to a double well. We observed that coherence between the two states is preserved for ~ 50 ms even though they were both dressed with an effective Rabi frequency of $\Omega_{\text{dressing}} \approx 2\pi 40$ kHz which generated very different potentials for the two states.

We have demonstrated that the two tone dressing method allows us to maintain a good wavefunction overlap between the two states as it allows us to tune their relative displacement by choosing different detunings for the two dressing tones. An asymmetry in the dressing, caused by the coupling of the $|1, -1\rangle$ state to $|2, -2\rangle$ made it possible to form a double well just for the $|2, 1\rangle$ state while maintaining a good vertical overlap.

We have used a spectrally broad pulse which transferred atoms to the top of the barrier causing the atoms to roll in the two wells and recombine after one oscillation period. We have not observed clear interference fringes between the two clouds, possibly due to asymmetries in the microwave mode shape which resulted in an asymmetric double well potential and a relative velocity between the two clouds as they recombined. This relative velocity might have then caused a fringe separation below our imaging resolution. The long oscillation period and the large kinetic energy imparted on the atoms could also have caused the atoms to decohere by the time the clouds recombined (after ~ 80 ms).

The second approach was more gentle and constituted in the attempt of transferring the atoms to the one vibrational state of the double well, ideally the ground state, hopefully producing a well defined relative phase between the two wells. Up to now, we were unable to observe an interference signal for these measurements as well. There are several issues which we believe prevented us from observing interference in this regime, we will summarize them in what follows and offer possible solutions that could open the way to a successful implementation of our scheme in the future.

Interactions induced level shifts

The interaction energy for our parameters changes by several hundred Hz when transferring from a single to a double well. The reduction in overlap between the $F=1$ and $F=2$ wavefunctions and the different densities in the two states cause the interaction energy to depend on the relative population. Thus as atoms are transferred from the single to the double well, the transition frequency increases and the LO becomes out of resonance eventually inhibiting the transfer. We suggested using Feshbach resonances or shallower traps in order to minimize the effect of interactions on the transition frequency but the simplest method would seem to be applying a chirp to the transfer pulse. We are currently working on estimating the correct chirping profile for various traps and simulations suggest we should be able to keep the pulse on resonance in such a way.

Asymmetry of the double well

The asymmetric microwave mode in our system generates an asymmetric double well with different trap frequencies for the left and right well (14 and 10 Hz respectively). Since these frequencies are close to one another, the Rabi spectrum exhibits a forest of interlaced lines which require very long pulses to individually resolve (see fig. 3-31). We believe the cause of the asymmetry to be a parasitic capacitive and/or inductive coupling to adjacent wires on the chip which could be alleviated by either producing a new chip with a larger separations between the wires or simply by adjusting the impedance of the two adjacent wires in order to symmetrize the coupling. Since all we

are interested in is a symmetric microwave mode and not necessarily the elimination of stray currents, the last option seems feasible.

Coupling to higher vibrational states - overlap and detuning

The ground state of $|1, -1\rangle$ should ideally have the largest overlap with the ground state of the $|2, 1\rangle$ double well and all other vibrational levels should be sufficiently detuned so as not to be coupled by the transfer pulse. However, for our shallow trap frequencies ($\omega_y \approx 20 - 40$ Hz) and large splitting distances ($\approx 30 \mu\text{m}$), the overlap with higher vibrational states of $|2, 1\rangle$ is typically larger. Additionally, the spacing of the vibrational levels is too small to compensate for the increased overlap causing the transfer pulse to populate higher vibrational states preferentially. Through simulations we have concluded that the solution to these problems is to work with a tighter trap along the splitting axis, with $\omega_y \approx 100$ Hz for the trap frequencies in the double well. For such trap frequencies we find that the detuning of higher vibrational states will be sufficient to suppress their population. Also, starting from a tighter trap one can create smaller splitting distances for the double well since the rotation of the trap field becomes non-negligible for trap frequencies on the order of 1 kHz and contributes to the curvature of the dressing field as in the work of Schumm et al. [112]. Smaller splittings will thus allow for a better overlap with the single well potential making the transfer pulses possibly more efficient.

Although the full interferometer scheme has not yet been achieved, we have demonstrated the basic building blocks of the method and have suggested ways to overcome the various difficulties. We believe that additional efforts will be fruitful and hope to demonstrate the full interferometer cycle in the near future.

Chapter 4

Conclusion

We have demonstrated an atomic clock with a stability of 5.8×10^{-13} at one second which integrates to the 10^{-15} level in less than a day. We have shown that the clock stability is limited by shot to shot cloud temperature and magnetic field fluctuations. We saw that the sensitivity to these two sources of noise can be cancelled by offsetting the bias field from the magic field value. Unfortunately the offset value is different for the magnetic and temperature fluctuations so that the sensitivity to both effects cannot be simultaneously cancelled. Reducing one noise source however, will reduce the system sensitivity to both as the minimum field could then be set nearer to the optimum point of the other. We discussed the possibility of increasing the time-of-flight in order to detect larger clouds and thus improve our estimation of the temperature, allowing us to correct for these fluctuations as we do for the atom number.

In the next generation of the experiment we plan to actively stabilize the current supplies by a feedback from a high precision transducer which performs on the 10^{-6} level, thus gaining an order of magnitude improvement on the magnetic fluctuations. We will also incorporate a 2D-MOT in order to implement a fast atom loading and a lower background pressure. This will increase the atom number and lifetime while reducing the cycle time. This upgrade will allow us to use longer Ramsey interrogation periods increasing the sensitivity. The higher atom number will allow us to improve on the quantum projection and detection noise while the better vacuum will reduce the

contribution from the symmetric losses noise. The shorter loading times and longer Ramsey times will increase the duty cycle reducing the Dick effect contribution. By implementing these steps we hope to reach the 1×10^{-13} level at one second at which point our clock will reach the precision of the best hydrogen masers available today.

In the second part of this work we have made the preliminary steps towards implementing an atom interferometer on the same atom chip. We have proposed a new interferometer scheme where atoms are transferred between two different internal states from a single to a double well. We have demonstrated such potentials by using state selective MW dressing and succeeded in transferring atoms between the two potentials, a feat which required the dressing of both states with two frequencies in order to match their vertical displacement and allow coupling. Although we were able to show coherence between the two internal states we are not able at this point to identify interference between the left and right wells. We have identified several issues that prevented us from reaching this goal. Interaction induced level shifts demand that the transfer pulse be chirped in order to keep it on resonance with the clock transition. We have found that the vibrational levels in the double well are too closely spaced and thus do not allow the transfer pulse to spectrally resolve the ground state with a pulse length shorter than the lifetime. The states were also not sufficiently detuned so as to hinder any transition to higher vibrational levels. Overcoming these difficulties by using tighter trap frequencies, a calibrated MW field and a chirped transfer pulse will possibly allow the generation of an interferometer with an arm separation of $\approx 200 \mu\text{m}$ which we were able to demonstrate. Assuming a modest coherence time of 50 ms, such an interferometer will have a figure of merit on the order of $\chi \approx 0.01 \text{ mm}\cdot\text{s}$ placing it on par with current falling cube gravimeters.

We have thus demonstrated the possibility of integrating two different sensors, an atomic clock and an atom interferometer on the same atom chip. The narrow linewidth shown in the atomic clock implementation can in principle be used to measure other physical quantities (e.g. acceleration) and demonstrates the suitability of the atom chip technology for demanding metrological applications including inertial navigation.

A future generation of our system could thus provide a solution for integrated inertial navigation units.

Appendix A

The spectral analysis of fluctuations

We present in this appendix a basic treatment of the mathematical formulation of fluctuations and derive some results which are used throughout the text.

We start by describing a general signal as:

$$V(t) = V_0(t) \cdot \cos(\omega_0 t + \phi(t)) \quad (\text{A.1})$$

We describe the noise on the amplitude and phase of the signal by writing:

$$V(t) = V_0 \cdot (1 + \alpha(t)) \cdot \cos(\omega_0 t + \phi(t)) = V_0 \cdot (1 + \alpha(t)) \cdot \cos(\omega_0 t + \int_0^t \Delta\omega(t') dt') \quad (\text{A.2})$$

Where we assume the oscillator is locked to a reference and has reached equilibrium, so that both $\alpha(t)$ and $\phi(t)$ should be regarded as small fluctuations around 0.

Since the phase $\phi(t)$ fluctuates around a zero mean value we turn our focus to the second moment of the fluctuation - the variance or power of the noise. The variance characterizes a noise process completely only if the process is stationary, ergodic and Gaussian since the highest non-zero moment of a Gaussian noise is the variance. We ensure stationarity and ergodicity by averaging over time and over

different realizations of the same experiment. Even if the probability density of the individual processes from which the noise originates are not Gaussian a Gaussian amplitude distribution can always be assumed for a large number of degrees of freedom due to the central limit theorem. Such an assumption is justified in our case as the noise originates from the fluctuation of a large number of electrons in the circuit. If in addition, the individual noise sources are uncorrelated then the noise is said to be white but Gaussian noise does not necessarily imply white noise (a common mistake) and you can have $1/f$ Gaussian noise for example. A Gaussian noise simply means that the amplitude distribution of the noise is Gaussian but says nothing about the spectrum.

We consider that the variance of the phase has reached equilibrium:

$$\langle \phi^2(t) \rangle = \sigma_\phi^2 \quad (\text{A.3})$$

Since a noise source is by definition time dependent (it fluctuates), a full analysis will have to investigate the spectrum of this Gaussian envelope. If the phase was a periodic signal we could write

$$\phi(t) = \sum_{n=1}^{\infty} a_n \cos(n\omega_0 t) + \sum_{n=1}^{\infty} b_n \sin(n\omega_0 t) \quad (\text{A.4})$$

Where we have already subtracted the mean value a_0 (since $\phi(t)$ is the fluctuation of phase from the mean value) and:

$$a_n = \frac{2}{T} \int_0^T \phi(t) \cos(n\omega_0 t) dt \quad b_n = \frac{2}{T} \int_0^T \phi(t) \sin(n\omega_0 t) dt \quad (\text{A.5})$$

But since $\phi(t)$ is a random function of time, then the coefficients a and b would themselves be statistical in nature. To apply the concept of periodicity to such a function, we must take the measurement time T to be infinite which amounts to taking $\omega_0 \rightarrow 0$, in this limit we can take the ensemble average of equation A.5 and get:

$$\langle a_n \rangle = \langle b_n \rangle = 0 \quad (\text{A.6})$$

However, by taking the ensemble average of equation A.4 squared, we obtain:

$$\langle \phi^2(t) \rangle = \sum_n \frac{1}{2} \langle a_n^2 \rangle + \sum_n \frac{1}{2} \langle b_n^2 \rangle = \sum_n \frac{1}{2} [\langle a_n^2 \rangle + \langle b_n^2 \rangle] = \sigma_\phi^2 \quad (\text{A.7})$$

Now, since the phases are random, we have for all n , $\langle a_n^2 \rangle = \langle b_n^2 \rangle$ so we can write:

$$\langle \phi^2(t) \rangle = \sum_n \langle a_n^2 \rangle = \int_0^\infty S(f) df \quad (\text{A.8})$$

Where $S(f)$ is called the power spectral density (or PSD) of the random process and it represents the frequency dependence of the fluctuations. The PSD gives the contribution of each frequency component to the total variance:

$$\langle a_n^2 \rangle = S(nf_0) \Delta(nf_0) \quad (\text{A.9})$$

The units of PSD $S(f)$ are the power of the noise source within a 1 Hz bandwidth centered around a frequency f (see Fig. A-1).

The usage of the word “power” is used in the sense that energy can be defined as the integral of the square of a signal (and using Parserval’s theorem it is also the integral of the square of the Fourier transform of the signal), in case the signal is the voltage applied on a 1 Ohm resistor, the units of energy are Joule and the power is actually in Watt’s. For any other signal, one needs to apply a proper scaling to reach actual SI units and this is very rarely done. Usually one simply uses the units of the fluctuating variable squared per Hz, so for phase fluctuations the units are in $\frac{\text{rad}^2}{\text{Hz}}$ or $\text{dB} \frac{\text{rad}^2}{\text{Hz}}$ or when we are interested in the standard deviation, we take the square root of the variance and have the weird units of $\frac{\text{rad}}{\sqrt{\text{Hz}}}$.

Using equation A.5 we can write the expression for $\langle a_n^2 \rangle$ directly:

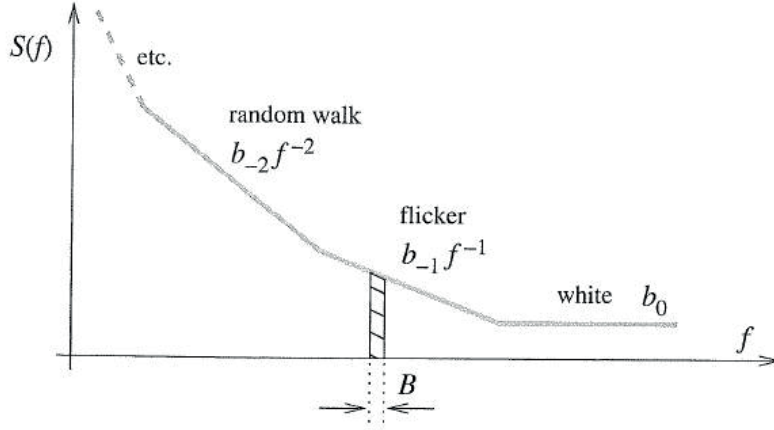


Figure A-1: The Power Spectral Density is defined as the average power in Watt in a 1 Hz bandwidth centered around the frequency f . It is calculated using an infinitesimally narrow averaging region to remove effects of slope, the average power is then: $S(f) \equiv P(f) = \lim_{B \rightarrow 0} \frac{1}{B} \int_{f-B/2}^{f+B/2} S(f') df'$ and the integral over all frequencies is the total power: $P = \int_0^{\infty} S(f) df$. Taken from [106].

$$\langle a_n^2 \rangle = \frac{4}{T^2} \int_0^T \int_0^T \langle \phi(t_1)\phi(t_2) \rangle \cos\left(\frac{2\pi n t_1}{T}\right) \cos\left(\frac{2\pi n t_2}{T}\right) dt_1 dt_2 \quad (\text{A.10})$$

Changing to the variables $X = \frac{1}{2}(t_1 + t_2)$ and $\tau = t_2 - t_1$ we get:

$$\langle a_n^2 \rangle = \frac{2}{T^2} \int_{X=0}^T \int_{\tau=-\infty}^{\infty} \langle \phi(t_1)\phi(\tau + t_1) \rangle \left[\cos\left(\frac{2\pi n \tau}{T}\right) + \cos\left(\frac{4\pi n X}{T}\right) \right] dX d\tau \quad (\text{A.11})$$

Where we kept the t_1 in the integral since it is understood that the interval T over which the measurement is performed is much larger than the duration over which the phase variable $\phi(t)$ is periodic (since this is a randomly fluctuating variable, which has no “memory” of past results) so t_1 can in the limit $T \rightarrow \infty$ be considered constant. Such systems are also called stationary, they are symmetric to a time translation.

Now, the second part of the integral vanishes on integration over X and the first part gives:

$$\langle a_n^2 \rangle = \frac{4}{T} \int_0^{\infty} R(\tau) \cos\left(\frac{2\pi n \tau}{T}\right) d\tau \quad (\text{A.12})$$

Where $R(\tau)$ is the autocorrelation function:

$$R(\tau) = \langle \phi(t)\phi(t + \tau) \rangle \quad (\text{A.13})$$

Comparing with (A.9) we finally get:

$$S(f) = 4 \int_0^{\infty} R(\tau) \cos(2\pi f\tau) d\tau \quad (\text{A.14})$$

And the inverse equation is:

$$R(\tau) = \int_0^{\infty} S(f) \cos(2\pi f\tau) df \quad (\text{A.15})$$

Equations A.14 and A.15 constitute the theorem of Wiener and Khintchin and are the basis of noise measurements.

For $\tau = 0$ we get:

$$R(0) = \int_0^{\infty} S(f) df = \langle \phi^2(t) \rangle = \sigma_{\phi}^2 \quad (\text{A.16})$$

In the literature you often see (particularly in a theoretical context) the use of the two-sided power spectral density, defined as:

$$S^{II}(f) = \int_{-\infty}^{\infty} R(\tau) e^{-i2\pi f\tau} d\tau \quad (\text{A.17})$$

Using the complex function basis $e^{i\omega t}$ which requires S^{II} to be a complex quantity that extends also to negative frequencies, the inverse equation is then:

$$R(\tau) = \frac{1}{2\pi} \int_{-\infty}^{\infty} S^{II}(f) e^{i2\pi f\tau} df \quad (\text{A.18})$$

And the autocorrelation and two-sided PSD are a Fourier transform pair which facilitates calculations. For example, The PSD of a white noise source (completely uncorrelated) can be easily calculated by noticing that for a white source the autocorrelation function is simply a delta function times the variance:

$$\begin{aligned}
S_{White}(f) &= 2 \int_{-\infty}^{\infty} R(\tau) e^{-i\omega t} dt \\
&= 2 \int_{-\infty}^{\infty} \lim_{T \rightarrow \infty} \frac{1}{T} \int_{-\frac{T}{2}}^{\frac{T}{2}} \phi(t) \phi(t + \tau) dt e^{-i\omega t} dt \\
&= 2 \int_{-\infty}^{\infty} \sigma^2 \delta(t) e^{-i\omega t} dt = 2\sigma^2
\end{aligned} \tag{A.19}$$

One must remember however, that when the oscillating field is a scalar, the negative frequencies and complex part of $S^{II}(f)$ in such a calculation are a mathematical artifact and have no physical meaning whatsoever. As we have seen, the derivation can be done without any reference to negative frequencies or complex numbers. When the two-sided PSD is used, the negative frequencies convey no information and the relationship between the real PSD and the two-sided kind is:

$$\begin{aligned}
S(f) &= 2S^{II}(f), \text{ for } f > 0 \\
S(f) &= 0, \text{ otherwise}
\end{aligned} \tag{A.20}$$

A meaning to negative frequencies can only be made in the case of vector observables that have a sense of rotation. Then, a clockwise rotation is associated with negative frequencies and a counter-clockwise rotation with positive frequencies. In our case, $\phi(t)$ is a scalar, and there is no meaning to its direction of oscillation.

A.1 Unit conversion of the Power Spectral density

Up to now we were discussing the fluctuation of the phase variable, in case we want to use the frequency fluctuation, we simply notice that the frequency is the derivative of the phase and write for the frequency PSD:

$$S_{\omega}(f) = 4 \int_0^{\infty} \langle \dot{\phi}(t)\dot{\phi}(t+\tau) \rangle \cos(2\pi f\tau) d\tau = 4\pi^2 f^2 4 \int_0^{\infty} \langle \phi(t)\phi(t+\tau) \rangle \cos(2\pi f\tau) d\tau = 4\pi^2 f^2 S_{\phi}(f) \quad (\text{A.21})$$

Since inside the cosine transform the time derivative maps into a multiplication by $2\pi f$. We then get for the PSD of the angular frequency:

$$S_f(f) = \frac{1}{4\pi^2} S_{\omega}(f) = f^2 S_{\phi}(f) \quad (\text{A.22})$$

The fractional frequency (the frequency relative to the carrier $y = \frac{f}{f_0}$) PSD is then:

$$S_y(f) = \left(\frac{f}{f_0}\right)^2 S_{\phi}(f) \quad (\text{A.23})$$

Where in our case $f_0 = 6.834GHz$.

Usually the PSD is given in dB units, writing:

$$S_{dB\phi}(f) = 10 \log\left(\frac{S_{\phi}(f)}{1 \frac{\text{rad}^2}{\text{Hz}}}\right) \quad (\text{A.24})$$

Relative to the power in $1 \frac{\text{rad}^2}{\text{Hz}}$ (this is why the actual energy in Watt is never used)

Or in dBc, which is usually said to define the fluctuations relative to the power of the carrier, but it is simply defined by as:

$$\begin{aligned} L(f) &= \frac{1}{2} S_{\phi}(f) \\ dBc &= 10 \log_{10}(L(f)) = 10 \log_{10}\left(\frac{1}{2} S_{\phi}(f)\right) \\ &= 10 \log_{10}\left(\frac{1}{2}\right) + 10 \log_{10}(S_{\phi}) = -3.0103 + dB S_{\phi} \end{aligned} \quad (\text{A.25})$$

Bibliography

- [1] Accubeat AR133a-03 Rubidium frequency standard. <http://www.accubeat.com/var/125/525204-AR133A-03%20Specifications%2017.07.2011.pdf>.
- [2] Stanford research systems PRS10 Rubidium frequency standard. <http://www.thinksrs.com/downloads/PDFs/Catalog/PRS10c.pdf>.
- [3] Symmetricom 5071A datasheet. http://www.microsemi.com/document-portal/doc_download/133269-5071a.
- [4] Symmetricom SA.45s chip scale atomic clock. www.microsemi.com/products/timing-synchronization-systems/embedded-timing-solutions/components/sa-45s-chip-scale-atomic-clock.
- [5] Symmetricom XPRO high-performance rubidium oscillator. http://www.microsemi.com/document-portal/doc_download/133334-xpro.
- [6] Charles C Agosta, Isaac F Silvera, Hendricus Theodorus Christiaan Stoof, and BJ Verhaar. Trapping of neutral atoms with resonant microwave radiation. *Physical review letters*, 62(20):2361, 1989.
- [7] David W Allan. Statistics of atomic frequency standards. *Proceedings of the IEEE*, 54(2):221–230, 1966.
- [8] Dana Z Anderson and Jakob GJ Reichel. Cold atom system with atom chip wall, October 24 2006. US Patent 7,126,112.

- [9] MR Andrews, CG Townsend, H-J Miesner, DS Durfee, DM Kurn, and W Ketterle. Observation of interference between two Bose condensates. *Science*, 275(5300):637–641, 1997.
- [10] T Bandi, C Affolderbach, CE Calosso, and G Mileti. High-performance laser-pumped rubidium frequency standard for satellite navigation. *Electronics letters*, 47(12):698–699, 2011.
- [11] Florian Baumgärtner, RJ Sewell, S Eriksson, I Llorente-Garcia, Jos Dingjan, JP Cotter, and EA Hinds. Measuring energy differences by BEC interferometry on a chip. *Physical review letters*, 105(24):243003, 2010.
- [12] Simon Bernon, Thomas Vanderbruggen, Ralf Kohlhaas, Andrea Bertoldi, Arnaud Landragin, and Philippe Bouyer. Heterodyne non-demolition measurements on cold atomic samples: towards the preparation of non-classical states for atom interferometry. *New Journal of Physics*, 13(6):065021, 2011.
- [13] BJ Bloom, TL Nicholson, JR Williams, SL Campbell, M Bishof, X Zhang, W Zhang, SL Bromley, and J Ye. An optical lattice clock with accuracy and stability at the 10⁻¹⁸ level. *Nature*, 2014.
- [14] Pascal Böhi, Max F Riedel, Theodor W Hänsch, and Philipp Treutlein. Imaging of microwave fields using ultracold atoms. *Applied Physics Letters*, 97(5):051101, 2010.
- [15] Pascal Böhi, Max F Riedel, Johannes Hoffrogge, Jakob Reichel, Theodor W Hänsch, and Philipp Treutlein. Coherent manipulation of Bose–Einstein condensates with state-dependent microwave potentials on an atom chip. *Nature Physics*, 5(8):592–597, 2009.
- [16] Ch J Bordé. Atomic interferometry with internal state labelling. *Physics letters A*, 140(1):10–12, 1989.

- [17] Rym Bouchendira, Pierre Cladé, Saïda Guellati-Khélifa, François Nez, and François Biraben. New determination of the fine structure constant and test of the quantum electrodynamics. *Physical Review Letters*, 106(8):080801, 2011.
- [18] Erez Boukobza, Maya Chuchem, Doron Cohen, and Amichay Vardi. Phase-diffusion dynamics in weakly coupled Bose-Einstein condensates. *Physical review letters*, 102(18):180403, 2009.
- [19] G Kleine Büning, J Will, W Ertmer, E Rasel, Jan Arlt, C Klempt, F Ramirez-Martinez, F Piéchon, and P Rosenbusch. Extended coherence time on the clock transition of optically trapped rubidium. *Physical review letters*, 106(24):240801, 2011.
- [20] JHT Burke, B Deissler, KJ Hughes, and CA Sackett. Confinement effects in a guided-wave atom interferometer with millimeter-scale arm separation. *Physical Review A*, 78(2):023619, 2008.
- [21] Olivier Carnal and Jürgen Mlynek. Young’s double-slit experiment with atoms: A simple atom interferometer. *Physical review letters*, 66(21):2689, 1991.
- [22] Donatella Cassettari, Alexander Chenet, Ron Folman, Albrecht Haase, Bjorn Hessmo, P Krüger, Thomas Maier, Stefan Schneider, Tommaso Calarco, and Jorg Schmiedmayer. Micromanipulation of neutral atoms with nanofabricated structures. *Applied Physics B*, 70(5):721–730, 2000.
- [23] Donatella Cassettari, Björn Hessmo, Ron Folman, Thomas Maier, and Jörg Schmiedmayer. Beam splitter for guided atoms. *Physical Review Letters*, 85(26):5483, 2000.
- [24] D Chambon, S Bize, M Lours, F Narbonneau, H Marion, A Clairon, G Santarelli, A Luiten, and M Tobar. Design and realization of a flywheel oscillator for advanced time and frequency metrology. *Review of Scientific Instruments*, 76(9):094704, 2005.

- [25] Sheng-wey Chiow, Tim Kovachy, Hui-Chun Chien, and Mark A Kasevich. 102 hbar k large area atom interferometers. *Physical review letters*, 107(13):130403, 2011.
- [26] Steven Chu. The manipulation of neutral particles. *Reviews of Modern Physics*, 70(3):685–706, 1998.
- [27] Maya Chuchem, Katrina Smith-Mannschott, Moritz Hiller, Tsampikos Kottos, Amichay Vardi, and Doron Cohen. Quantum dynamics in the Bosonic Josephson junction. *Physical Review A*, 82(5):053617, 2010.
- [28] A Clairon, C Salomon, S Guellati, and WD Phillips. Ramsey resonance in a Zacharias fountain. *EPL (Europhysics Letters)*, 16(2):165, 1991.
- [29] Claude Cohen-Tannoudji. Manipulating atoms with photons. *Physica Scripta*, 1998(T76):33, 1998.
- [30] Claude Cohen-Tannoudji, Jacques Dupont-Roc, and Gilbert Grynberg. *Atom-photon interactions: basic processes and applications*. Wiley Online Library, 1992.
- [31] Yves Colombe, Elena Knyazchyan, Olivier Morizot, Brigitte Mercier, Vincent Lorent, and Hélène Perrin. Ultracold atoms confined in rf-induced two-dimensional trapping potentials. *EPL (Europhysics Letters)*, 67(4):593, 2004.
- [32] CC Counselman III, II Shapiro, AEE Rogers, HF Hinteregger, CA Knight, AR Whitney, and TA Clark. VLBI clock synchronization. In *IEEE Proceedings*, volume 65, page 1622, 1977.
- [33] Alexander D Cronin, Jörg Schmiedmayer, and David E Pritchard. Optics and interferometry with atoms and molecules. *Reviews of Modern Physics*, 81(3):1051, 2009.
- [34] Franco Dalfovo, Stefano Giorgini, Lev P Pitaevskii, and Sandro Stringari. Theory of Bose-Einstein condensation in trapped gases. *Reviews of Modern Physics*, 71(3):463, 1999.

- [35] JM Danet, O Kozlova, S Guerandel, and E de Clercq. Recent progress on the pulsed CPT Cs clock at SYRTE. In *European Frequency and Time Forum (EFTF), 2012*, pages 91–95. IEEE, 2012.
- [36] J Denschlag, D Cassetari, A Chenet, St Schneider, and Jörg Schmiedmayer. A neutral atom and a wire: towards mesoscopic atom optics. *Applied Physics B*, 69(4):291–301, 1999.
- [37] Andrei Derevianko and Hidetoshi Katori. Colloquium: Physics of optical lattice clocks. *Reviews of Modern Physics*, 83(2):331, 2011.
- [38] Christian Deutsch, Fernando Ramirez-Martinez, Clement Lacroûte, Friedemann Reinhard, Tobias Schneider, Jean-Noël Fuchs, Frédéric Piéchon, Franck Laloë, Jakob Reichel, and Peter Rosenbusch. Spin self-rephasing and very long coherence times in a trapped atomic ensemble. *Physical review letters*, 105(2):020401, 2010.
- [39] Susannah M Dickerson, Jason M Hogan, Alex Sugarbaker, David MS Johnson, and Mark A Kasevich. Multiaxis inertial sensing with long-time point source atom interferometry. *Physical review letters*, 111(8):083001, 2013.
- [40] Savas Dimopoulos, Peter W Graham, Jason M Hogan, and Mark A Kasevich. Testing general relativity with atom interferometry. *Physical review letters*, 98(11):111102, 2007.
- [41] F Pereira Dos Santos, H Marion, S Bize, Y Sortais, A Clairon, and Christophe Salomon. Controlling the cold collision shift in high precision atomic interferometry. *Physical review letters*, 89(23):233004, 2002.
- [42] John M Dow, RE Neilan, and C Rizos. The international GNSS service in a changing landscape of global navigation satellite systems. *Journal of Geodesy*, 83(3-4):191–198, 2009.

- [43] DS Durfee, YK Shaham, and MA Kasevich. Long-term stability of an area-reversible atom-interferometer Sagnac gyroscope. *Physical review letters*, 97(24):240801, 2006.
- [44] VA Dzuba and VV Flambaum. Atomic optical clocks and search for variation of the fine-structure constant. *Physical Review A*, 61(3):034502, 2000.
- [45] Todd Ely, Jill Seubert, John Prestagez, and Robert Tjoelker. The deep space atomic clock: ushering in a new paradigm for radio navigation and science. 2013.
- [46] Francois-Xavier Esnault, David Holleville, Nicolas Rossetto, Stephane Guerandel, and Noel Dimarcq. High-stability compact atomic clock based on isotropic laser cooling. *Physical Review A*, 82(3):033436, 2010.
- [47] Jerome Esteve, Thorsten Schumm, J-B Trebbia, Isabelle Bouchoule, Alain Aspect, and CI Westbrook. Realizing a stable magnetic double-well potential on an atom chip. *The European Physical Journal D-Atomic, Molecular, Optical and Plasma Physics*, 35(1):141–146, 2005.
- [48] Jérôme Estève, J-B Trebbia, Thorsten Schumm, Alain Aspect, Christoph I Westbrook, and Isabelle Bouchoule. Observations of density fluctuations in an elongated Bose gas: Ideal gas and quasicondensate regimes. *Physical review letters*, 96(13):130403, 2006.
- [49] Tristan Farah, Christine Guerlin, Arnaud Landragin, Philippe Bouyer, Stéphane Gaffet, Franck Pereira Dos Santos, and Sébastien Merlet. Underground operation at best sensitivity of the mobile LNE-SYRTE cold atom gravimeter. *arXiv preprint arXiv:1404.6722*, 2014.
- [50] Raymond Filler, Steven Ganop, Paul Olson, Stanley Sokolowski, and William Fischer. Positioning, navigation and timing: the foundation of command and control. Technical report, DTIC Document, 2004.

- [51] JB Fixler, GT Foster, JM McGuirk, and MA Kasevich. Atom interferometer measurement of the Newtonian constant of gravity. *Science*, 315(5808):74–77, 2007.
- [52] Ron Folman, Peter Krüger, Jörg Schmiedmayer, Johannes Denschlag, and Carsten Henkel. Microscopic atom optics: from wires to an atom chip. *Advances in Atomic, Molecular, and Optical Physics*, 48:263–356, 2002.
- [53] J Fortagh, A Grossmann, C Zimmermann, and TW Hänsch. Miniaturized wire trap for neutral atoms. *Physical review letters*, 81(24):5310, 1998.
- [54] Maurice Françon. Optical interferometry. In *Neutron interferometry*. 1979.
- [55] Carlos L Garrido Alzar, Wenhua Yan, and Arnaud Landragin. Towards high sensitivity rotation sensing using an atom chip. In *High Intensity Lasers and High Field Phenomena*, pages JT2A–10. Optical Society of America, 2012.
- [56] A Gauguet, Benjamin Canuel, Thomas Lévèque, Walid Chaibi, and Arnaud Landragin. Characterization and limits of a cold-atom Sagnac interferometer. *Physical Review A*, 80(6):063604, 2009.
- [57] David M Giltner, Roger W McGowan, and Siu Au Lee. Atom interferometer based on Bragg scattering from standing light waves. *Physical review letters*, 75(14):2638, 1995.
- [58] Peter W Graham, Jason M Hogan, Mark A Kasevich, and Surjeet Rajendran. New method for gravitational wave detection with atomic sensors. *Physical review letters*, 110(17):171102, 2013.
- [59] Jocelyne Guéna, Michel Abgrall, Daniele Rovera, Peter Rosenbusch, Michael E Tobar, Ph Laurent, André Clairon, and Sébastien Bize. Improved tests of local position invariance using Rb 87 and Cs 133 fountains. *Physical review letters*, 109(8):080801, 2012.

- [60] TL Gustavson, A Landragin, and MA Kasevich. Rotation sensing with a dual atom-interferometer Sagnac gyroscope. *Classical and Quantum Gravity*, 17(12):2385, 2000.
- [61] Wolfgang Hänsel, Peter Hommelhoff, TW Hänsch, and J Reichel. Bose-Einstein condensation on a microelectronic chip. *Nature*, 413(6855):498–501, 2001.
- [62] DM Harber, HJ Lewandowski, JM McGuirk, and EA Cornell. Effect of cold collisions on spin coherence and resonance shifts in a magnetically trapped ultracold gas. *Physical Review A*, 66(5):053616, 2002.
- [63] S Hofferberth, I Lesanovsky, B Fischer, T Schumm, and J Schmiedmayer. Non-equilibrium coherence dynamics in one-dimensional Bose gases. *Nature*, 449(7160):324–327, 2007.
- [64] S Hofferberth, I Lesanovsky, B Fischer, J Verdu, and J Schmiedmayer. Radiofrequency-dressed-state potentials for neutral atoms. *Nature Physics*, 2(10):710–716, 2006.
- [65] Munekazu Horikoshi and Kenichi Nakagawa. Suppression of dephasing due to a trapping potential and atom-atom interactions in a trapped-condensate interferometer. *Physical review letters*, 99(18):180401, 2007.
- [66] Munekazu Horikoshi and Ken'ichi Nakagawa. Dephasing due to atom-atom interaction in a waveguide interferometer using a Bose-Einstein condensate. *Physical Review A*, 74(3):031602, 2006.
- [67] Y-Y Jau, H Partner, PDD Schwindt, JD Prestage, JR Kellogg, and N Yu. Low-power, miniature ^{171}Yb ion clock using an ultra-small vacuum package. *Applied Physics Letters*, 101(25):253518, 2012.
- [68] Rudra P Kafle, Dana Z Anderson, and Alex A Zozulya. Analysis of a free oscillation atom interferometer. *Physical Review A*, 84(3):033639, 2011.

- [69] Elliott D Kaplan and Christopher J Hegarty. *Understanding GPS: principles and applications*. Artech house, 2005.
- [70] Mark Kasevich and Steven Chu. Atomic interferometry using stimulated Raman transitions. *Physical Review Letters*, 67(2):181, 1991.
- [71] Mark Kasevich and Steven Chu. Atomic interferometry using stimulated Raman transitions. *Physical Review Letters*, 67(2):181, 1991.
- [72] Mark A Kasevich, Erling Riis, Steven Chu, and Ralph G DeVoe. RF spectroscopy in an atomic fountain. *Physical review letters*, 63(6):612, 1989.
- [73] S Knappe, P Schwindt, V Shah, L Hollberg, J Kitching, L Liew, and J Moreland. A chip-scale atomic clock based on ^{87}Rb with improved frequency stability. *Optics express*, 13(4):1249–1253, 2005.
- [74] M Kohnen, PG Petrov, RA Nyman, and EA Hinds. Minimally destructive detection of magnetically trapped atoms using frequency-synthesized light. *New Journal of Physics*, 13(8):085006, 2011.
- [75] Clement Lacroute, Friedemann Reinhard, Fernando Ramirez-Martinez, Christian Deutsch, Tobias Schneider, Jakob Reichel, and Peter Rosenbusch. Preliminary results of the trapped atom clock on a chip. *Ultrasonics, Ferroelectrics and Frequency Control, IEEE Transactions on*, 57(1):106–110, 2010.
- [76] Ph Laurent, M Abgrall, Ch Jentsch, P Lemonde, G Santarelli, A Clairon, I Maksimovic, S Bize, Ch Salomon, D Blonde, et al. Design of the cold atom PHARAO space clock and initial test results. *Applied Physics B*, 84(4):683–690, 2006.
- [77] Jean Lautier, Michel Lours, and Arnaud Landragin. A compact micro-wave synthesizer for transportable cold-atom interferometers. *Review of Scientific Instruments*, 85(6):063114, 2014.
- [78] Jongmin Lee. Spring gravimeters and other alternatives.

- [79] I Lesanovsky, S Hofferberth, J Schmiedmayer, and Peter Schmelcher. Manipulation of ultracold atoms in dressed adiabatic radio-frequency potentials. *Physical Review A*, 74(3):033619, 2006.
- [80] Jérôme Lodewyck, Philip G Westergaard, and Pierre Lemonde. Nondestructive measurement of the transition probability in a Sr optical lattice clock. *Physical Review A*, 79(6):061401, 2009.
- [81] Anthony G Mann, Chang Sheng, and Andre N Luiten. Cryogenic sapphire oscillator with exceptionally high frequency stability. *Instrumentation and Measurement, IEEE Transactions on*, 50(2):519–521, 2001.
- [82] MR Matthews, BP Anderson, PC Haljan, DS Hall, MJ Holland, JE Williams, CE Wieman, and EA Cornell. Watching a superfluid untwist itself: Recurrence of Rabi oscillations in a Bose-Einstein condensate. *Physical review letters*, 83(17):3358, 1999.
- [83] JM McGuirk, GT Foster, JB Fixler, MJ Snadden, and MA Kasevich. Sensitive absolute-gravity gradiometry using atom interferometry. *Physical Review A*, 65(3):033608, 2002.
- [84] Salvatore Micalizio, CE Calosso, Aldo Godone, and Filippo Levi. Metrological characterization of the pulsed Rb clock with optical detection. *Metrologia*, 49(4):425, 2012.
- [85] Holger Müller, Sheng-wei Chiow, Quan Long, Sven Herrmann, and Steven Chu. Atom interferometry with up to 24-photon-momentum-transfer beam splitters. *Physical review letters*, 100(18):180405, 2008.
- [86] TM Niebauer, GS Sasagawa, JE Faller, R Hilt, and Fred Klopping. A new generation of absolute gravimeters. *Metrologia*, 32(3):159, 1995.
- [87] Dennis Normile and Daniel Clery. First global telescope opens an eye on the cold universe. *Science*, 333(6051):1820–1823, 2011.

- [88] Caspar F Ockeloen, Roman Schmied, Max F Riedel, and Philipp Treutlein. Quantum metrology with a scanning probe atom interferometer. *Physical review letters*, 111(14):143001, 2013.
- [89] CF Ockeloen, AF Tauschinsky, RJC Spreeuw, and S Whitlock. Detection of small atom numbers through image processing. *Physical Review A*, 82(6):061606, 2010.
- [90] H Ott, J Fortágh, S Kraft, A Günther, D Komma, and C Zimmermann. Nonlinear dynamics of a Bose-Einstein condensate in a magnetic waveguide. *Physical review letters*, 91(4):040402, 2003.
- [91] Thomas E Parker. Long-term comparison of caesium fountain primary frequency standards. *Metrologia*, 47(1):1, 2010.
- [92] Christian G Parthey, Arthur Matveev, Janis Alnis, Birgitta Bernhardt, Axel Beyer, Ronald Holzwarth, Aliaksei Maistrou, Randolph Pohl, Katharina Predehl, Thomas Udem, et al. Improved measurement of the hydrogen 1 s–2 s transition frequency. *Physical review letters*, 107(20):203001, 2011.
- [93] Christopher Pethick and Henrik Smith. *Bose-Einstein condensation in dilute gases*. Cambridge university press, 2002.
- [94] William D Phillips. Laser cooling and trapping of neutral atoms. Technical report, DTIC Document, 1992.
- [95] John D Prestage, Sang K Chung, Lawrence Lim, and Annond Matevosian. Compact microwave mercury ion clock for deep-space applications. In *Frequency Control Symposium, 2007 Joint with the 21st European Frequency and Time Forum. IEEE International*, pages 1113–1115. IEEE, 2007.
- [96] John D Prestage, Sang K Chung, Robert J Thompson, and Paul MacNeal. Progress on small mercury ion clock for space applications. In *Frequency Control Symposium, 2009 Joint with the 22nd European Frequency and Time forum. IEEE International*, pages 54–57. IEEE, 2009.

- [97] Fernando Ramirez-Martinez, Michel Lours, Peter Rosenbusch, Friedemann Reinhard, and Jakob Reichel. Low-phase-noise frequency synthesizer for the trapped atom clock on a chip. *Ultrasonics, Ferroelectrics and Frequency Control, IEEE Transactions on*, 57(1):88–93, 2010.
- [98] J Reichel, W Hänsel, and TW Hänsch. Atomic micromanipulation with magnetic surface traps. *Physical review letters*, 83(17):3398, 1999.
- [99] Jakob Reichel and Vladan Vuletic. *Atom Chips*. John Wiley & Sons, 2010.
- [100] G Reinaudi, T Lahaye, Z Wang, and D Guéry-Odelin. Strong saturation absorption imaging of dense clouds of ultracold atoms. *Optics letters*, 32(21):3143–3145, 2007.
- [101] Friedemann Reinhard. *Design and construction of an atomic clock on an atom chip*. PhD thesis, Paris 6, 2009.
- [102] F Riehle, Th Kisters, A Witte, J Helmcke, and Ch J Bordé. Optical Ramsey spectroscopy in a rotating frame: Sagnac effect in a matter-wave interferometer. *Physical review letters*, 67(2):177, 1991.
- [103] Till Rosenband, DB Hume, PO Schmidt, CW Chou, A Brusch, L Lorini, WH Oskay, RE Drullinger, TM Fortier, JE Stalnaker, et al. Frequency ratio of Al⁺ and Hg⁺ single-ion optical clocks; metrology at the 17th decimal place. *Science*, 319(5871):1808–1812, 2008.
- [104] P Rosenbusch. Magnetically trapped atoms for compact atomic clocks. *Applied Physics B*, 95(2):227–235, 2009.
- [105] G Rosi, F Sorrentino, L Cacciapuoti, M Prevedelli, and GM Tino. Precision measurement of the Newtonian gravitational constant using cold atoms. *Nature*, 2014.
- [106] E. Rubiola. *Phase noise and frequency stability in oscillators*. Cambridge Univ Pr, 2009.

- [107] M Saba, TA Pasquini, C Sanner, Y Shin, W Ketterle, and DE Pritchard. Light scattering to determine the relative phase of two Bose-Einstein condensates. *Science*, 307(5717):1945–1948, 2005.
- [108] Patrice Salzenstein, Alexander Kuna, Ludvík Sojdr, and Jacques Chauvin. Significant step in ultra-high stability quartz crystal oscillators. *Electronics letters*, 46(21):1433–1434, 2010.
- [109] Giorgio Santarelli, Claude Audoin, Ala’a Makdissi, Philippe Laurent, G John Dick, and C Clairon. Frequency stability degradation of an oscillator slaved to a periodically interrogated atomic resonator. *Ultrasonics, Ferroelectrics and Frequency Control, IEEE Transactions on*, 45(4):887–894, 1998.
- [110] Giorgio Santarelli, Ph Laurent, Pierre Lemonde, André Clairon, Anthony G Mann, S Chang, Andre N Luiten, and Christophe Salomon. Quantum projection noise in an atomic fountain: A high stability cesium frequency standard. *Physical Review Letters*, 82(23):4619, 1999.
- [111] Jörg Schmiedmayer, Ron Folman, and Tommaso Calarco. Quantum information processing with neutral atoms on an atom chip. *Journal of Modern Optics*, 49(8):1375–1388, 2002.
- [112] T Schumm, S Hofferberth, L Mauritz Andersson, S Wildermuth, S Groth, I Bar-Joseph, J Schmiedmayer, and P Krüger. Matter-wave interferometry in a double well on an atom chip. *Nature physics*, 1(1):57–62, 2005.
- [113] BS Sheard, Gerhard Heinzel, Karsten Danzmann, DA Shaddock, WM Klipstein, and WM Folkner. Intersatellite laser ranging instrument for the GRACE follow-on mission. *Journal of Geodesy*, 86(12):1083–1095, 2012.
- [114] Y Shin, M Saba, TA Pasquini, W Ketterle, DE Pritchard, and AE Leanhardt. Atom interferometry with Bose-Einstein condensates in a double-well potential. *Physical review letters*, 92(5):050405, 2004.

- [115] Y Shin, C Sanner, G-B Jo, TA Pasquini, M Saba, W Ketterle, DE Pritchard, M Vengalattore, and M Prentiss. Interference of Bose-Einstein condensates split with an atom chip. *Physical Review A*, 72(2):021604, 2005.
- [116] CDJ Sinclair, EA Curtis, I Llorente Garcia, JA Retter, BV Hall, S Eriksson, BE Sauer, and EA Hinds. Bose-Einstein condensation on a permanent-magnet atom chip. *Physical Review A*, 72(3):031603, 2005.
- [117] F Sorrentino, Andrea Bertoldi, Quentin Bodart, L Cacciapuoti, M De Angelis, Y-H Lien, M Prevedelli, G Rosi, and GM Tino. Simultaneous measurement of gravity acceleration and gravity gradient with an atom interferometer. *Applied Physics Letters*, 101(11):114106, 2012.
- [118] David H Spradley, Lewis H Spradley Jr, and John P Wincelowicz Jr. Geodetic surveying system using multiple GPS base stations, October 13 1992. US Patent 5,155,490.
- [119] RJC Spreeuw, C Gerz, Lori S Goldner, WD Phillips, SL Rolston, CI Westbrook, MW Reynolds, and Isaac F Silvera. Demonstration of neutral atom trapping with microwaves. *Physical review letters*, 72(20):3162, 1994.
- [120] Camillo Stefanucci, Thejesh Bandi, Francesco Merli, Matthieu Pellaton, Christoph Affolderbach, Gaetano Mileti, and Anja K Skrivervik. Compact microwave cavity for high performance Rubidium frequency standards. *Review of Scientific Instruments*, 83(10):104706, 2012.
- [121] JK Stockton, K Takase, and MA Kasevich. Absolute geodetic rotation measurement using atom interferometry. *Physical review letters*, 107(13):133001, 2011.
- [122] Pippa Storey and Claude Cohen-Tannoudji. The Feynman path integral approach to atomic interferometry. a tutorial. *Journal de Physique II*, 4(11):1999–2027, 1994.

- [123] Joseph H Taylor Jr. Millisecond pulsars: Nature's most stable clocks. *Proceedings of the IEEE*, 79(7):1054–1062, 1991.
- [124] Yoshio Torii, Yoichi Suzuki, Mikio Kozuma, Toshiaki Sugiura, Takahiro Kuga, Lu Deng, and EW Hagley. Mach-Zehnder Bragg interferometer for a Bose-Einstein condensate. *Physical Review A*, 61(4):041602, 2000.
- [125] Philipp Treutlein. *Coherent manipulation of ultracold atoms on atom chips*. PhD thesis, lmu, 2008.
- [126] Philipp Treutlein, Theodor W Hänsch, Jakob Reichel, Antonio Negretti, Markus A Cirone, and Tommaso Calarco. Microwave potentials and optimal control for robust quantum gates on an atom chip. *Physical Review A*, 74(2):022312, 2006.
- [127] Philipp Treutlein, Peter Hommelhoff, Tilo Steinmetz, Theodor W Hänsch, and Jakob Reichel. Coherence in microchip traps. *Physical review letters*, 92(20):203005, 2004.
- [128] NV Vitanov and K-A Suominen. Time-dependent control of ultracold atoms in magnetic traps. *Physical Review A*, 56(6):R4377, 1997.
- [129] Ying-Ju Wang, Dana Z Anderson, Victor M Bright, Eric A Cornell, Quentin Diot, Tetsuo Kishimoto, Mara Prentiss, RA Saravanan, Stephen R Segal, and Saijun Wu. Atom Michelson interferometer on a chip using a Bose-Einstein condensate. *Physical review letters*, 94(9):090405, 2005.
- [130] Philip Westergaard, Jerome Lodewyck, and Pierre Lemonde. Minimizing the Dick effect in an optical lattice clock. *Ultrasonics, Ferroelectrics and Frequency Control, IEEE Transactions on*, 57(3):623–628, 2010.
- [131] S Wildermuth, S Hofferberth, I Lesanovsky, S Groth, P Krüger, J Schmiedmayer, and I Bar-Joseph. Sensing electric and magnetic fields with Bose-Einstein condensates. *Applied physics letters*, 88(26):264103, 2006.

- [132] S Wildermuth, P Krüger, C Becker, M Brajdic, S Haupt, A Kasper, R Folman, and J Schmiedmayer. Optimized magneto-optical trap for experiments with ultracold atoms near surfaces. *Physical Review A*, 69(3):030901, 2004.
- [133] Stephan Wildermuth, Sebastian Hofferberth, Igor Lesanovsky, Elmar Haller, L Mauritz Andersson, Sönke Groth, Israel Bar-Joseph, Peter Krüger, and Jörg Schmiedmayer. Bose–Einstein condensates: microscopic magnetic-field imaging. *Nature*, 435(7041):440–440, 2005.
- [134] Peter Wolf, Sebastien Bize, Andre Clairon, Andre N Luiten, Giorgio Santarelli, and Michael E Tobar. Tests of Lorentz invariance using a microwave resonator. *Physical review letters*, 90(6):060402, 2003.
- [135] R Wynands and S Weyers. Atomic fountain clocks. *Metrologia*, 42(3):S64, 2005.
- [136] Tilman Zibold, Eike Nicklas, Christian Gross, and Markus K Oberthaler. Classical bifurcation at the transition from Rabi to Josephson dynamics. *Physical review letters*, 105(20):204101, 2010.
- [137] O Zobay and BM Garraway. Two-dimensional atom trapping in field-induced adiabatic potentials. *Physical review letters*, 86(7):1195, 2001.